



THE HONG KONG  
POLYTECHNIC UNIVERSITY

香港理工大學

Pao Yue-kong Library

包玉剛圖書館

---

## Copyright Undertaking

This thesis is protected by copyright, with all rights reserved.

**By reading and using the thesis, the reader understands and agrees to the following terms:**

1. The reader will abide by the rules and legal ordinances governing copyright regarding the use of the thesis.
2. The reader will use the thesis for the purpose of research or private study only and not for distribution or further reproduction or any other purpose.
3. The reader agrees to indemnify and hold the University harmless from and against any loss, damage, cost, liability or expenses arising from copyright infringement or unauthorized usage.

### IMPORTANT

If you have reasons to believe that any materials in this thesis are deemed not suitable to be distributed in this form, or a copyright owner having difficulty with the material being included in our database, please contact [lbsys@polyu.edu.hk](mailto:lbsys@polyu.edu.hk) providing details. The Library will look into your claim and consider taking remedial action upon receipt of the written requests.

**SPECTRAL ANALYSIS AND CORRELATION  
STUDY OF VASOMOTION**

**LIU SHUHONG**

**PhD**

**The Hong Kong Polytechnic University**

**2022**

The Hong Kong Polytechnic University

Department of Mechanical Engineering

**Spectral Analysis and Correlation Study of  
Vasomotion**

**Liu Shuhong**

A thesis submitted in partial fulfillment of the requirements for the degree of Doctor of

Philosophy

July 2021

## CERTIFICATE OF ORIGINALITY

I hereby declare that this thesis is my own work and that, to the best of my knowledge and belief, it reproduces no material previously published or written, nor material that has been accepted for the award of any other degree or diploma, except where due acknowledgement has been made in the text.

\_\_\_\_\_ (Signed)

LIU Shuhong \_\_\_\_\_ (Name of student)

## **Abstract**

This thesis consists of two parts focusing on the origin of vasomotion and stochastic resonance in vascular motion, respectively.

The first part of the thesis concentrates on the origin of vasomotion. Vasomotion is the spontaneous time-dependent contraction and relaxation of micro arteries with an oscillation frequency of about 0.01 - 0.2 Hz. The physiological mechanisms of vasomotion have not been thoroughly understood. From a dynamics point of view, the heartbeat is the only external loading exerted on the vascular system. Since the period of heartbeat is not constant but variable, we speculated that nonlinear blood flow in the vascular system and variable heartbeat would induce low-frequency vasomotion. We simulated linear flow in a single pipe and nonlinear flow in a network of tubes and found that nonlinear flow would generate low-frequency components. As the vascular system is highly nonlinear, we could deduce that the variable period of heartbeat and the nonlinearity of the vascular system induce vasomotion. Furthermore, using a laser Doppler flowmeter, we measured the time series of radial artery blood flow. Two modified time series were reconstructed with different heartbeat curves but with the same period as the measured time series. Wavelet spectral analysis showed that the low-frequency components were induced by the variable period and independent of the shape of the heartbeat curve.

The second part of the thesis focuses on stochastic resonance (SR) in vasomotion. SR is characterized by a system's response to noise and signal-to-noise ratio (SNR). The SNR ascends rapidly and peaks at the point where the SR occurs, after which the SNR descends gradually with increasing noise intensities. We used a laser Doppler flowmeter to measure the time series of radial artery blood flow after adding different disturbances on the forearm. With different cuff pressures added to the radial artery blood flow, the SNR of different frequency bands (~1 Hz, ~0.3 Hz, ~0.1 Hz, 0.03 Hz, and 0.01 Hz) in the pulse signals changed with pressure. We can infer that the ancient Chinese physicians diagnosed by applying pressures on the wrist to sense the SNR changes of different frequency bands in the pulse signals which relates to cardiac, respiratory, myogenic,

neurogenic, and endothelial activities. With the disturbance of different noise added to the radial arterial blood flow, the experiment pulse signal was decomposed by HHT. We obtained instantaneous SNR and instantaneous noise from the decomposed IMFs, and the phenomenon of SR was observed in frequency bands around 1 Hz, 0.3 Hz, and 0.1 Hz. The SNR results show that the noise has effects on the blood signal related to the respiratory activities ( $\sim 0.3$  Hz), but has little influence on the signal related to cardiac activities ( $\sim 1$  Hz). Adding white noise and then stopping white noise causes an increase in SNR in the frequency band related to vasomotion ( $\sim 0.1$  Hz).

## **Publications**

### Journal paper:

Liu SH, Zhao L, Liu Y\*. The Origin of Vasomotion and Stochastic Resonance in Vasomotion. *Frontiers in in Bioengineering and Biotechnology*. 2022;10.

### Conference paper:

Liu SH, Chi TX, Tian S, Su ZD, Liu Y, & Luo XY (2017, August). Numerical Study of Fluid-Structure Interaction of Microvasculature. In *Symposium on Fluid-Structure-Sound Interactions and Control* (pp. 257-261). Springer, Singapore.

## **Acknowledgments**

First and foremost, I would like to thank my supervisor, Dr. Yang Liu, for his invaluable advice, continuous support, and patience during my Ph.D. study at the Hong Kong Polytechnic University. He suggested many important improvements, and it has been a greatly enriching experience for me to work under his authoritative guidance. His dedication and cheerful enthusiasm enabled me to complete my research in a respectable manner. Also, his meticulous scrutiny, scholarly advice, and scientific approach have supported me to a great extent to accomplish my thesis.

Second, I would like to express my gratitude to all the group members, Tianxi Chi, Mingran Liu, Jingyu Cui, and Liangjing Zhao. Their patience during data collection made an invaluable contribution to my Ph.D.

Third, I would like to thank my parents for their unconditional trust, timely encouragement, and endless patience during my Ph.D. study. It was their love that inspired me when I got weary.

Last but certainly not least, I thank with love to my husband Yi Cao for his accompany, love, support, and encouragement. He helped me through all these years in the most positive way.

# Contents

<b>Abstract</b> .....	<b>I</b>
<b>Publications</b> .....	<b>III</b>
<b>Acknowledgments</b> .....	<b>IV</b>
<b>Chapter 1 Introduction</b> .....	<b>1</b>
1.1 <i>Physiology of vasomotion</i> .....	1
1.2 <i>Cellular mechanisms of vasomotion</i> .....	3
1.3 <i>Vasomotion response to different stimulations</i> .....	5
1.4 <i>Pathophysiological role of vasomotion</i> .....	8
1.5 <i>Variation of heart period</i> .....	10
1.6 <i>Numerical models related to vasomotion</i> .....	11
1.7 <i>Noise type</i> .....	13
1.8 <i>Stochastic resonance</i> .....	13
1.9 <i>Summary and research gap</i> .....	15
1.10 <i>Objectives of this thesis</i> .....	15
1.11 <i>Organization of this thesis</i> .....	16
<b>Chapter 2 Methods</b> .....	<b>17</b>
2.1 <i>Wavelet analysis</i> .....	17
2.2 <i>Hilbert–Huang transform</i> .....	17
2.3 <i>Signal to noise ratio</i> .....	19
<b>Chapter 3 Numerical study of microvasculature</b> .....	<b>21</b>
3.1 <i>Simulation set-up</i> .....	21
3.2 <i>The Casson model</i> .....	22
3.3 <i>Validation of numerical models</i> .....	24
3.3.1 <i>The validation of the turbulence model</i> .....	24
3.3.2 <i>Effect of time step and significant figures of <math>\pi</math> on simulation results</i> .....	25
3.3.3 <i>Mesh independence</i> .....	28
3.4 <i>Low frequency induced by input period variation</i> .....	31
3.4.1 <i>0.2 Hz frequency input for different models</i> .....	31
3.4.2 <i>0.02459 Hz frequency input for different models</i> .....	45
3.5 <i>Frequency of the system</i> .....	48

<b>Chapter 4</b>	<b>The origin of vasomotion .....</b>	<b>50</b>
4.1	<i>Experiment procedure .....</i>	<i>50</i>
4.2	<i>Experiment results.....</i>	<i>52</i>
<b>Chapter 5</b>	<b>Stochastic resonance .....</b>	<b>56</b>
5.1	<i>Pressure disturbance .....</i>	<i>56</i>
5.1.1	Procedure .....	56
5.1.2	Results.....	58
5.2	<i>Noise disturbance.....</i>	<i>65</i>
5.2.1	Procedure .....	65
5.2.2	HHT results.....	67
5.2.3	Stochastic resonance of different noise .....	73
5.2.4	SNR for different disturbances of noise.....	76
<b>Chapter 6</b>	<b>Conclusions and future work.....</b>	<b>84</b>
6.1	<i>Conclusions.....</i>	<i>84</i>
6.2	<i>Future work .....</i>	<i>85</i>
<b>Reference</b>	<b>.....</b>	<b>87</b>

## List of figures

Figure 1-1 Measured blood flow oscillation in the radial artery.....	2
Figure 1-2 Measured heart periods .....	11
Figure 3-1 Numerical models: (a) real vessels in hand; (b) numerical vessel structure in hand; (c) connected-tubes model; (d) three-connected-tubes model; (e) four-connected-tubes model; (f) five-connected-tubes model, and (g) single tube model.....	21
Figure 3-2 Inlet velocity for numerical simulations (modified from a report study <sup>160</sup> ).....	22
Figure 3-3 Shear-thinning effect (RBC-Red blood cell) <sup>162</sup> .....	23
Figure 3-4 The mean wavelet results for point on the first connection for three-connected tube model using different turbulence model .....	25
Figure 3-5 Single tube model, inlet oscillating at 1Hz, different time steps, $\pi=3.1415$ , wavelet analysis.....	26
Figure 3-6 Single tube model, inlet oscillating at 1 Hz, time step of 0.01 s, $\pi=3.14159267$ , wavelet analysis .....	26
Figure 3-7 Single tube model, inlet oscillating at 1Hz, mean wavelet analysis.....	27
Figure 3-8 Three-connected-tubes model, inlet oscillating at 1 Hz, wavelet analysis and mean wavelet analysis .....	28
Figure 3-9 Mesh independence.....	31
Figure 3-10 Velocity input with a period of 5s.....	31
Figure 3-11 Monitor points on the model.....	32
Figure 3-12 Single tube model and three-connected-tubes model, point before connection, 0.2 Hz input frequency, wavelet analysis.....	33
Figure 3-13 Single tube model and three-connected-tubes model, point before connection, 0.2 Hz input frequency, mean wavelet analysis .....	33
Figure 3-14 Three-connected-tubes model, point on connections, 0.2 Hz input frequency, wavelet analysis .....	35
Figure 3-15 Three-connected-tubes model, point before and after three connections, 0.2 Hz input frequency, wavelet analysis .....	36
Figure 3-16 Experimental data, wavelet analysis .....	36
Figure 3-17 Three-connected-tubes model, 0.2 Hz input frequency, mean wavelet analysis.....	37
Figure 3-18 Three-connected-tubes model, points on the connections, mean wavelet analysis, different diameters: (a) 1 mm, (b) 4 mm and (c) 8 mm.....	39

Figure 3-19 Three-connected-tubes model, points on the connections, mean wavelet analysis, different maximum inlet velocities: (a) 1 mm/s, (b) 4 mm/s and (c) 8 mm/s .....	41
Figure 3-20 Three-connected-tubes model, points on the connections, 0.02 mm, 1 mm/s, mean wavelet analysis ....	42
Figure 3-21 Three-connected-tubes model, points on the connections, mean wavelet analysis, different number of connections: (a) four connected tubes, (b) five connected tubes and (c) six connected tubes .....	43
Figure 3-22 Three-connected-tubes model, different open-close states, 2 mm diameter, 2 mm/s maximum inlet velocity, 0.2 Hz input frequency, mean wavelet analysis .....	44
Figure 3-23 Measured data at the radial artery in the wrist, wavelet analysis and mean wavelet analysis.....	45
Figure 3-24 Velocity input of 40.5 s period.....	45
Figure 3-25 Three-connected-tubes model, points on three connections, 0.0245 Hz input frequency, wavelet analysis .....	46
Figure 3-26 Three-connected-tubes model, point before and after three connections, 0.0245 Hz input frequency, wavelet analysis.....	47
Figure 3-27 Three-connected-tubes model, 0.0245 Hz input frequency, mean wavelet analysis.....	48
Figure 3-28 Frequencies of the connected-tubes model system .....	49
Figure 4-1 Laser Doppler flowmetry .....	50
Figure 4-2 Reconstructed data and experimental data in three cycles .....	52
Figure 4-3 The wavelet analysis of the measured time series, the reconstructed signal, and the average flux signal .	53
Figure 4-4 The mean wavelet analysis of the measured time series, the reconstructed signal, and the average flux signal .....	54
Figure 5-1 Pulse diagnose and a sphygmomanometer cuff encircling the forearm .....	56
Figure 5-2 Five frequency bands in the wavelet analysis result .....	56
Figure 5-3 Instantaneous power spectrum in wavelet analysis.....	57
Figure 5-4 The SNR for frequency band around 1 Hz of four subjects with different pressures .....	58
Figure 5-5 The SNR for frequency band around 0.3 Hz of four subjects with different pressures.....	59
Figure 5-6 The SNR for frequency band around 0.1 Hz of four subjects with different pressures.....	60
Figure 5-7 The SNR for frequency band around 0.03 Hz of four subjects with different pressures.....	61
Figure 5-8 The SNR for frequency band around 0.01 Hz of four subjects with different pressures.....	62
Figure 5-9 SNR vs Noise for five frequency bands of subject 1 without pressure .....	64

Figure 5-10 A speaker placed on the forearm.....	65
Figure 5-11 An IMF component after HHT .....	65
Figure 5-12 Wavelet analysis for an IMF.....	66
Figure 5-13 Instantaneous power spectrum in the wavelet analysis for an IMF after HHT .....	67
Figure 5-14 The HHT IMFs of measured data of radial artery at the wrist without adding noise .....	69
Figure 5-15 The wavelet analysis for IMFs of measured data of radial artery at the wrist without adding noise .....	72
Figure 5-16 Stochastic resonance at 1 Hz.....	73
Figure 5-17 Stochastic resonance at 0.3 Hz.....	74
Figure 5-18 Stochastic resonance at 0.1 Hz.....	75
Figure 5-19 The average top 1000 SNR for frequency band around 1 Hz of ten experiments .....	78
Figure 5-20 The total average top 1000 SNR of ten experiments and their mean $\pm$ SD at different noise conditions for frequency band around 1 Hz .....	78
Figure 5-21 The average top 1000 SNR for frequency band around 0.3 Hz of ten experiments .....	80
Figure 5-22 The total average top 1000 SNR of ten experiments and their mean $\pm$ SD at different noise conditions for frequency band around 0.3 Hz .....	81
Figure 5-23 The average top 1000 SNR for frequency band around 0.1 Hz of ten experiments.....	83
Figure 5-24 The average top 1000 SNR of ten experiments and their mean $\pm$ SD at different noise conditions for frequency band around 0.1 Hz.....	83

## List of tables

Table 3-1 The coefficients of determination ( $R^2$ ) of the inlet velocity and the computed velocity of the point on the first connections, 2mm/s, different diameter .....	39
Table 3-2 The coefficients of determination ( $R^2$ ) of the inlet velocity and the computed velocity at the point on the first connection, different maximum inlet velocities .....	40
Table 3-3 The coefficients of determination ( $R^2$ ) of the inlet velocity and the computed velocity at the point on the first connection, different number of connections .....	42
Table 3-4 The coefficients of determination ( $R^2$ ) of the inlet velocity and the computed velocity at the point on the first connection, different open-close states.....	44
Table 3-5 RMS of oscillating pressure for different frequencies.....	49
Table 4-1 Anthropometric parameters for four subjects.....	50
Table 4-2 The coefficients of determination ( $R^2$ ) of mean wavelet analysis data between the reconstructed signal, the average flux signal, and the measured time series .....	55
Table 5-1 Absolute standard deviation coefficients of SNR.....	63

# Chapter 1 Introduction

## 1.1 Physiology of vasomotion

Vasomotion is spontaneous time-dependent contraction and relaxation of arteries, mainly in the micro arteries<sup>1</sup> but also in the large arteries<sup>2</sup>. Vasomotion may reveal the status of vascular function in other systems, and abnormalities in microvasculature may indicate the onset of some diseases<sup>3,4</sup>. Many studies have been conducted to recognize the link between vascular motion and cardiovascular disease<sup>5,6</sup>. However, the mechanism involved in vasomotion is still not fully understood. The phenomenon of vasomotion was observed by Jones<sup>7</sup> in 1852 of rhythmic changes in the batwing, and since then it has been detailed in many pieces of research both in vivo and in vitro. Both in living animals and in isolated arteries, vasomotion has been detected<sup>8-10</sup>. Apart from vessel diameter changes, several methods are applied to detect vasomotion, such as measuring blood-cell velocity<sup>11</sup>, capillary pressure variations<sup>12</sup>, or laser-Doppler flow (LDF) signals<sup>13</sup>. Many studies<sup>14-20</sup> analyzed characteristic frequencies of blood flow oscillation signals and these frequencies components correspond to several types of activities. Oscillations around ~1 Hz are related to the cardiac activity; oscillations around ~0.3 Hz are related to the respiratory activity; and oscillations between from 0.001 to 0.2 Hz are related to endothelial and myogenic activities<sup>9,12</sup>. Vasomotion is the oscillation related to endothelial and myogenic activities whose frequency interval is from 0.001 to 0.2 Hz. The in vivo study of vasomotion activity allows the behavior of the vasculature to be discussed in natural circumstance, and in vivo flow motion manifest a pattern that different periodic activities of various origins are integrated<sup>21</sup>. In our experiment in vivo in which blood flow oscillation was measured by LDF, several low frequencies components related to vasomotion were observed (Figure 1-1). In vitro, several frequency components related to vasomotion activities were observed in isolated arteries from different species and different vessels<sup>22,23</sup>, which is consistent with our experiment and other measurements in vivo<sup>24,25</sup>. In vitro studies help researchers to detail the experimental conditions to acquire knowledge of vasomotion physiology and to identify the inherent activities of vasomotion. Vasomotion is usually unpredictable and arduous to imitate in vitro experiments and fails

to be replicated in vitro, whereas the origin of different activities found in vivo experiments may be less clear<sup>26,27</sup>.

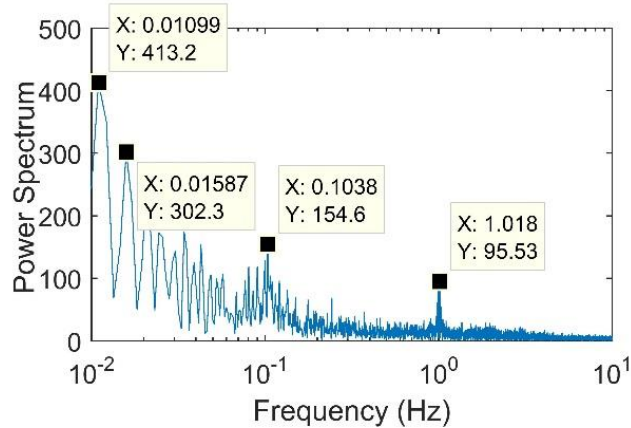


Figure 1-1 Measured blood flow oscillation in the radial artery

Conventionally, there are mainly five experimental methods to demonstrate vasomotion. The first method is vital microscopy. This is a conventional method to investigate vasomotion that the movements of blood vessels are directly observed. The experiments carried out by Colantuoni et.al<sup>28</sup> were conducted on anesthetized hamsters in vivo. They observed blood vessels by chamber window that implanted on skin fold. The second method is pressure measurement. In the study of Mahler et.al<sup>12</sup>, after direct cannulation, the provided arteriovenous pressure difference remained unchanged during the entire measurement, and the ratio of resistance in precapillary to postcapillary could be obtained by measuring the pressure in the capillaries. Pressure fluctuations were found, which may reflect vasomotion, in agreement with the findings in Wiederhielm and Weston's<sup>29</sup> experiment. The third method is blood-cell velocity measurement. The research by Fagrell et.al<sup>11</sup> recorded the capillary blood flow, where the velocity in the capillary was determined by measuring the time to pass a certain distance along. In their observations, most subjects had spontaneous fluctuations in blood cell velocity at the frequency of  $\sim 0.1$ Hz, which may be related to vasomotion. The fourth method is laser-Doppler flow measurement. There is an extensive application of LDF to study human skin circulation in the last half century because the LDF signal achieves a appraisal of tissue blood flow<sup>30-32</sup>. LDF uses the Doppler effect in the illuminated tissue to calculate the blood flow and can be used to detect the blood flow oscillations<sup>33,34</sup>. After photons in light beams are shot into the tissue, Doppler shifts induced by moving erythrocytes are evaluated by the cell's

scattering angle, wavelength, and velocity vector<sup>35</sup>. LDF is completely non-invasive and real-time at high sampling rates, and the frequency features of LDF signals can be processed with wavelet analysis<sup>36</sup>.

However, the neighboring vessels and main circulatory factors<sup>11,32-35</sup>, such as blood pressure fluctuations, are disturbances that need to be resolved in our measurements mentioned above. There is another method based on isolated vessels. This method can strictly follow controlled conditions and examine the local phenomena of excised isolated vessel segments with various kinds of organ-bath techniques. Notwithstanding that in vivo vasomotion is generally detected in capillaries, the isolated vessels are limited to relatively large arteries for technical reasons.

Localized oscillations in human skin blood flow circulation are presented in the studies<sup>37-39</sup> which indicates the existence of oscillations origin from the local and non-nervous, and the method based on isolated vessels can still suggest some cellular mechanisms of vasomotion. In many experiments, it is difficult to determine vasomotion under real body conditions. It is formidable to define the number of specific tones, so it is difficult to determine concentration-response curves explicitly<sup>40</sup>. Nevertheless, in the last half-century, achievements have been made on the exploration of cellular mechanisms and the physiological significance of vasomotion. The development of imaging techniques for visualizing intracellular contributes to the revelation of the possible cellular mechanisms underlying vasomotion.

## 1.2 Cellular mechanisms of vasomotion

For the generation of vasomotion, the existence of a cellular oscillator is necessary<sup>41,42</sup>. The cellular oscillator can be modeled as a feedback loop in which one or more steps in the loop represent a series of events to ensure the oscillation<sup>43</sup>. Based on the cellular mechanisms of vasomotion, cellular oscillations are partitioned into cytosolic and membrane oscillators<sup>44</sup>. Oscillators originating from the cytoplasm may be unnecessarily related to in membrane potential shifts that is found to be associated with the release or absorption of  $\text{Ca}^{2+}$  in intracellular storages<sup>21,40</sup>. It has been suggested that the oscillating of  $\text{Ca}^{2+}$  release and absorption is responsible for vasomotion vasodilation<sup>5,45</sup>. Intracellular

oscillators can be visualized by the intracellular  $\text{Ca}^{2+}$  transients and generally can be achieved under experimental conditions<sup>46</sup>. The periodic oscillation of  $\text{Ca}^{2+}$  waves was observed by Ruehlmann et al.<sup>47</sup>. The  $\text{Ca}^{2+}$  waves in the intracellular calcium concentration ( $[\text{Ca}^{2+}]_i$ ) represent rhythmical oscillation and are not synchronous between adjacent cells. After electrical and pharmacological stimulation to vascular smooth muscle cells (VSMCs),  $\text{Ca}^{2+}$  oscillates asynchronously<sup>28,48</sup>. When vasomotion occurs, oscillations of the  $[\text{Ca}^{2+}]_i$  in VSMCs are synchrony but not asynchrony, the  $\text{Ca}^{2+}$  wave disappears, and the global  $[\text{Ca}^{2+}]_i$  oscillations appear<sup>29,32-34</sup>. Despite the stimulus-induced  $\text{Ca}^{2+}$  oscillation, the  $\text{Ca}^{2+}$  waves also occasionally occur spontaneously<sup>47,49</sup>. And in lower concentrations of contractile agonists condition the spontaneous  $\text{Ca}^{2+}$  oscillation is more distinct<sup>45,50-52</sup>. Experimental data of Jacobsen et al.<sup>46</sup> observed significant heterogeneity in  $\text{Ca}^{2+}$  waves of different VSMCs in the vascular wall. In addition, for the purpose of synchronizing the  $\text{Ca}^{2+}$  oscillation in a single VSMCs, the synchronization by membrane potential variation concerns the interaction of the cytosolic oscillator and the membrane<sup>43</sup>. Other types of oscillations that are based on either oscillation of the glycolytic pathway or interaction of ion currents in the sarcolemma such as Na, K-pump, which may be effective under some conditions, are less mentioned<sup>40</sup>. The  $\text{Ca}^{2+}$  signals communicate through gap junctions and the intercellular spread of membrane potential oscillations may induce the synchronization of  $\text{Ca}^{2+}$  oscillating among sufficient smooth muscle cells (SMCs) which generate vasomotion. The myoendothelial junctions (MEJs) provide the pathway for such electrical coupling, which are more affluent in the gap junctions between SMCs. The synchronization of voltage and  $[\text{Ca}^{2+}]_i$  oscillations among SMCs is achieved by endothelium through MEJs coupled between the endothelial and smooth muscle layers<sup>44</sup>. Endothelium may act as a favourable pathway for the signal transmission along blood vessels and have an important effect on coordinating  $\text{Ca}^{2+}$  fluxes through electrical coupling in individual SMCs<sup>53</sup>.

Above all, rhythmical contraction in vascular smooth muscles is the basis of vasomotion. Contraction and relaxation of VSMCs are primarily driven by the oscillatory transient of intracellular  $\text{Ca}^{2+}$  through the operation of a cytosolic  $\text{Ca}^{2+}$  oscillator<sup>54</sup>. Nevertheless, the mechanisms under the contraction and relaxation of vascular smooth muscles are not exhaustively known.

### 1.3 Vasomotion response to different stimulations

The cellular response in vasomotion can be affected by many physiological stimuli, such as acetylcholine (Ach), potassium ion, norepinephrine (NE), and phenylephrine (PE)<sup>55-59</sup>. Topical application of vasoactive agents was delivered to stimulate the vascular wall in the study of Segal and Duling<sup>60</sup> and Welsh et al.<sup>61</sup>, and this local stimulus on the vascular wall leads to the partial changes in membrane potential of SMCs and transmits to adjacent vascular cells. Ach is capable of evoking a powerful hyperpolarization through the Ca<sup>2+</sup>-activated K<sup>+</sup> channels<sup>62</sup>. The responses of the experiment stimulated by Ach indicate that Ach induced the release of metabolites from arteriolar ECs which carried out SMCs hyperpolarization and contributed to vasodilation<sup>63</sup>. In the research of Peng et al.<sup>45</sup>, the NE stimulation of SMCs leads to intermittent Ca<sup>2+</sup> emit from the sarcoplasmic reticulum. The released Ca<sup>2+</sup> activates a membrane conductance and excited an inward current which results in depolarization and causes Ca<sup>2+</sup> influx which activates Ca<sup>2+</sup> release in overall cells. Thereby the Ca<sup>2+</sup> wave becomes global oscillations, synchronizing the cells and causing contraction of SMCs. After applying stimulation by NE and assessing the effect on Cl<sup>-</sup> conductance of isolate VSMCs, Boedtkjer et al.<sup>64</sup> found that in vasomotion Cl<sup>-</sup> conductance is critical in [Ca<sup>2+</sup>]<sub>i</sub> oscillations. Furthermore, the application of pharmacological tools such as niflumic acid, flufenamic acid, and mefenamic acids which blocks Ca<sup>2+</sup>-activated Cl<sup>-</sup> channels, activates Ca<sup>2+</sup>-activated K<sup>+</sup> channels<sup>65</sup>. This observation together with the analogous structure between Ca<sup>2+</sup>-activated Cl<sup>-</sup> channels and Ca<sup>2+</sup>-activated K<sup>+</sup> channels indicate that a homologous motif could exist. PE is proverbially used as a vasoconstrictor to find out the mechanism of Ca<sup>2+</sup> oscillations SMCs<sup>66</sup>. Lamboleley et al. conducted experiments in which arterial strips were stimulated by different PE concentrations, and revealed that the recruitment of SMCs strongly depends on the concentration of PE<sup>67</sup>. At a low concentration of PE, no local contraction was detected, and cell recruitment was not synchronous enough to generate vasoconstriction. With the increase of PE concentration, the number of recruited SMCs significantly increased, leads to an [Ca<sup>2+</sup>]<sub>i</sub> oscillation, and exhibits vasomotion. At a high concentration of PE, SMC recruitment almost completed instantly, the [Ca<sup>2+</sup>]<sub>i</sub> oscillated synchronously and was accompanied by a strong arterial strip contraction. In Haddock & Hill's research<sup>68</sup> by using ryanodine, the vascular tone remained unchanged, the SMCs

depolarized, the  $\text{Ca}^{2+}$  waves asynchrony abolished and rhythmical contractions were eliminated. The frequency of  $\text{Ca}^{2+}$  oscillations and spontaneous depolarization from the vessel wall increased and amplitude decreased. The  $\text{Ca}^{2+}$  waves were observed, but  $\text{Ca}^{2+}$  oscillations in individual SMCs were not detected. With some other treatments such as charybdotoxin and disulphonic acid,  $\text{Ca}^{2+}$  waves of individual SMCs oscillated synchronize in neighbouring cells. And weak rhythmical contractions were observed, and the amplitude of the contractions and depolarizations oscillated periodically. Overall, the cellular  $\text{Ca}^{2+}$  oscillations involve several mechanisms, and vasomotion can be affected by various physiological stimuli.

Vasomotion can be influenced by certain mechanical stimulations, such as stimuli to muscle fibers, intravascular pressure, temperature, vessel wall sheer stress. The segment of arteriole was cannulated and pressured in the research of Rivers<sup>69</sup> to study the effects of pressure on arterioles. Pressure transients in arterioles induce the change in the tension of smooth muscle which causes intercellular communication response, scilicet the muscle stretching leads the changes in membrane potential of VSMCs. The intercellular communication initiated by membrane potential variation spreads to the vasculature network and promotes global responses. Therefore, the arteriole pressure change could generate signals in the vasculature and spread throughout the network. The rhythmical fluctuations of blood flow in response to temperature changes were studied by Sheppard et al.<sup>70</sup>. The responses of blood flowmotion to cooling are similar to that during reduced pressure<sup>69</sup>, and as a result of vasoconstriction, there is an immediate drop in frequency and an increment in the amplitude of the synchronized myogenic oscillations. At low temperatures, the blood perfusion is reduced, and the metabolic activity and the rate of spontaneous oscillation are slowed in the smooth muscle fibers. During the heating process, vasodilation is produced, and the smooth muscle fibers are extended. The PSD proportion of the oscillation  $\sim 0.1$  Hz reduced, and the PSD proportion of the oscillation related to cardiac activity increased. The effects of vessel wall stress on vasomotion were also investigated by Koenigsberger et al.<sup>71</sup>. The shear stress applied to the ECs induces  $\text{Ca}^{2+}$  influx through stretch-activated channels which increases the  $\text{Ca}^{2+}$  level in the ECs. The  $\text{Ca}^{2+}$  level in the SMCs increases due to the stress in SMCs and decreases due to the stress in ECs. In addition, the myogenic response was promoted by

stress in SMCs and suppressed by stress in ECs. Typically, the shear stress causes an increase in  $\text{Ca}^{2+}$  levels in SMCs and vasoconstriction. The muscle fiber was stimulated in the research of Berg et al.<sup>72</sup>. The muscle fibers' contraction produces the dilation of the remote upstream arterioles and initiates a vasodilatory signal. The increase in capillary blood flow, involving conducted vasomotor responses and possible flow-dependent expansion, is regulated by dilations of the upstream arterioles away from the contracting muscle fibers and is not affected by the direct release of vasoactive metabolites. Davis et al.<sup>73</sup> studied the contribution of  $\text{Ca}^{2+}$  in the stretching response of vascular smooth muscle to an increasing active force. They found that stretching individual VSMCs led to the increase of intracellular  $\text{Ca}^{2+}$ . Stretching can induce  $\text{Ca}^{2+}$  to release from intracellular stores and  $\text{Ca}^{2+}$  influx to cross the plasma membrane. A mechanical stimulus was generated in the experiment of Demer et al.<sup>74</sup> by a microprobe impulse which is a discrete and detailed mechanical force and applied to a single cell. Both stimulated and adjacent ECs respond to direct mechanical stimulation.  $[\text{Ca}^{2+}]_i$  increases and spreads from the contact site to the cell edges as a  $\text{Ca}^{2+}$  wave. As the distance from the stimulated cell increases, the time delay of  $\text{Ca}^{2+}$  wave appearing in neighboring cells increases, and the peak  $[\text{Ca}^{2+}]_i$  in each cell decreases. In Li et al.'s experiments<sup>75</sup>, an acoustic shear wave was generated by the mechanical movement of a needle and was able to initiate cytosolic  $\text{Ca}^{2+}$  rise in both excitatory and non-excitatory cells, to induce  $\text{Ca}^{2+}$  oscillations, and to augment in vivo  $\text{Ca}^{2+}$  release into blood plasma in mice. The periodic transports of  $\text{Ca}^{2+}$  flux introduce a time-periodic cytoplasmic calcium concentration, the cross-bridges formation in smooth muscles, and the development of muscle stress. The resultant muscle stresses determine the rate of change in vessel diameter: vasomotion<sup>21,22</sup>. Arterial blood vessels respond to an increase in vessel pressure, a phenomenon that Bayliss<sup>76</sup> termed the myogenic response. Generally, myogenic contractions are thought to be initiated by vascular smooth muscle and capable of regulating  $\text{Ca}^{2+}$  entry through voltage-gated  $\text{Ca}^{2+}$  channels. Micheal's experiment results<sup>77</sup> illustrate that arteriole vasodilation in response to an acute pressure increase and the  $[\text{Ca}^{2+}]_i$  is changing with different pressure.

#### 1.4 Pathophysiological role of vasomotion

Vasomotion may mirror the conditions of other systemic vascular functions, the microvascular abnormalities may reflect the sequence of pathological conditions, and changes in the pattern of vasomotion implicate several pathological conditions<sup>4,5,78,79</sup>. By assessing vasomotion in patients with different pathological conditions, the characteristics of oscillations in the blood perfusion provide further insights into microvascular disease. There are number of studies about the significance of vasomotion in hypertension. The positive correlation between vasomotion and blood pressure in hypertensive rats reveals an inseparable connection between high blood pressure and the oscillatory ability of blood perfusion<sup>76,77,80</sup>. Correspondingly, essential hypertensive patients observed increased amplitude in vasomotion. Rossi et al.<sup>8</sup> investigated the relationship between essential arterial hypertension and vasomotion of skin arteriole. In patients with long-standing essential arterial hypertension, the absent post-ischemic increase of the skin vasomotion component was observed which was not reported in newly diagnosed hypertension patients. A disturbed skin blood flowmotion response to ischemia and a preserved increase in skin blood perfusion after ischemia indicate that the myogenic activities are engaged in skin blood flow control and it is more sensitive to explore skin vasomotion than to measure skin reactive hyperemia in the assessment of skin vasomotion disorders, in the early stage of essential arterial hypertension. Subsequently, they conducted experiments to investigate the skin blood flowmotion in hypercholesterolemic patients<sup>81</sup>. The increase in PSD of the vasomotion frequency component ( $\sim 0.01$  Hz) which is induced by a blunted Ach and related to endothelium activity may predict skin microvascular endothelial dysfunction in hypercholesterolemic patients without clinically manifest. The investigation of the skin vasomotion to study endothelial cell dysfunction in the skin microvascular bed is of clinical significance for patients with hypercholesterolemia.

The observation of Schmidt et al.<sup>31</sup> denotes that the prevalence of vasomotion is increased in patients with the mild peripheral arterial occlusive disease. Nevertheless, for the patients who have similar blood flow, the tissue oxygen levels were notably higher in patients who were detected with vasomotion than those not detected. This finding is

profitable for perspectives of pathogenesis and treatment in peripheral arterial occlusive disease.

Ramadan et al.<sup>82</sup> explored the pathophysiology of ischemia caused by mental stress. They observed that the response of vasomotion to mental stress may recognize the hazards of initiating induced myocardial ischemia, and that the vasomotion dysregulation would initiate induced myocardial ischemia. In addition, mental stress-induced ischemia potentially is treatable and/or improved by targeting at modulating vasomotion changes.

The endothelial function in the skin microvascular bed was examined in systemic scleroderma patients in the research of Schlez et al.<sup>83</sup>, and the results illustrate that the endothelium-independent vasomotion in systemic scleroderma patients is considerably perturbed. In both healthy subjects and patients with systemic scleroderma, the injection of Ach resulted in endothelium-independent vasomotion. A critical decrease in capillary blood flow velocity and an increase in vascular diameter were observed in healthy subjects, but not in systemic scleroderma patients, and thus the endothelium was damaged in patients with systemic scleroderma.

Skin endothelial-dependent vasomotion in Type 2 diabetes patients has been discussed by Schmiedel et al.<sup>84</sup>. A general disturbed endothelium-independent vasomotion is found in Type 2 diabetes patients suggesting that diabetes impairs microvascular perfusion generally and that an impairment of the endothelium-dependent mechanisms is involved in microalbuminuria. Thus, microalbuminuria associated with microvascular endothelial dysfunction in Type 2 diabetes patients seems to be closely related to the perturbed endothelium-dependent mechanisms. This phenomenon represents that vasomotion functional derangement or vascular structural abnormalities originate from microalbuminuria in Type 2 diabetes. In insulin-independent diabetic patients and diabetic patients with neuropathy, analogous findings have been observed by Schmiedel et al.<sup>84</sup> that the vasomotion was impaired<sup>84-87</sup>. These observations are in compliance with several animal studies with streptozotocin-induced diabetes showing that vascular tone virtually vanishes in bat wings, hamster cheek pouch<sup>88</sup>, and rat spinotrapezius muscle<sup>89</sup>.

Jongh et al.<sup>90</sup> have demonstrated that obesity-associated microvascular dysfunction is caused by a local and direct effect on the microvasculature. The results show that skin

microvascular vasomotion observed in women with obesity is severely impaired and with less endothelial activity compared to that in slim women.

The importance of vasomotion for oxygen delivery and nutritional blood supply has been illustrated in several studies<sup>91-94</sup>. The vasomotion in skeletal muscle ceased in the experiment of Rucker et al.<sup>92</sup>, and the functional capillary density and individual capillary blood flow decreased in the periosteum, subcutaneous tissue, and skin. The skeletal muscle is not capable of eliciting nutritive perfusion by itself, while vasomotion in skeletal muscle can maintain the microvascular perfusion in the muscle and neighboring tissues and may safeguard the nutritional blood supply within muscles. The observations in the research of Bertuglia et al.<sup>93</sup> indicate that vasomotion has a significant influence on tissue oxygenation and could reduce average blood flow resistance which helps to the balance between blood flow in tissue and vessels. The hyperoxia support enhances the vasomotion patterns, and the changes in the pattern of vasomotion stimulate the microvascular responses which would result in the change in mean vessel diameter.

Thus, there is undoubtedly physiological significance that the exploration of the mechanism of vasomotion provides clues to understand different microvascular diseases.

### **1.5 Variation of heart period**

Traditionally the heart beating is considered as a regular rhythm with a constant heart period. However, the heart rate, i.e., the number of heartbeats per minute, is a nonstationary signal in fact. As shown in Figure 1-2, the heart period measured with LDF is changing with time, which indicates that the heart period varies from beat to beat. Heart rate variability (HRV) is the alterations in the time intervals between adjacent heartbeats<sup>95</sup>. Being a reliable reflection of blood pressure, vascular tone, regulation of autonomic balance, heart, gas exchange, gut, possibly facial muscles, and many other physiological factors, HRV helps the human body adapt to environmental challenges and relates to health, self-regulatory capacity as well as adaptability<sup>96-98</sup>. Furthermore, healthy and diseased biological systems exhibit dissimilarities in their spatial and temporal complexity of the general regulation of heart rhythm, which can be reflected by HRV and processed to reveal existing or imminent cardiovascular disease<sup>99</sup>.

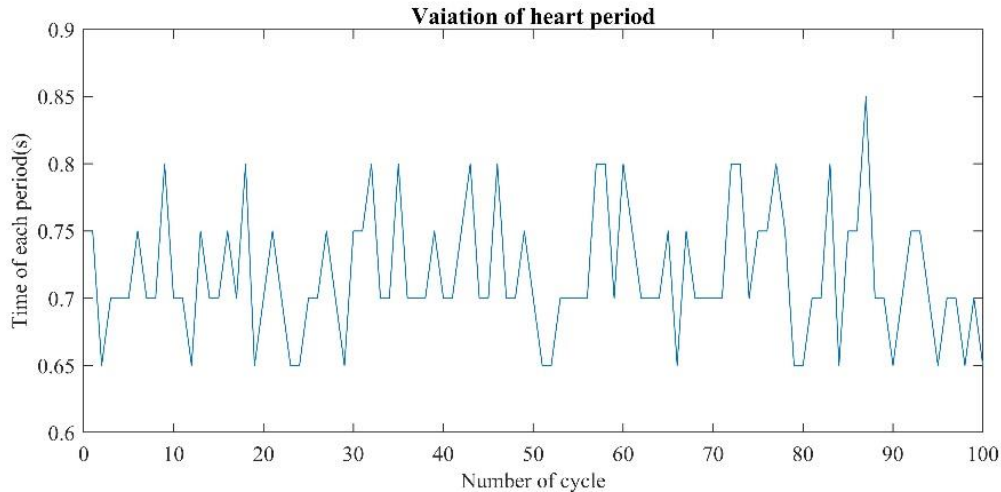


Figure 1-2 Measured heart periods

Baroreceptors are blood pressure sensors involved in short-term HRV, which locates in the aortic arch and internal carotid arteries<sup>97</sup>. Linked to vascular tone, blood pressure, and heart rate, baroreflex accelerates or decelerates heart rate as well as vascular tone when baroreceptors detect ascent or descent in blood pressure during respiration activities<sup>100,101</sup>. Other impact factors such as the central nervous, endocrine, and chemoreceptors also contribute to different frequency components in short term HRV spectrum<sup>95,102</sup>. A survey reveals<sup>103</sup> that the system producing the healthy heart oscillations is not only simply linear and has complex and nonlinear components. Exposed to dynamic methods of HRV quantification, the unnoticeable heart rate nonlinear variations can be described by mathematical chaos<sup>104</sup>. Nonlinear fluctuations in HRV provide the cardiovascular system with rapid responses to uncertain conditions, but the elevated value of nonlinearity of HRV is not a healthy indicator for stressors and disorders of diseases<sup>105</sup>.

## 1.6 Numerical models related to vasomotion

Several models have been developed for the generation of vasomotion to identify the underlying cellular mechanisms. As mentioned in section 1.2, the cellular oscillations are partitioned into cytosolic and membrane oscillators. In terms of cytosolic oscillators, many reports<sup>106-108</sup> provide models for the generation of oscillations in  $[Ca^{2+}]_i$ .  $Ca^{2+}$  oscillations caused by sarcoplasmic reticulum-released  $Ca^{2+}$  ions are presented by these models and

the simulation results of the models have received experimental support. These models give evidence that vasomotion is related to the actions of a cytosolic  $\text{Ca}^{2+}$  oscillator. Parthimos et al.<sup>109</sup> investigated the cellular mechanisms underlying vasomotion by a theoretical model about vasomotion in rabbit ear artery. In their study, cellular oscillations in the rabbit ear artery were considered, and vasomotion was characterized as a low-dimensional chaotic process with only a small number of variables modeled. Both the cytosolic and a membrane oscillator are independently involved in the theoretical model, and a variety of oscillation modes can be precisely created. They hypothesized that the independent oscillatory activity induced by membrane oscillator initiates fast oscillation, while cytosolic oscillator initiates slow oscillation. In another report from Griffith et al.<sup>110</sup>, by using pharmacological analysis, they confirmed the hypothesis that the origin of fast oscillation is related to the membrane oscillator, and that the cytosolic oscillator can generate slow oscillation. Furthermore, Parthimos et al.<sup>109</sup> made a mathematical model based on isolated rabbit arteries. The simulation of complex chaotic patterns of response can be achieved considering that arterial tone is regulated by the nonlinear interactions between ion transport systems. They simply illustrated the individual cell oscillations but did not include multiple cells. A few models are made in multiple cells to investigate vasomotion. In the process mentioned in section 1.2, vasomotion is generated by the synchronization of  $\text{Ca}^{2+}$  oscillations in a network of VSMCs. Later in 2007, Parthimos et al.<sup>111</sup> discussed a vasomotion model that employed membrane potential,  $[\text{Ca}^{2+}]_i$  in the cytosol, and  $\text{Ca}^{2+}$  in intracellular stores as dominant variables. By a combination of synchronized cells, the complex chaotic behavior of response is analyzed. All of the above models discussed the cellular mechanisms of vasomotion and oscillations in VSMCs, however, the fundamental mechanism of vasomotion has not been clarified. In addition to the above studies that explored the flow-dependent stimulations on the features of vasomotion, the cellular mechanisms, the effects of myogenic, and microvascular perfusion regulation were investigated by Ursino et al.<sup>112</sup> through a numerical model of a microvasculature. Their model evaluated the effects of flow-dependent stimuli on vasomotion, such as variations in arteriolar effective diameter and variations in arterial blood pressure. And vasomotion patterns related to vasodilation and vasoconstriction were evaluated. A theoretical model with dynamic variables in vessels

such as diameter and activation level were presented by Arciero<sup>113</sup>. Arciero's model was used in both a single vessel and simplified networks and involved the effects of wall shear stress and oxygen-dependent metabolic signals on smooth muscle activation. Based on Arciero's model, the generation of vasomotion depended on several parameters, the level of metabolic stimuli, vascular characteristics, and vasoactive substance.

### 1.7 Noise type

White noise is a noise whose frequencies are distributed equally over a wide range of frequencies with uniform intensity. Colored noise is noise with uneven distribution of frequency components. Pink noise is one of the colored noises whose intensity has an inverse correlation with the frequency, and the energy is equal for all octaves. At a constant bandwidth, the pink noise decreases at a rate of 3 dB per octave.

### 1.8 Stochastic resonance

By adding random perturbations, feeble information in the signal of the nonlinear system is amplified, discriminated, and optimized. This phenomenon refers to stochastic resonance (SR) which can be described by the response of the system to varying noise<sup>114</sup>. SR is discernible in nonlinear systems when the signal to noise ratio (SNR) ascends sharply to a peak then decreases moderately due to a continuous increase in input noise intensity<sup>115</sup>. Three fundamental components include in SR are: an energetic activation barrier which acts as a form of threshold, a feeble coherent input such as periodic signal, and a source of noise that is inherent in the system or adds to the coherent input<sup>116</sup>. Because of its generic nature, the threshold behaviors of SR indicate many physiological functions, and SR extends its applications in many technical fields such as classical and quantum physics, engineering, chemistry, biology, and medicine<sup>117</sup>. The first SR study in biological and biomedical aspects was conducted in 1991 on neuronal networks<sup>118-120</sup>, and then further discussions were conducted in more specific areas such as crayfish mechanoreceptors<sup>121</sup>, isolated rat skin sensory neuron system<sup>122</sup>, and hippocampal brain tissue<sup>123</sup>. In recent years, researchers have found that SR is involved in human blood pressure control which is called the 'baroreflex' system<sup>124</sup>. As mentioned in section 1.5,

in the baroreflex system, baroreceptors detect blood pressure fluctuation, and as negative feedback, heart rate and vascular tone are modulated. The experiment conducted by Gluckman et al.<sup>123</sup> in a mammalian brain and the dynamical model proposed by Mandell and Selz<sup>125</sup> illustrate that the information processing in the brain is enhanced by noise, and their findings support the conclusion that in the brain the noise performs a functional role. In both arterial and venous, there are receptors in the baroreflex system located in the neck region monitoring the blood pressure. The brain stem receives the afferent inputs from receptors and transmits efferent outputs through a common pathway into the peripheral organs. Without the addition of noise, this weak subthreshold signal would neither result in an appreciable blood pressure response nor stimulate a baroreflex response. After the addition of noise to the receptors, together with the weak signal inputs, an enhanced output response is produced which is conveyed via a common pathway load into the heart system. The threshold-like behaviour is related to SR whose nonlinearity initiate the intensified baroreflex response in brain stem<sup>126,127</sup>. SR involved in this process acts at the higher level of the brain stem, demonstrating functional benefits of adding noise to the brain which optimizes the response<sup>117</sup>. However, there is inherent background noise in the human cardiovascular system<sup>128</sup>, and even without additional noise, the weak fluctuations in venous blood pressure will not result in perceptible heart rate responses but conversely alter the baroreflex sensitivity and trigger the arterial baroreflex<sup>126</sup>. Therefore, the transmission process between blood pressure and the outputs of efferent neural activities is impractically simple and linear in baroreflex physiology evaluation<sup>129,130</sup>, and might be influenced by intrinsic background noise. Most importantly, recouping brain dysfunction by adding external noise provides an experimental foundation for biomedical engineering applications<sup>131</sup>. Furthermore, based on the concepts of nonlinear dynamics of SR, optimizing weak biological information is not restricted to the method of noise-aided transmission but also bifurcation schemes<sup>132</sup> and self-organization<sup>133</sup>. Finally, there are several biomedical applications of SR such as improving human balance control and somatosensation<sup>134,135</sup>, enhancing cochlear implants<sup>136-138</sup>, and mechanical life-support ventilators<sup>131,139</sup>. Several researchers are still looking into the biological mechanism of unpredictable fluctuations<sup>140-144</sup> that is significant in the development of biomedicine.

## 1.9 Summary and research gap

The above-mentioned numerical studies in section 1.6 proved that the cytosolic oscillator, the membrane oscillator, and the metabolic oscillator can activate vasomotion. But the fundamental mechanism of vasomotion is still unclarified, and how the vasomotion frequency band is generated has not been studied. Based on the descriptions of vasomotion, smooth muscle, and calcium flux above, we have three findings: (1) the basis of vasomotion is the rhythmical contraction in vascular smooth muscles; (2) contraction and relaxation of VSMCs are primarily driven by the oscillatory release of  $\text{Ca}^{2+}$ ; and (3)  $\text{Ca}^{2+}$  can be released either by applying an acoustic shear wave on ECs and muscle cells or by stretching on SMCs. I suppose that the shear wave causes the release of  $\text{Ca}^{2+}$  and the rhythmical contraction of vascular smooth muscles, and hence governs vasomotion. Thus, the blood flow oscillation induces the shear wave on SMCs, which induces vasomotion. We tried to find the inherent mechanism of vasomotion deep in the blood flow itself. However, the experimental studies on vasomotion illustrated in sections 1.2 and 1.3 are focused on cellular mechanisms. In this thesis, we extract the signal characteristics from experimental data and try to reveal the origin of this blood flow oscillation. Several studies on SR in biology and biomedical engineering are mentioned in section 1.7. The studies on SR in blood flow mainly focused on the baroreflex system, which is related to respiratory activities, and SR in other frequency bands has not been demonstrated yet. In this thesis, we try to study the phenomenon of SR in pulse signals in all frequency bands, which are related to other activities such as cardiac, endothelial, and myogenic activities.

## 1.10 Objectives of this thesis

The first part of the thesis is devoted to the numerical simulation of linear flow in a single pipe and nonlinear flow in a piping network. The main objective is to find out the origin of low-frequency blood flow oscillation ( $\sim 0.1\text{Hz}$ ) and the mechanism of vasomotion. Since the two fundamental determinants in the blood circulation system are the heartbeat and vascular structure, the objectives of this part are:

(1) To develop a 3D model of the vascular structure.

- (2) To numerically investigate the relationship between the variable period of input heartbeat and low-frequency components of the output.
- (3) To numerically investigate the relationship between the nonlinearity of the vascular structure and low-frequency components of the output.

The second part of this thesis aims to investigate the origin of vasomotion experimentally. From a dynamics point of view, the heartbeat is the only external loading exerted on the vascular system. The objectives of this part are:

- (1) To characterize the pulse signal from the experimental data.
- (2) To investigate the lower frequency band (0.01~0.2 Hz) and find its origin.

The first part and the second part of this thesis illustrate possible mechanisms that could induce vasomotion. The third part of the thesis is about SR. This part aims to study the phenomenon of SR in pulse signals. The objectives of this part are:

- (1) To investigate the effect of pressure adding to the radial arterial blood flow to SNR of the pulse signal.
- (2) To study the effect of noise adding to the radial arterial blood flow to SNR of the pulse signal.

### **1.11 Organization of this thesis**

The structure of this thesis is presented as follows. Chapters 1 and 2 give a brief introduction to vasomotion and methods. In Chapter 3, linear flow in a single pipe and nonlinear flow in a piping network are investigated numerically. The simulated results with different inputs are discussed. The inherent frequency of the human microvasculature system is studied. In Chapter 4, the laser Doppler flowmeter is used to measure the time series of radial artery blood flow. The experimental time series is reconstructed to find the origin of vasomotion. In Chapter 5, the phenomenon of stochastic resonance is investigated by adding disturbance to the radial artery blood flow. Chapter 6 concludes this study and lists the future work.

## Chapter 2 Methods

### 2.1 Wavelet analysis

Fourier spectrum analysis and wavelet analysis are two important methods of spectral analysis employed in studying regulation mechanisms of the skin microvascular vasomotion<sup>9,30</sup>. It assumes in Fourier spectrum analysis that a time series is composed of a finite number of periodic sinusoidal functions which are different in frequencies and phases. Fourier spectrum analysis conveys the overall amplitude of a signal at particular frequencies which can be utilized to describe the cyclic pulses in skin blood flow. Wavelet is a zero-mean function located in time and frequency domain. And a three-dimensional construction can be built using the wavelet transform for a time series based on the time-frequency plane<sup>145</sup>. There are two types of wavelet transforms, continuous wavelet transform (CWT) and discrete wavelet transform (DWT). The continuous wavelet transform contributes to discovering the major oscillatory modes of a signal and the changing of those modes in times. Thus, the skin blood flow signals are suggested to be analyzed using continuous wavelet transform due to their continuously varying features. The continuous wavelet transform of a signal  $g(u)$  is given by,

$$g(s, t) = \frac{1}{\sqrt{s}} \int_{-\infty}^{\infty} \psi\left(\frac{u-t}{s}\right) g(u) du$$

where  $t$  is the position of the signal over time,  $s$  is the scale factor, and  $\psi$  is the wavelet function. The wavelet used in this thesis is a Morlet wavelet because of its excellent balance between time and frequency positioning. The complex Morlet wavelet is defined as,

$$\psi(u) = \frac{1}{\sqrt[4]{\pi}} e^{i2\pi f_0 u} e^{-u^2/2}$$

### 2.2 Hilbert–Huang transform

Generally, Fourier spectra give a relevant description of linear and stationary signals, and the analysis results are only capable of indicating global properties. Thus, it is

controversial to apply Fourier spectrum analysis to nonlinear and nonstationary signals. In a real situation, the most process is neither linear nor stationary. Hilbert–Huang transform (HHT) is recently proposed and designed by Huang et al.<sup>146-148</sup> and is potentially viable in analyzing data from nonlinear and nonstationary signals. This method is an empirical method that consists of empirical mode decomposition (EMD) and Hilbert spectral analysis (HSA)<sup>149</sup>. As a part of HHT, HAS is a way to present non-stationarity through obtaining instantaneous frequency and amplitude. The Hilbert transform  $y(t)$  for any real value signal  $x(t)$  is,

$$y(t) = H[x(t)] = \frac{1}{\pi} PV \int_{-\infty}^{\infty} \frac{x(\tau)}{t - \tau} d\tau$$

in which  $PV$  indicate the Cauchy principal value of the singular integral. The analytic signal is defined by,  $z(t) = x(t) + iy(t) = a(t)e^{i\theta(t)}$ , where the instantaneous amplitude is  $a(t) = \sqrt{x^2 + y^2}$ , the instantaneous phase function is  $\theta(t) = \arctan\left(\frac{y}{x}\right)$ , and instantaneous frequency is  $\omega = \frac{d\theta}{dt}$ .

As a crucial part of HHT, the EMD is derived from the local signatures of nonlinearity. Based on the assumption that the data may have many coexisting simple oscillatory modes of significantly different frequencies one superimposed on the other at any given time<sup>150</sup>, the EMD can decompose any complicated data into intrinsic mode functions (IMFs). IMFs are defined to satisfy the following two conditions (1) in the whole dataset, the number of extrema of the signal and the number of zero-crossings must either equal or differ by one, and (2) at any point, the mean value of the envelope defined by the local maxima and the envelope defined by the local minima is zero<sup>150</sup>. The IMF is extracted by the following steps:

- (1) Identify all the local extrema of an input signal  $x(t)$
- (2) Connect all maxima and minima which will form the upper envelop and lower envelop and calculate the mean  $m_1$  of the envelope defined by the local maxima and the envelope defined by the local minima

(3) The difference  $d_1$  between input data  $x(t)$  and their mean  $m_1$  is calculated that  $d_1 = x(t) - m_1$ , and  $d_1$  satisfies the definition of an IMF

(4) Repeat the shifting process above after  $k$  times of iterations,  $d_{1k} = d_{1(k-1)} - m_{1k}$ , and the IMF  $c_1 = d_{1k}$

(5) The residual  $r_1 = x(t) - c_1$  is treated to be a new set of data and repeat the same shifting process  $r_n = r_{n-1} - c_n$

(6) Sum up the residual equations,  $x(t) = \sum_{j=1}^n c_j + r_n$ , that is the input signal  $x(t)$  is decomposed into IMFs  $c_n$  and residual  $r_n$ .

After Hilbert transform for each IMF component, the signal  $x(t)$  can be expressed as

$$x(t) = Re\left[\sum_{j=1}^n a_j(t)e^{i\int\omega_j(t)dt}\right]$$

In many studies<sup>151,152</sup>, HHT is validated empirically, and HHT is able to reveal signals' true physical meanings in the time and frequency domain. This methodology provides much more apparent results than analysis results of traditional methods, particularly in time-frequency-energy representations<sup>149</sup>. Recently, HHT is applied to biomedical signal analysis, such as decomposes of electrocardiographic signal<sup>153-156</sup> and ballistocardiograph signal<sup>157,158</sup>. By decomposing signals and extracting ambiguous information hidden behind the signals, the effects of external stimuli on the cardiovascular system may be determined.

### 2.3 Signal to noise ratio

The signal to noise ratio (SNR) is defined as the ratio of the signal power to the noise power,

$$SNR = P_s / P_n$$

where  $P_s$  is the average signal power and  $P_n$  is the noise power. It is normally adopted by engineers when both signal and noise are broadband that the SNR is calculated by

the ratio between the total integrated signal power  $S_p$  to that of the total integrated noise power  $N_p$  <sup>159</sup>.

$$SNR = S_p / N_p$$

The decibel uses a logarithmic scale to represent signals and thus a wide range of ratios can be demonstrated easily. Many signals have a very wide dynamic range, and based upon the definition of decibels (dB), the SNR can be expressed in dB as,

$$SNR_{dB} = 10 \log_{10} (S_p / N_p)$$

## Chapter 3 Numerical study of microvasculature

### 3.1 Simulation set-up

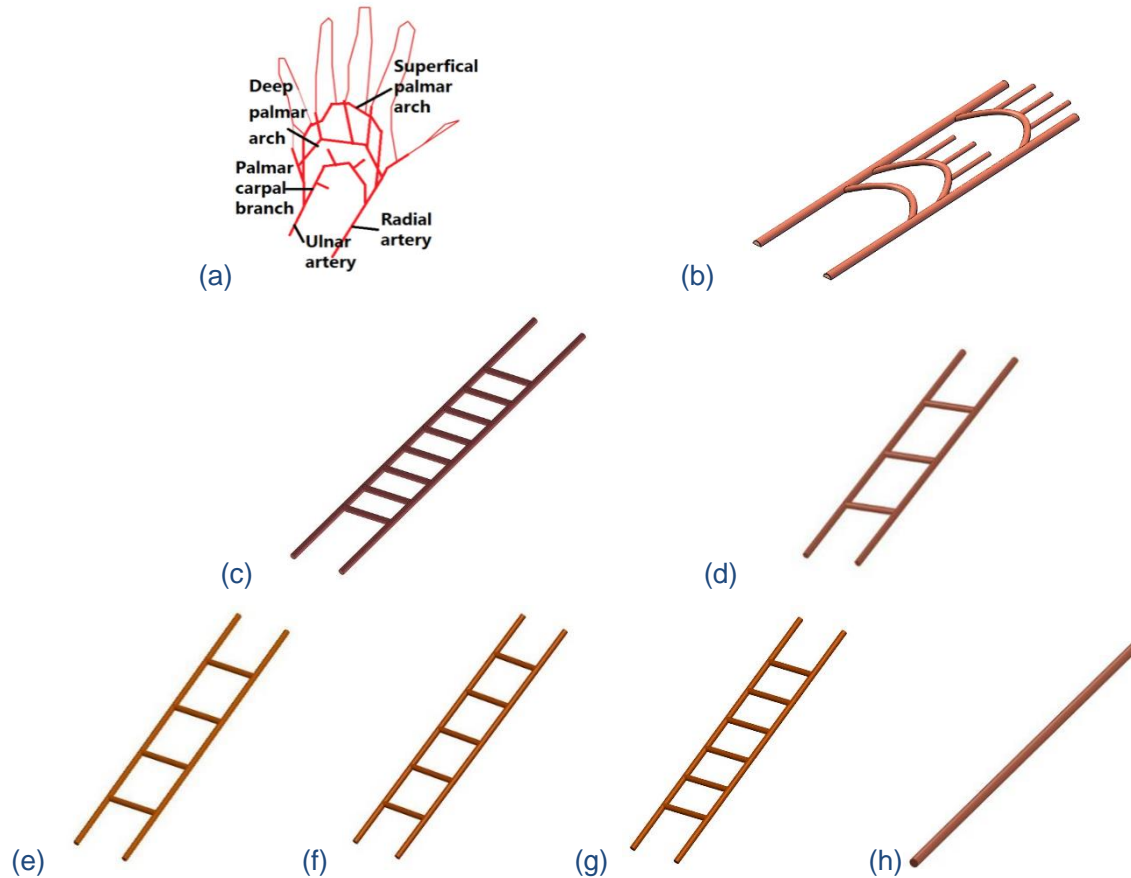


Figure 3-1 Numerical models: (a) real vessels in hand; (b) numerical vessel structure in hand; (c) connected-tubes model; (d) three-connected-tubes model; (e) four-connected-tubes model; (f) five-connected-tubes model, and (g) single tube model

The blood vessel model of palmar vessels is shown in Figure 3-1(a). The two examples of constructed models are indicated in Figure 3-1 (b) and Figure 3-1 (c). In our simulation, the numbers of connected tubes in Figure 3-1 (c) are 3, 5, 6, 8, 16, and 32, respectively. The diameter of the tubes is 2 mm, and the first connected tubes are located at 25 mm points on the main tubes. The connected tubes are spaced at 10 mm intervals. The three-connected-tubes vessel model shown in Figure 3-1 (d) includes five tubes simplified from palmar arteries. Models with tubes of 1mm, 2 mm, and 4 mm diameter were investigated separately. The length of the two main tubes is 100 mm, and the length of the connected

tubes is 20 mm. The connected tubes are spaced at 25 mm intervals. The four-connected-tubes vessel model is shown in Figure 3-1 (e) with connected tubes spaced at 20 mm intervals. The five-connected-tubes vessel model is shown in Figure 3-1 (f) and the connected tubes are located at the 17 mm, 33.5 mm, 50 mm, 66.5 mm, and 83 mm points on the main tubes. The six-connected-tubes vessel model is shown in Figure 3-1(g) and the connected tubes are located at the 18.75 mm, 31.25 mm, 43.75 mm, 56.25 mm, 68.75 mm, and 81.25 mm points on the main tubes. The diameter of the tubes in the four-connected-tubes vessel model, the five-connected-tubes vessel model and the six-connected-tubes vessel model is 2 mm. The single tube model shown in Figure 3-1 (h) was also studied as a comparison. The density of the blood is set as  $1050\text{kg/m}^3$ , and non-Newtonian properties are determined by the Casson model. The nonlinear effect of the vascular system and its relationship to the low frequencies were investigated in a three-connected-tubes model using ANSYS CFX. The actual velocity waveform<sup>160</sup> as shown in Figure 3-2 is used to simulate the inlet velocity with different frequencies in the radial artery. The no-slip wall boundary condition was adopted to the vessel wall.

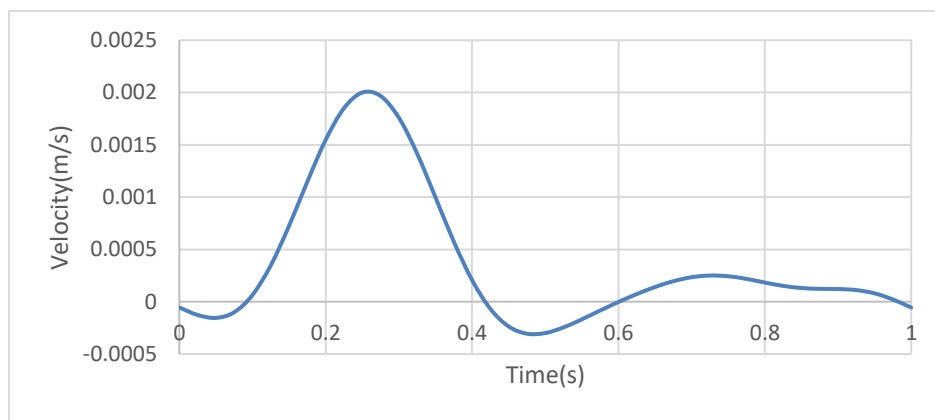


Figure 3-2 Inlet velocity for numerical simulations (modified from a report study<sup>160</sup>)

### 3.2 The Casson model

The blood is a multiphase flow that contains plasma and three main types of cells, namely red blood cells, white blood cells, and platelets. As a result, blood has a significantly non-Newtonian behaviour<sup>161</sup>. A non-Newtonian fluid is one whose viscosity can change under force, which indicates that the shear stress and the shear strain rate in the blood do not simply maintain a linear relationship. As shown in Figure 3-3, normal human blood

exhibits shear-thinning behavior compared to Newtonian behavior (hardened red blood cells in plasma). The red cells are a tangled network of aggregated cell structures that disorganize the blood flow streamlines when the shear rate is less than a critical value, and consequently, the apparent blood viscosity is extremely high at low shear rates or shear stress. With the shear rate or shear stress increasing, the linear aggregates of blood cells gradually disintegrate, and the apparent viscosity decreases and approaches to an asymptotic value. In small capillary hemodynamic, the diameter of vessels is commensurate to the diameter of red blood cells, so red blood cells are subject to drift to the capillary center and form a cell-free layer which is a layer of plasma along the vascular wall<sup>162</sup>. As a result, the viscosity of blood is decreased with increasing vessel size when shear rates are high, and this phenomenon is referred to Fahraeus and Lindqvist effect. However, when vessel diameter is large enough compared to the red blood cell diameters, the blood viscosity is approximately constant in these large vessels and the blood flow maintains bulk properties<sup>162</sup>. The Casson model is one of the most popular models that describe the blood flow viscosity in narrow arteries. It has been demonstrated by many researchers<sup>163-165</sup> that this model satisfactorily predicts blood flow in narrow arteries at low shear rates. The Casson model considers both shear-thinning behavior and a parameter in Casson fluid, namely the yield stress of the blood.

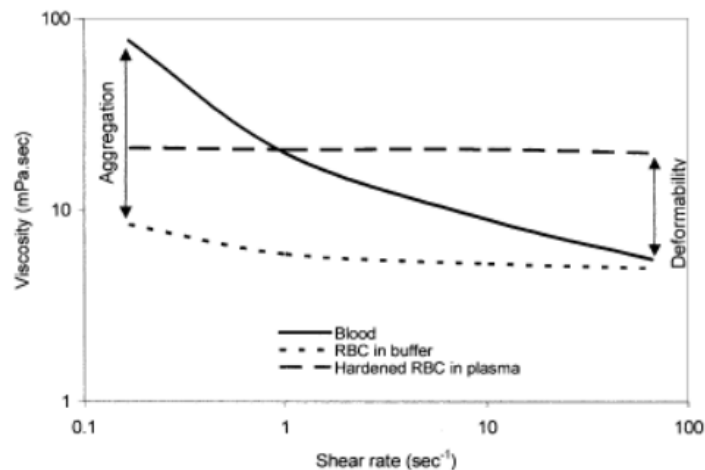


Figure 3-3 Shear-thinning effect (RBC-Red blood cell)<sup>162</sup>

In the Casson model, blood is modeled as an isotropic, homogeneous, non-Newtonian fluid.

$$\sqrt{\tau} = \sqrt{\tau_0} + \sqrt{\kappa\dot{\gamma}}$$

where  $\tau_0$  is the yield stress,  $\dot{\gamma}$  is the shear rate, and  $\kappa$  is the viscosity coefficient of Casson fluid. The apparent viscosity is obtained from the equation below and reads,

$$\sqrt{\mu} = \sqrt{\frac{\tau_0}{\dot{\gamma}}} + \sqrt{\kappa}$$

where the model parameters are chosen according to Docorato's report<sup>166</sup>:  $\tau_0 = 4 \times 10^{-3} Pa$ ,  $\kappa = 3.5 \times 10^{-3} Pa \cdot s$ .

### 3.3 Validation of numerical models

#### 3.3.1 The validation of the turbulence model

The pulsatile flow often tends to be turbulent. In physiological flows, additional complexity is created by the complex geometry and non-Newtonian fluids. Even the flow transition of laminar to turbulence in simpler Newtonian fluids pulsating in straight tubes is not well understood. It is reported in earlier studies<sup>167-171</sup> that the threshold Reynolds number for the onset of turbulence increases with the Womersley number. The Womersley number is 1.28 for the case of 2 mm diameter and 1 Hz frequency. The input period for the simulation has a main period of 5 s, which means that the Womersley number is very small in the simulation. Thus, the Reynolds number of transition threshold in our cases might be extremely low. The flow in our simulation cases might be turbulence. So, the turbulence model Shear Stress Transport (SST) is used. To investigate the accuracy of the model, the three-connected model with 2 mm diameter and 2 mm/s velocity is simulated with the laminar model and SST model, separately. The mean wavelet results are shown in Figure 3-4, where the heart beating period is 1 Hz and the main cycle is 0.2 Hz. The frequency results for simulation using SST show an accurate representation of the input frequencies. The frequencies observed in the results for simulations using Laminar are 0.8 Hz and 0.2 Hz. The frequency 1Hz in the actual condition is shifted to 0.8Hz, which cannot reflect the real situation. Thus, it is reasonable to use the SST as the turbulence model in the simulations.

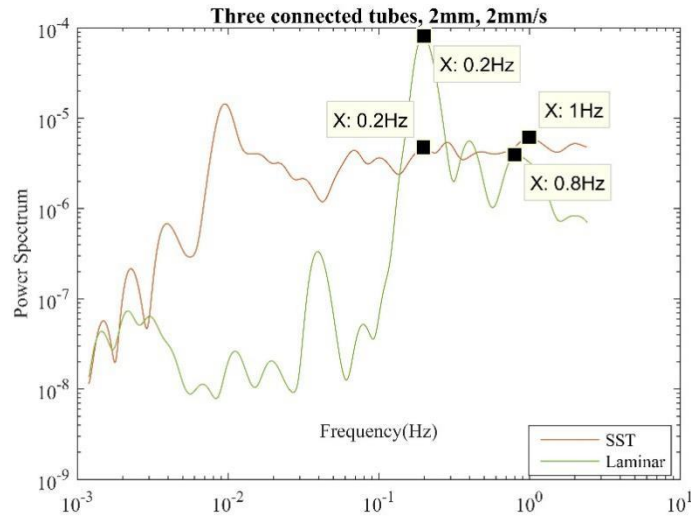


Figure 3-4 The mean wavelet results for the point on the first connection for the three-connected tube model using different turbulence model

### 3.3.2 Effect of time step and significant figures of $\pi$ on simulation results

#### 3.3.2.1 Single tube model, $\pi$ with different significant figures, time steps of 0.05 s and 0.01 s

From a basic conjecture, the value of  $\pi$  and the selected time step are two possible contributors to numerical errors. To highlight low-frequency oscillations that are possibly introduced by errors, a low pass filter is used to cut the input frequency. Figure 3-5 demonstrates the filtered wavelet analysis results for a single tube model. The inlet frequency was 1 Hz and  $\pi$  was estimated to be 3.1415. With two different time steps, the results include different low-frequency components. Since the input is a 1 Hz signal for all these simulations, such low frequencies may be attributed to numerical errors. Because both results involve the low-frequency component of  $\sim 0.1$  Hz, it is likely that frequencies caused by errors interfere with the studies of vasomotion.

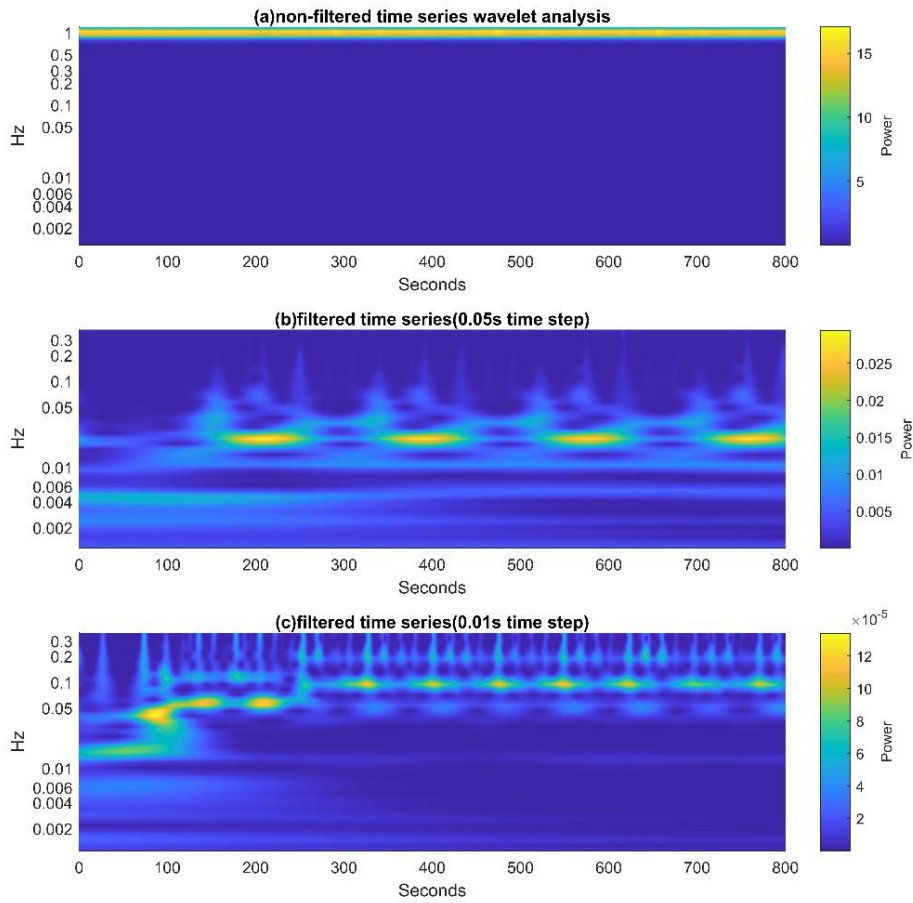


Figure 3-5 Single tube model, inlet oscillating at 1Hz, different time steps,  $\pi=3.1415$ , wavelet analysis

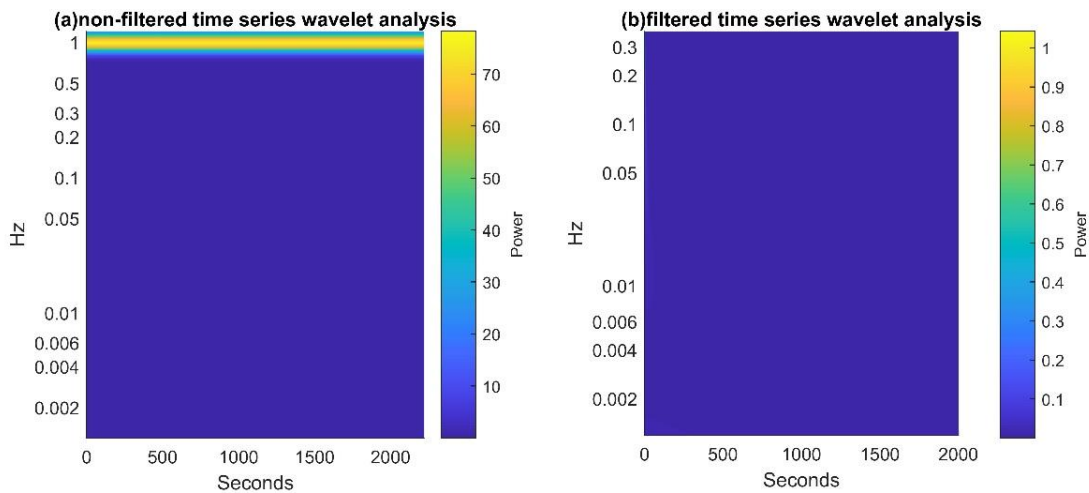


Figure 3-6 Single tube model, inlet oscillating at 1 Hz, time step of 0.01 s,  $\pi=3.14159267$ , wavelet analysis

Figure 3-6 shows the wavelet analysis results of the single tube model in which the inlet frequency is 1 Hz, the time step is 0.01 s, and  $\pi$  round to 8 significant figures and is approximated to 3.1415927. Similar to the two cases mentioned above, a low pass filter is used. No low frequency is observed in the filtered results. The mean wavelet results are computed as the time-averaged power spectrum from wavelet analyses and demonstrated in Figure 3-7. At 1 Hz input, the processed power spectrum curve of the (0.01 s, 3.14159267) case is flat in  $\sim 0.1$  Hz frequency band which means that low-frequency components are eliminated by adopting a more accurate  $\pi$  value.

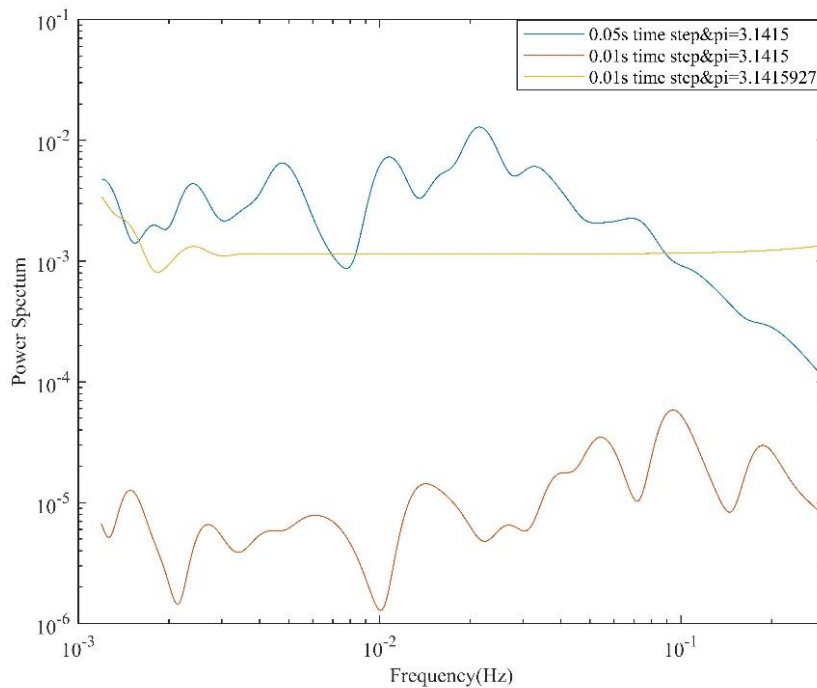


Figure 3-7 Single tube model, inlet oscillating at 1Hz, mean wavelet analysis

### 3.3.2.2 Three-connected-tubes model, $\pi$ with 8 significant figures, time step of 0.01 s

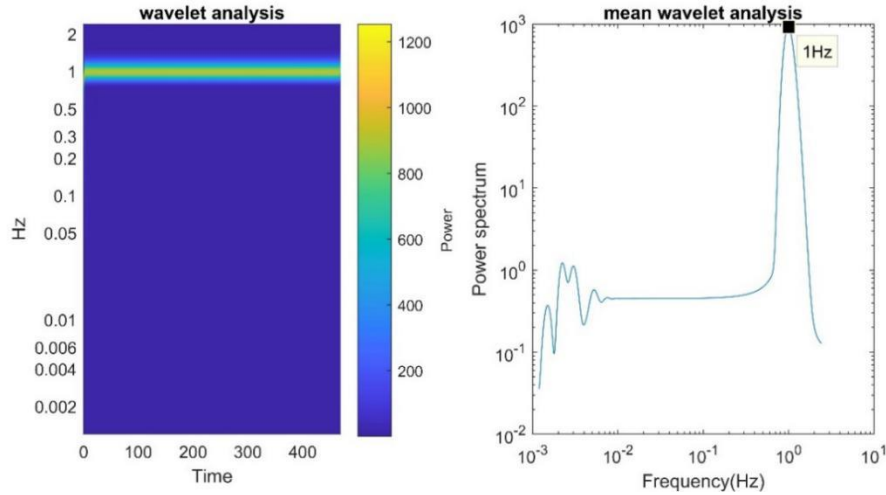


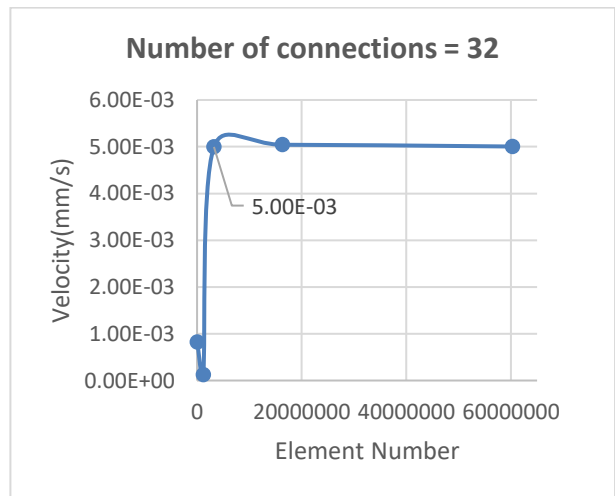
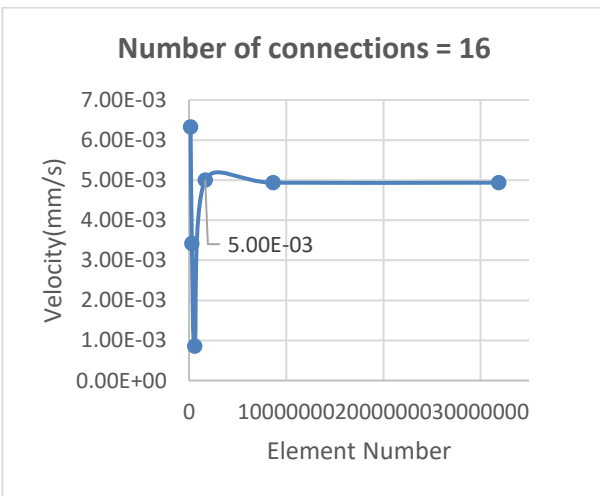
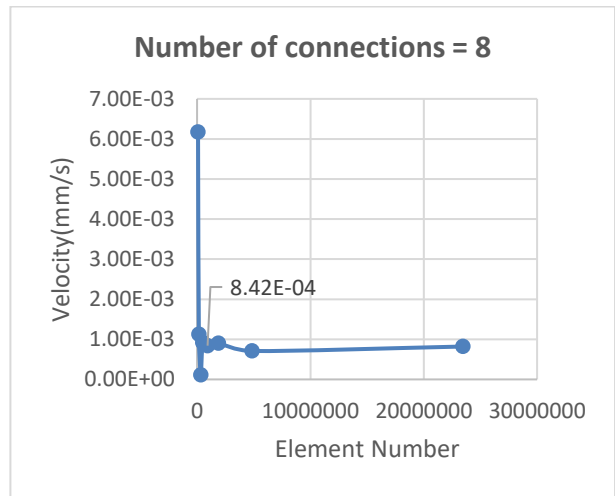
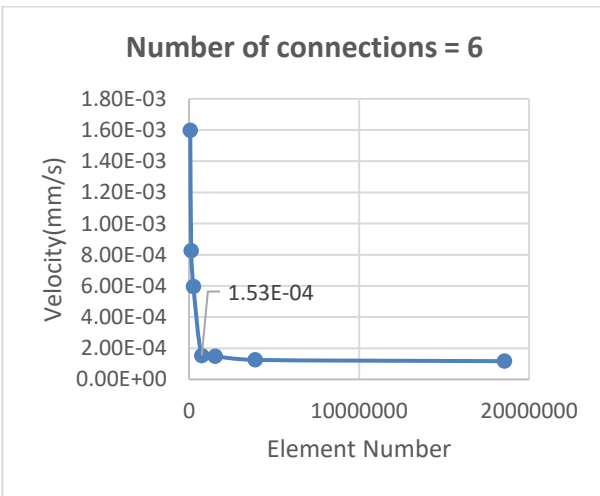
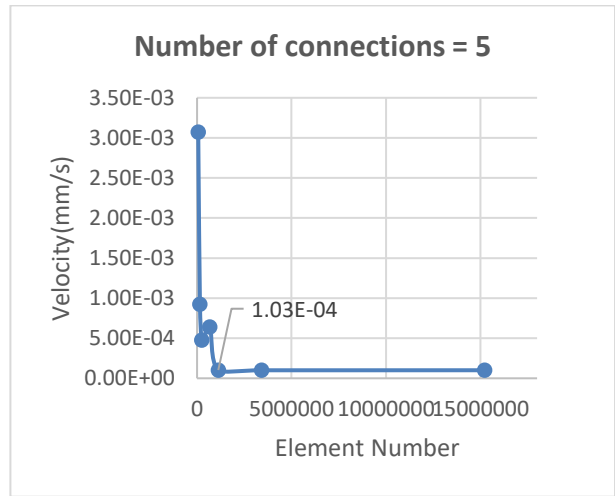
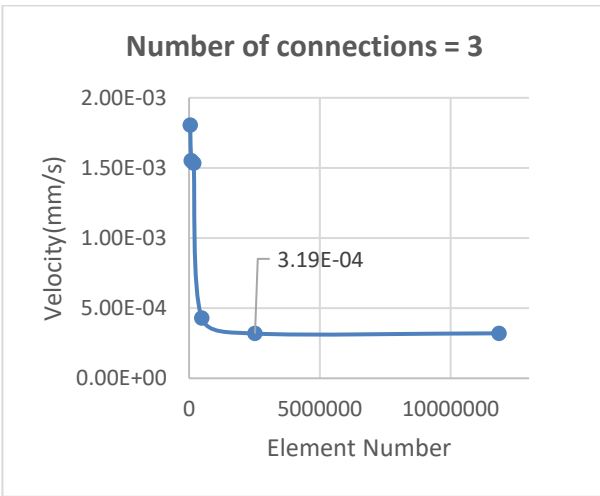
Figure 3-8 Three-connected-tubes model, inlet oscillating at 1 Hz, wavelet analysis and mean wavelet analysis

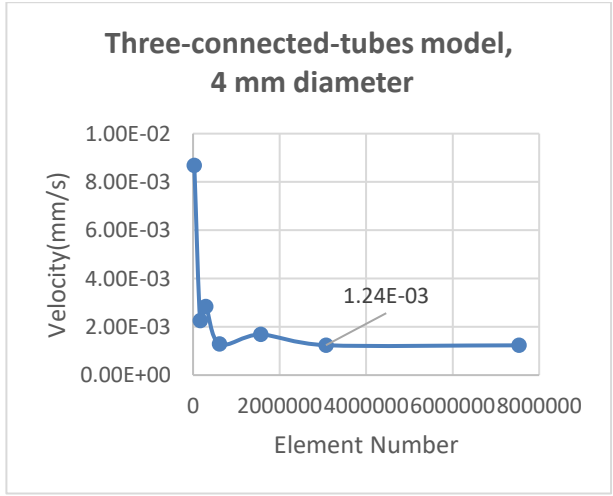
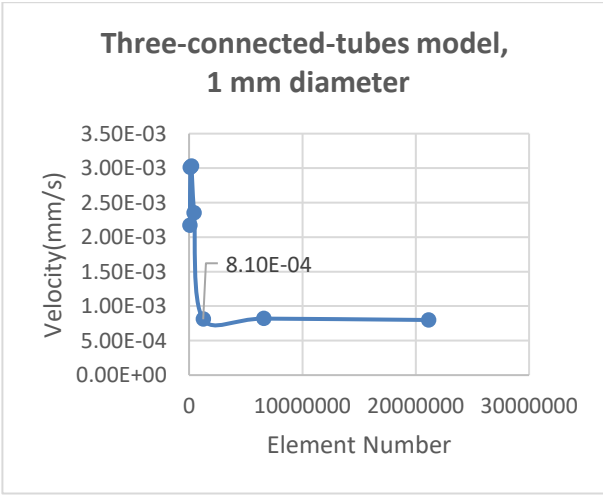
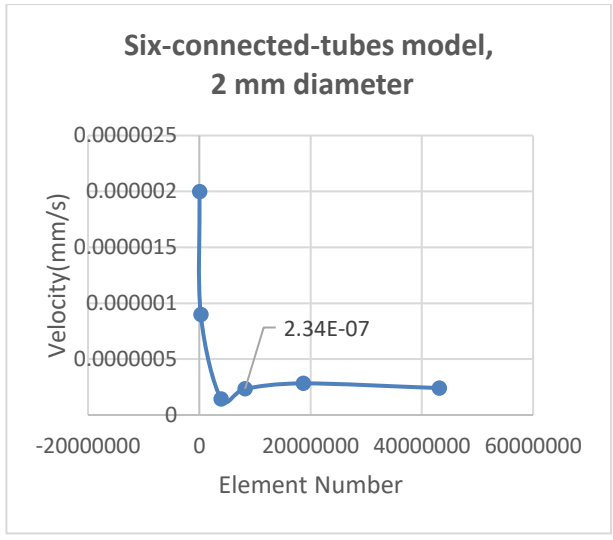
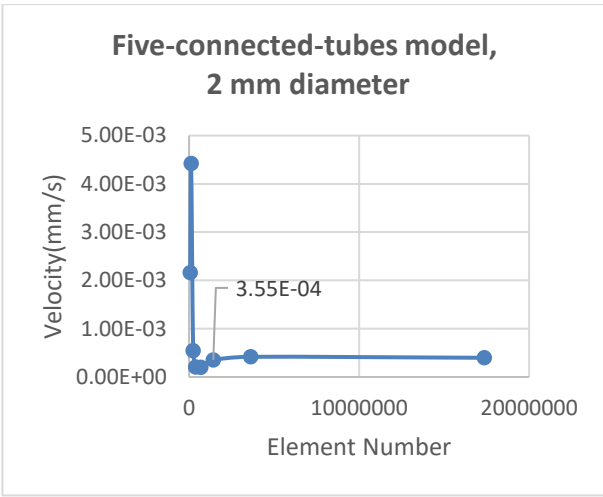
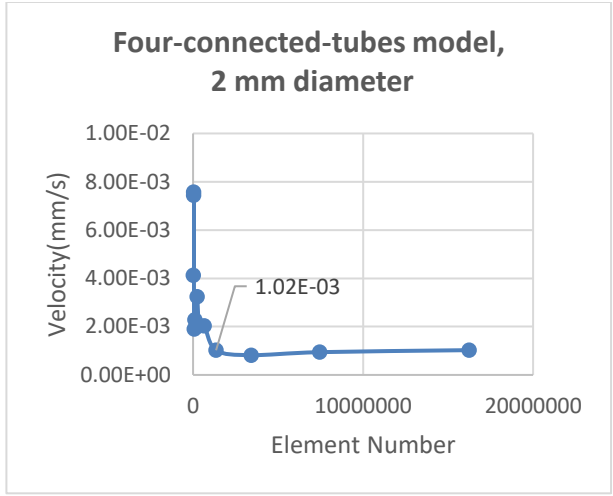
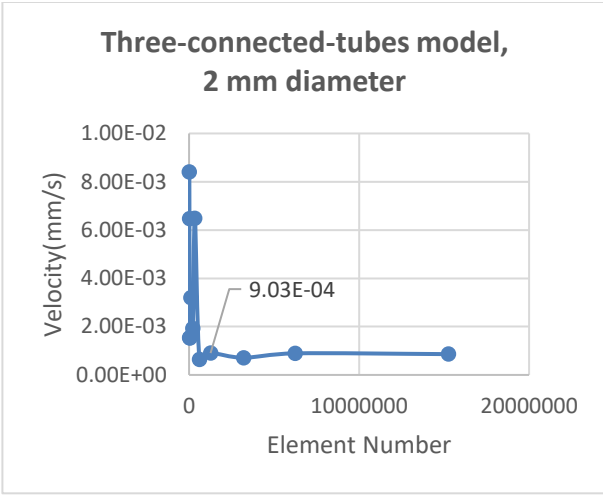
To further validate whether the time step being 0.01 s and  $\pi$  estimated to 8 significant figures are reasonable settings for connected-tubes models, the three-connected-tubes model with 1Hz inlet frequency is simulated. As shown in Figure 3-8, no  $\sim 0.1$  Hz oscillations are observed which means that 0.01 s time step and  $\pi$  estimated to 8 significant figures are reasonable settings for models.

### 3.3.3 Mesh independence

We validated the mesh independence by simulating a steady flow and detecting the velocity on the first connection of the models in Figure 3-1 (c), (d), (e), and (f). The inlet velocity was set to 2 mm/s. The results of the mesh-independence study are shown in Figure 3-9. The element number for each model is chosen at a point where there is little difference when the mesh is further refined. Thus, the mesh resolution for models in Figure 3-1 (c) with 3, 5, 6, 8, 16, and 32 connections are 2522139, 1123259, 747613, 928151, 1664500, and 1664500, respectively. An element number of 1264830 is chosen for the three-connected-tubes model with 2 mm diameter, 1352966 for the four-connected-tubes model, 1423657 for the five-connected-tubes model, and 8231819 for the six-connected-tubes model. Considering a high level of frequency accuracy and computational cost, the mesh resolutions with 1247633, 3071290, and 923742 elements

are chosen for the three-connected-tubes models with 1 mm, 4 mm and 8mm diameter, respectively.





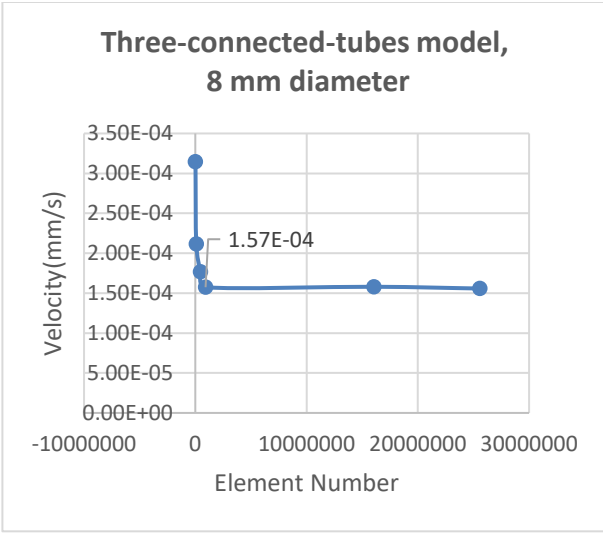


Figure 3-9 Mesh independence

### 3.4 Low frequency induced by input period variation

#### 3.4.1 0.2 Hz frequency input for different models

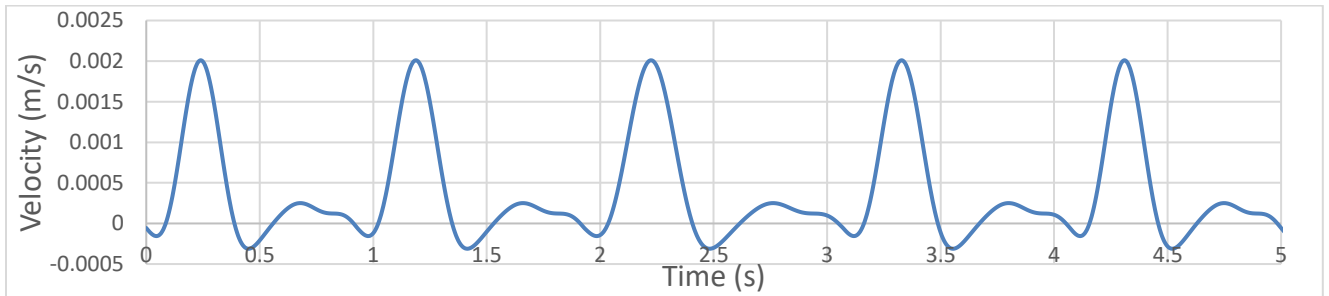


Figure 3-10 Velocity input with a period of 5s

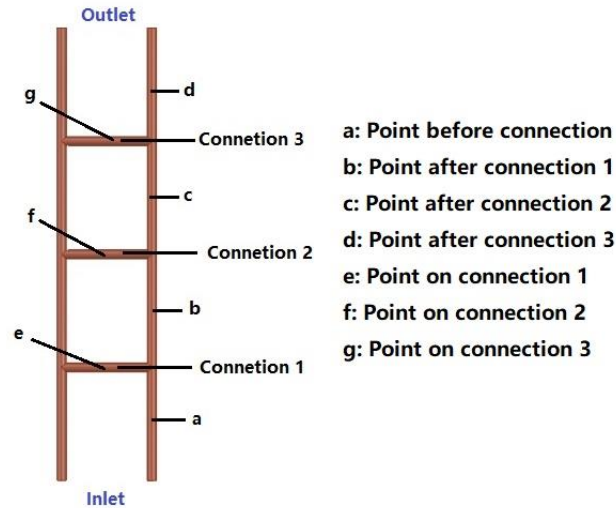


Figure 3-11 Monitor points on the model

In order to verify the influence of heart period variation on blood flow oscillation, the main period of the inlet velocity signal was set to 5 s, including five different input heart periods, i.e., 0.93 s, 1 s, 1.14 s, 1 s, and 0.93 s. The velocity profile is shown in Figure 3-10. The wavelet analysis results for the three-connected-tubes model and single tube model are shown in Figure 3-12, where  $\sim 1$  Hz has ultrahigh PSD compared to other lower frequency oscillations. Hence, mean wavelet analysis was implemented to identify lower frequency components. Figure 3-13 shows the mean wavelet results for the three-connected-tubes model and single tube model. The blue curve shows the results for the single tube model, where 0.984 Hz is the mean heart rate; 0.2 Hz is the input frequency, and 0.4 Hz and 1.97 Hz are the harmonic frequency of 0.2 Hz and 0.984 Hz, respectively. The red curve shows the results for the three-connected-tubes model. The input frequencies (0.2 Hz and  $\sim 1$  Hz) and several low-frequency components (0.01 Hz to 0.1 Hz) are found at the point before connection, i.e., at monitor point a. The oscillation of blood flow in the three-connected tubes model has several low frequencies compared to that in the single tube model. Thus, low frequencies in simulation results of the three-connected-tubes model are not only induced by the variation of heart period but also caused by the nonlinear vasculature. To further investigate whether various locations have different low-frequency oscillations, data from other monitors, as shown in Figure 3-11, are analyzed.

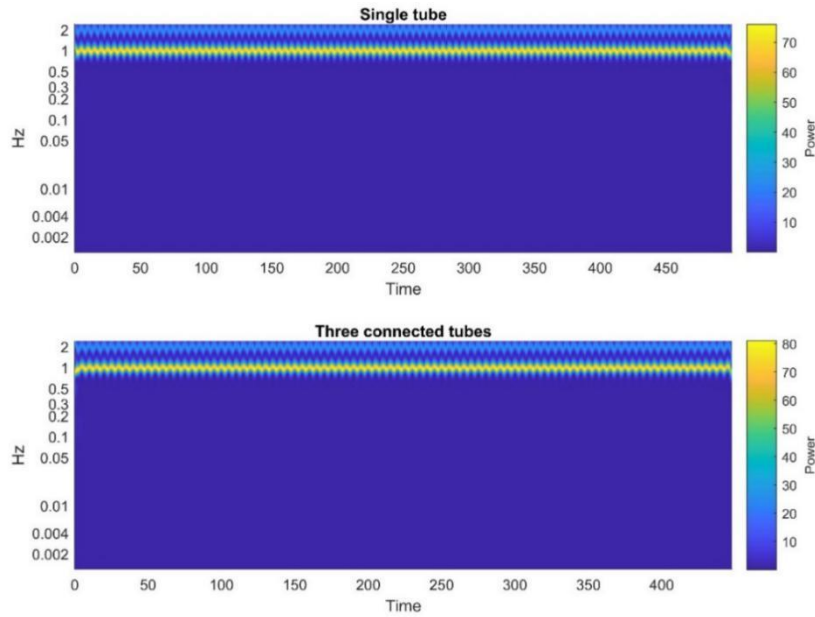


Figure 3-12 Single tube model and three-connected-tubes model, point before connection, 0.2 Hz input frequency, wavelet analysis

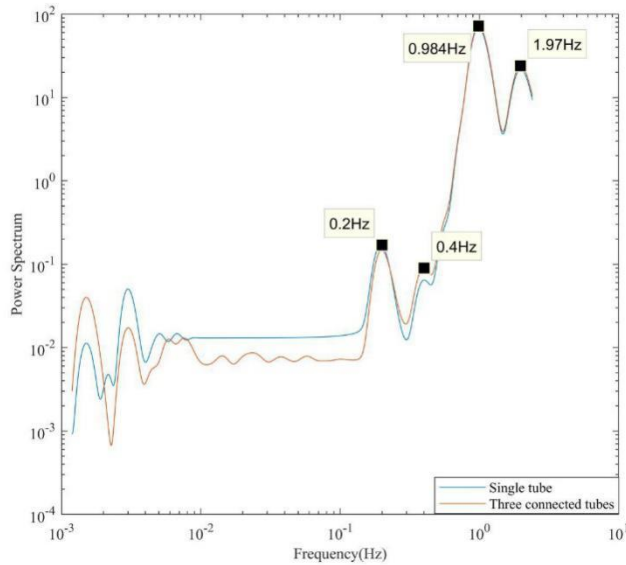


Figure 3-13 Single tube model and three-connected-tubes model, point before connection, 0.2 Hz input frequency, mean wavelet analysis

Figure 3-14 displays the wavelet analysis results at various locations (monitor points e, f, and g) on the three-connected-tubes model. Figure 3-15 displays the results of the four points (a, b, c, and d) on the straight tube before and after connections. The power mainly concentrates at ~1Hz in the wavelet analysis results of the points on the straight tube,

while the results of the points on three connections exhibit a pattern where the power spectrum is not purely concentrated at ~1 Hz, but spreads in the region from 0.5 Hz to 2 Hz. Meanwhile, at these points on connections, the power spectrum of low-frequency oscillations varies with time which resembles the frequency feature discovered in the experiment data in Figure 3-16. Linear regression analysis helps to find the relationship between the inlet velocity and the computed velocity of the points on the connections (e, f, and g). The coefficients of determination  $R^2$  are 0.007759, 0.002389, and 0.004832, respectively, which are close to zero, indicating that the correlation between the inlet velocity and the computed velocity of the points on the connections is nonlinear. In contrast, the linear regression of the input velocity and the computed velocity of the point on the single tube generates an  $R^2$  of 0.992135 which is close to one and means a linear correlation. As a summary, the linear regression analysis results of the inlet velocity and computed velocity in the three-connected-tubes model show that the interconnected vasculature induces a nonlinear effect in the flow velocity at the points on the connections.

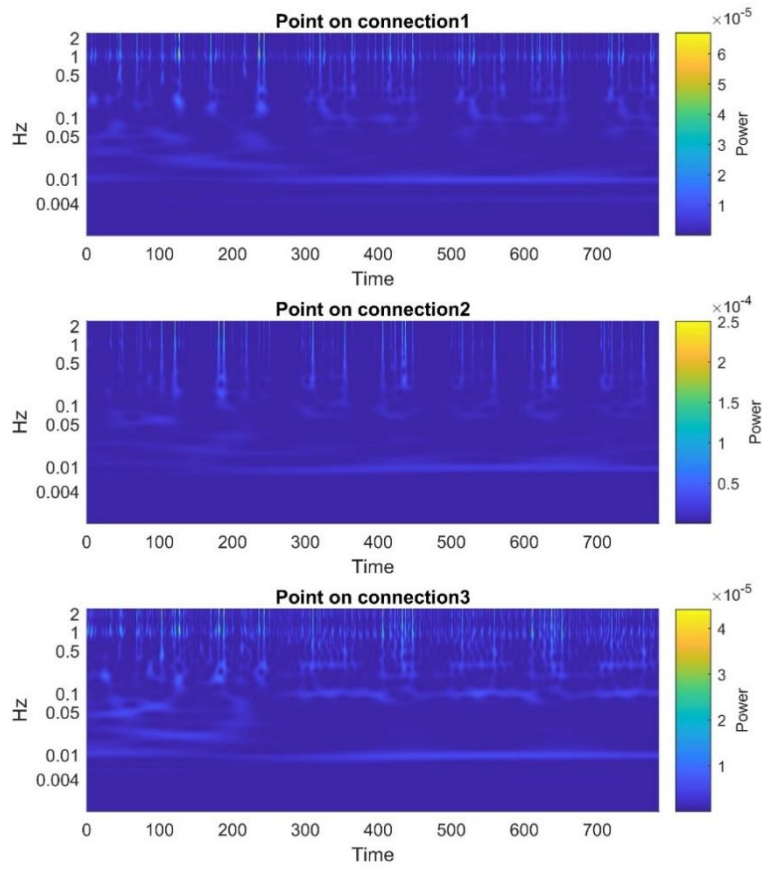


Figure 3-14 Three-connected-tubes model, point on connections, 0.2 Hz input frequency, wavelet analysis

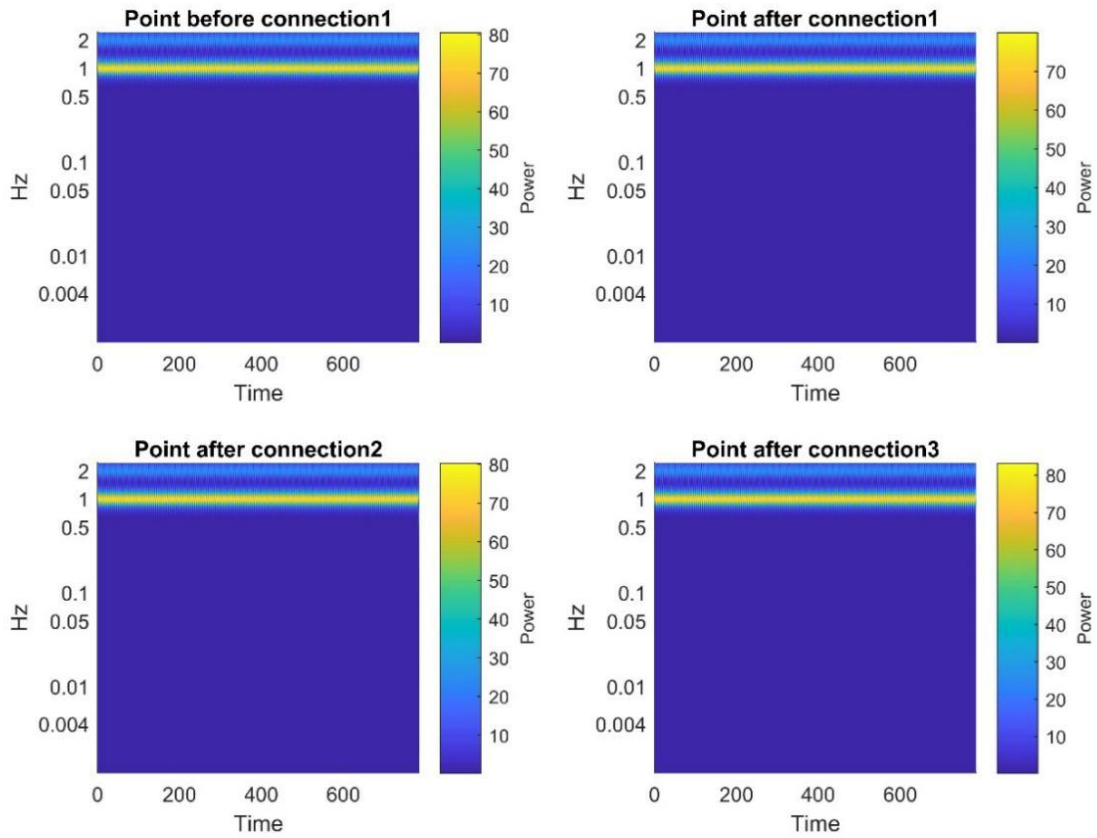


Figure 3-15 Three-connected-tubes model, point before and after three connections, 0.2 Hz input frequency, wavelet analysis

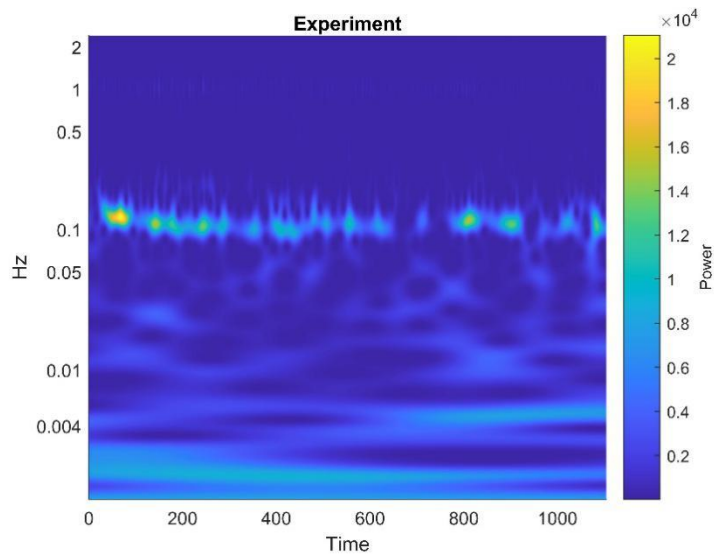
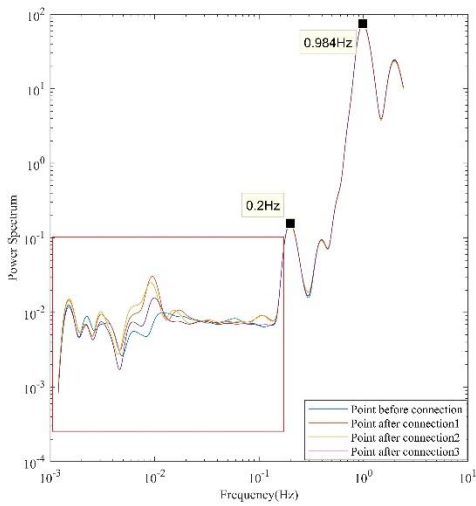
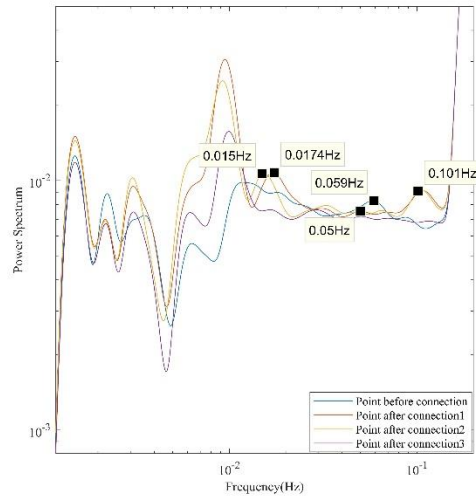


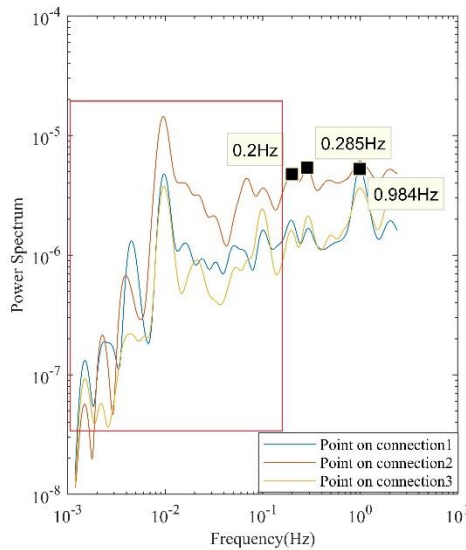
Figure 3-16 Experimental data, wavelet analysis



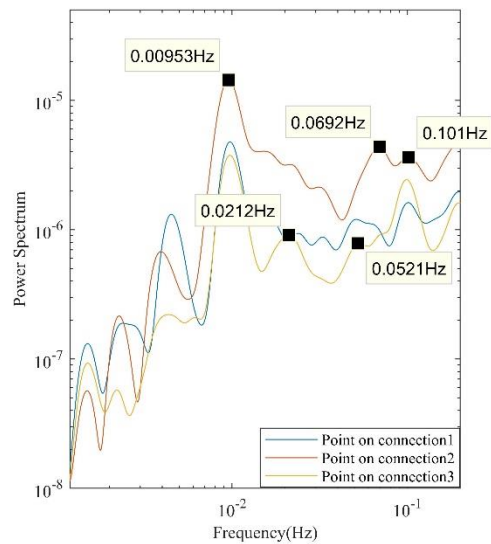
(a)



(b)



(c)



(d)

Figure 3-17 Three-connected-tubes model, 0.2 Hz input frequency, mean wavelet analysis

Mean wavelet analysis is performed for clearer observation of oscillation frequencies for the three-connected-tubes model, and the results are shown in Figure 3-17. Curves within the red box in the graphs on the left, Figure 3-17 (a) and (c), are magnified and displayed in the graphs on the right, Figure 3-17 (b) and (d), respectively. As shown in Figure 3-17 (a), the inlet frequencies (0.2Hz and  $\sim 1$ Hz) at the points before and after connections play a dominant role in their flow oscillations. Meanwhile, in the results on the connections shown in Figure 3-17 (c), the vasomotion related frequencies ( $\sim 0.1$ Hz) have a higher

power spectrum than that of inlet frequencies. In Figure 3-17 (b) and (d), several low frequencies oscillations are identified, i.e., 0.00953 Hz, 0.052 Hz, and 0.101 Hz. The 0.101 Hz frequency might be the subharmonic of 0.2Hz input frequency. The power spectrum at 0.0953 Hz at the monitor point f on connection 2 is much higher than that at monitor point e on connection 1 and g on connection 3, because the flow through connections 1 and 3 are influenced by inlet and outlet settings. The main straight tubes and the connections in the model are compared to arteries and branches in the vascular system, respectively. The findings above comply with the two facts below: (i) the vasomotion is mainly observed in microvasculature<sup>84,97,172,173</sup>; and (ii) the power spectrum of 0.001 ~ 0.1 Hz may be higher than that at heart rate<sup>174,175</sup>. By comparing the results of 0.2 Hz input frequency from the single tube model with those from the three-connected-tubes model, we found that these ~0.1 Hz low frequencies are generated by the interaction of geometry. At the same time, for the three-connected-tubes model shown in Figure 3-8 with 1Hz constant inlet frequency, no low frequency is observed from the results. Therefore, the generation of low-frequency oscillations needs not only the interaction of geometry but also the variation of the input period. It concludes that the low-frequency oscillations (0.01 ~ 0.1 Hz) are most likely due to the interconnected vessel geometry and the frequency change in the cardiac cycle.

#### *3.4.1.1 Effect of the diameter of the tubes and inlet velocity*

The tubes of 1 mm and 4 mm diameter were simulated to investigate the influence of the tube diameter on frequencies. The mean wavelet analysis results are shown in Figure 3-18. From Figure 3-17 and Figure 3-18, the model with 2 mm diameter tubes induces the most complex low-frequency components. And as the diameter of the tubes increases to 4 mm, the complexity of low-frequency components decreases. Further, the mean wavelet analysis result for model with 8 mm diameter tubes is nearly flat below 0.2 Hz. We can speculate from the mean wavelet results that the complexity of the induced low-frequency components decreases with increasing vessel diameter after a certain size of the diameter. The coefficients of determination  $R^2$  between the inlet velocity and the computed velocity at the point e on the first connection are shown in Table 3-1. Either the model with 2 mm, 4mm and 8 mm diameter has an  $R^2$  close to zero. The model with 1

mm diameter tubes has the maximum  $R^2$  of 0.131068. The results show that the diameter of vessels has influence on the induced nonlinear effect on the flow velocity at the points on the connections.

Table 3-1 The coefficients of determination ( $R^2$ ) of the inlet velocity and the computed velocity of the point on the first connections, 2mm/s, different diameter

Diameter	1 mm	2 mm	4 mm	8 mm
$R^2$	0.131068	0.007759	0.065449	0.011931

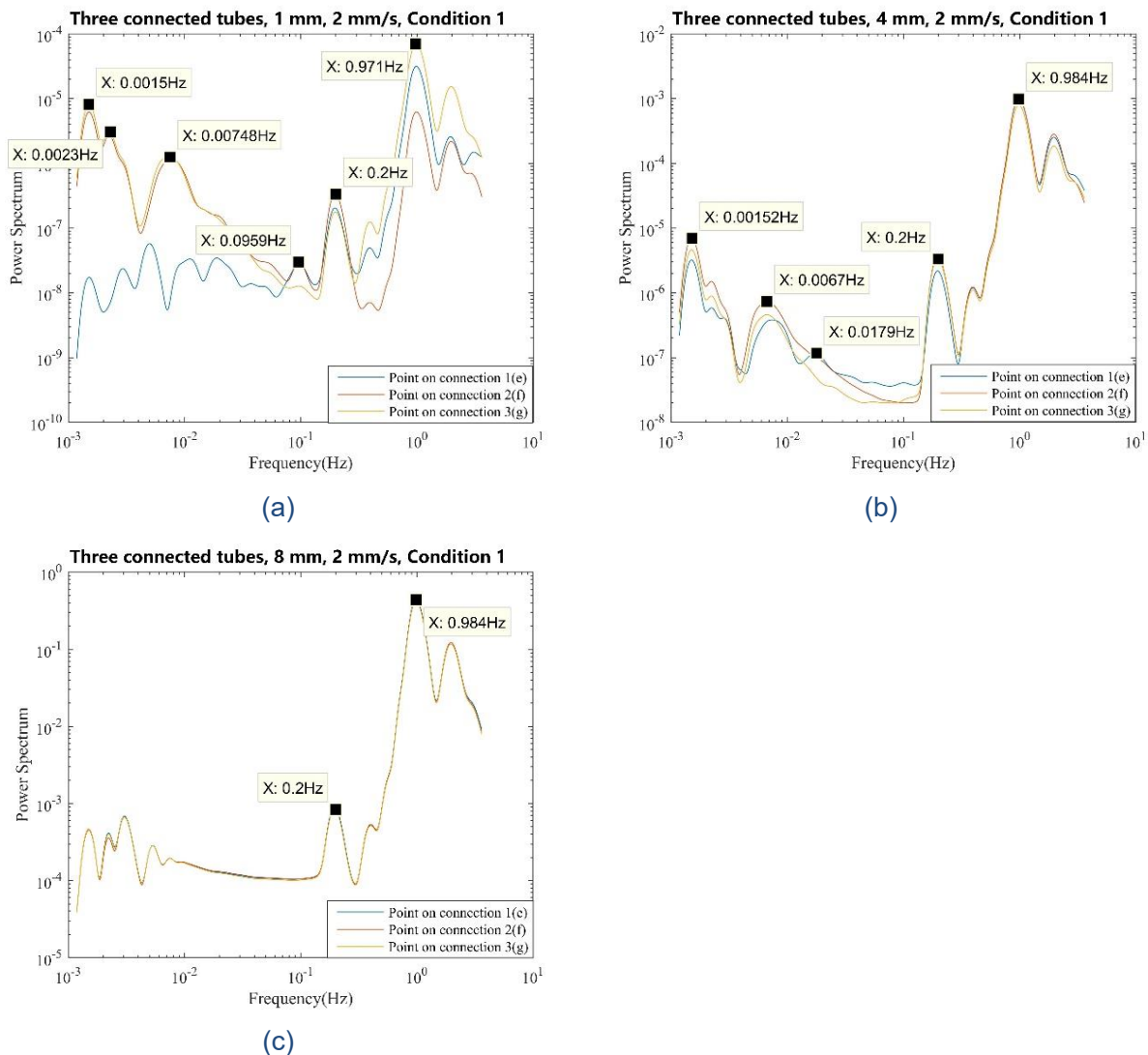


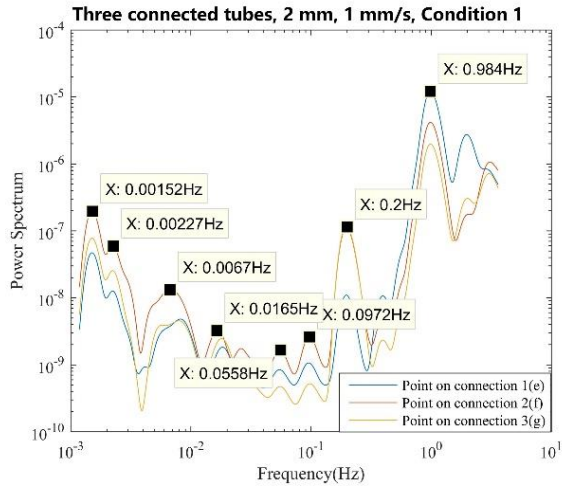
Figure 3-18 Three-connected-tubes model, points on the connections, mean wavelet analysis, different diameters: (a) 1 mm, (b) 4 mm and (c) 8 mm

From Figure 3-19, using a maximum inlet velocity of 4 mm/s and 8 mm/s will induce several low frequency oscillations, i.e., 0.0959 Hz and 0.0177 Hz for 4 mm/s and 0.1Hz and 0.027Hz for 8 mm/s. Compared to a maximum inlet velocity of 4 mm/s and 8 mm/s, using a maximum inlet velocity of 1 mm/s induces more complex low-frequency components, i.e., 0.0972 Hz, 0.0558 Hz, and 0.0165 Hz. It can be speculated that the low-frequency components induced at low velocities are more complex than at high velocities. The coefficients of determination results are shown in Table 3-2, where the simulations with a maximum inlet velocity of 1 mm/s and 4 mm/s have R<sup>2</sup> similar results of around ~0.5, in contrast, the results of R<sup>2</sup> for models with 2 mm/s and 8 mm/s are close to zero.

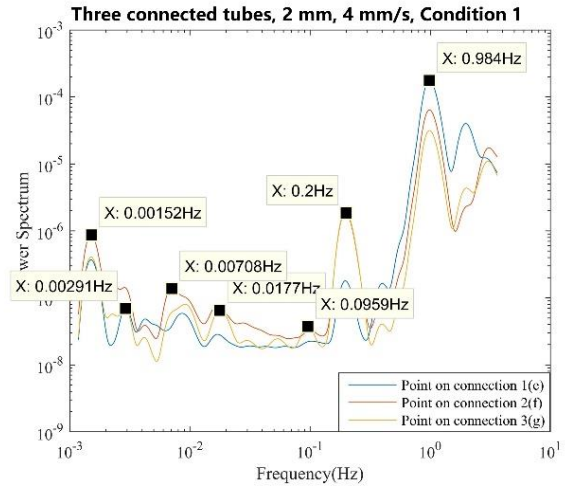
The Womersley number is used to describe the frequency of pulsating flow associated with viscous effects. It is calculated by  $\alpha = \frac{D}{2} \sqrt{\frac{2\pi f}{\gamma}}$ , where  $\alpha$  is the Womersley number, D is the vessel diameter,  $f$  is the frequency, and  $\gamma$  is the dynamic viscosity of blood. The Womersley numbers for all these eight models range from 0.5 to 2, corresponding to the artery. Then, the three-connected-tubes model with a 2 mm diameter is scaled to 1/100 to simulate the arteriole condition whose Womersley number is about 0.01. Figure 3-20 shows the mean wavelet results for the scaled model with 0.02 mm diameter tubes and 1 mm/s velocity. Several low-frequency oscillations are noted, and there is no obvious relationship between these included low-frequency components and the variation in small vessel diameters. And the result of R<sup>2</sup> between the inlet velocity and the computed velocity point e on the first connections is 0.576280.

Table 3-2 The coefficients of determination (R<sup>2</sup>) of the inlet velocity and the computed velocity at the point on the first connection, different maximum inlet velocities

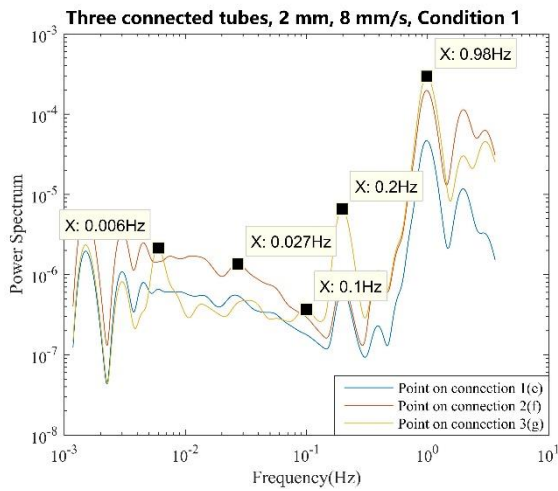
Velocity	1 mm/s	2 mm/s	4 mm/s	8 mm/s
R <sup>2</sup>	0.694723	0.007759	0.703345	0.071927



(a)



(b)



(c)

Figure 3-19 Three-connected-tubes model, points on the connections, mean wavelet analysis, different maximum inlet velocities: (a) 1 mm/s, (b) 4 mm/s and (c) 8 mm/s

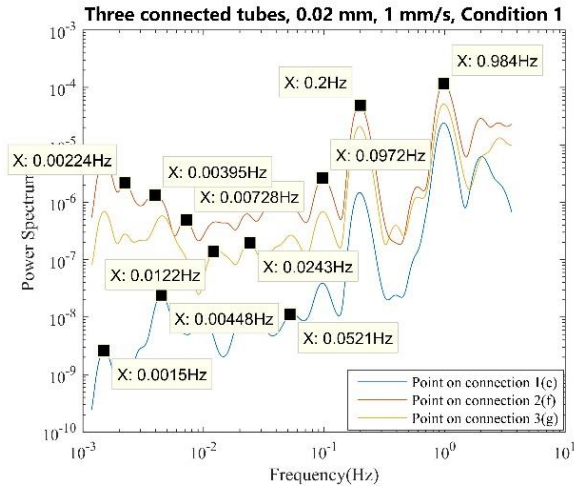


Figure 3-20 Three-connected-tubes model, points on the connections, 0.02 mm, 1 mm/s, mean wavelet analysis

### 3.4.1.2 Effect of the number of the tubes

The number of connected tubes was increased to 4 and 5 to investigate the influence of geometry on frequencies. In Figure 3-17, and Figure 3-21, the number of connected tubes changes from 3 to 5, and several low-frequency oscillations are identified in all these four models. The coefficients of determination results are shown in Table 3-3, where the three-connected-tubes model, five-connected-tubes model six-connected-tubes model have an  $R^2$  close to zero. The four-connected-tubes model has the maximum  $R^2$  of 0.484198.

Table 3-3 The coefficients of determination ( $R^2$ ) of the inlet velocity and the computed velocity at the point on the first connection, different number of connections

Number of connected tubes	3	4	5	6
$R^2$	0.007759	0.484198	0.002775	0.061840

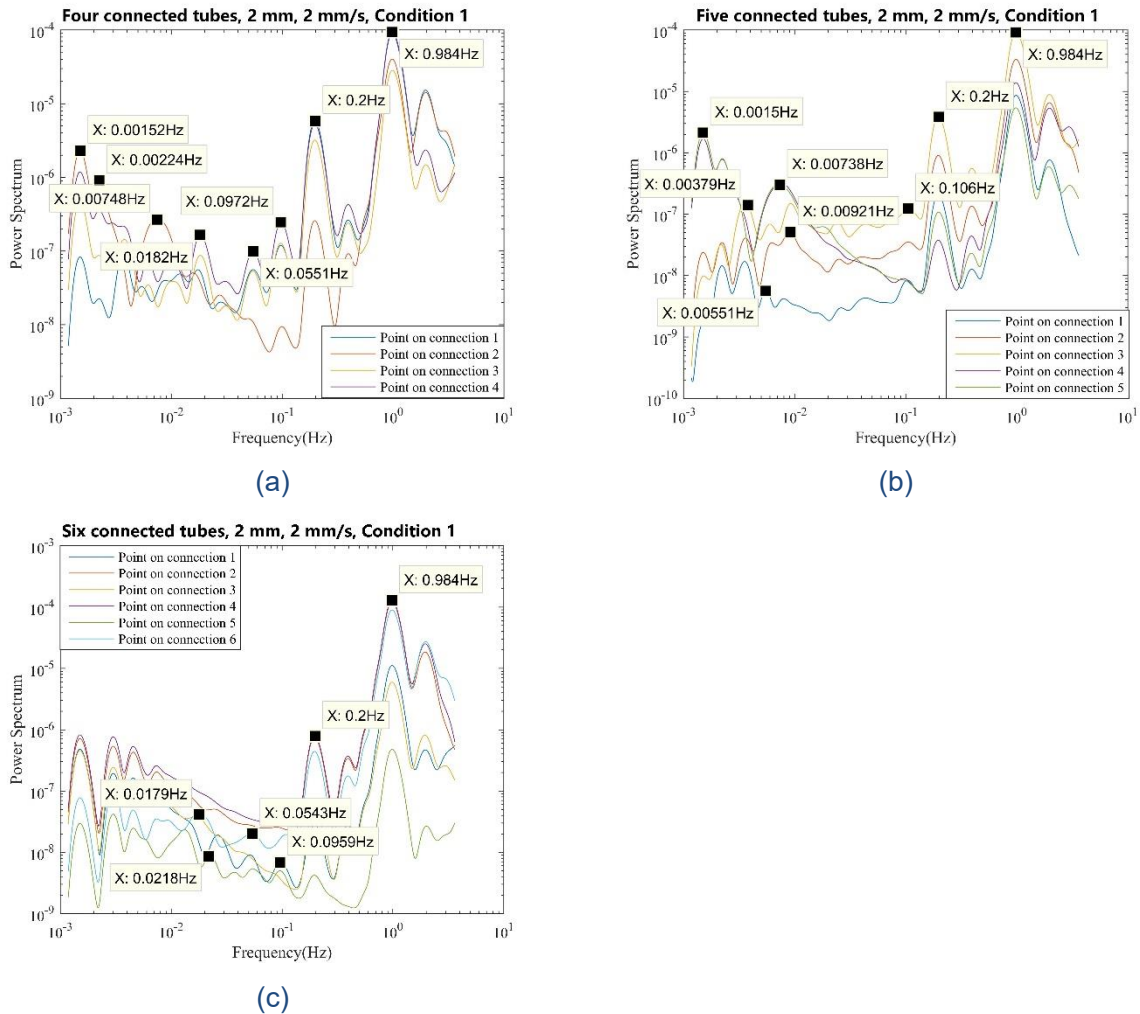


Figure 3-21 Three-connected-tubes model, points on the connections, mean wavelet analysis, different number of connections: (a) four connected tubes, (b) five connected tubes and (c) six connected tubes

### 3.4.1.3 Effect of different open-close states

Different open-close states of the three-connected-tubes model are also studied. Condition 1 and 2 refer to different inlet and outlet settings as shown in Figure 3-22(c) and Figure 3-22(d), respectively. And the mean wavelet results are shown in Figure 3-22 (a) and (b). Under condition 2, low-frequency components, such as 0.075 Hz, are induced and the ~1 Hz frequency still plays a dominant role at monitors on the connected tubes. Different from the results under condition 1, the power spectrum of the point on connection 2 is much lower than that of the point on connections 1 and 3. The coefficients of

determination results are shown in Table 3-4, the  $R^2$  result of condition 2 is close to one which means that there is a linear correlation between the input velocity and the computed velocity at the points on connections. The results indicates that the low frequency oscillations are mainly induced by the vessels with blood flow from the same directions.

Table 3-4 The coefficients of determination ( $R^2$ ) of the inlet velocity and the computed velocity at the point on the first connection, different open-close states

Condition	Condition 1	Condition 2
$R^2$	0.007759	0.822124

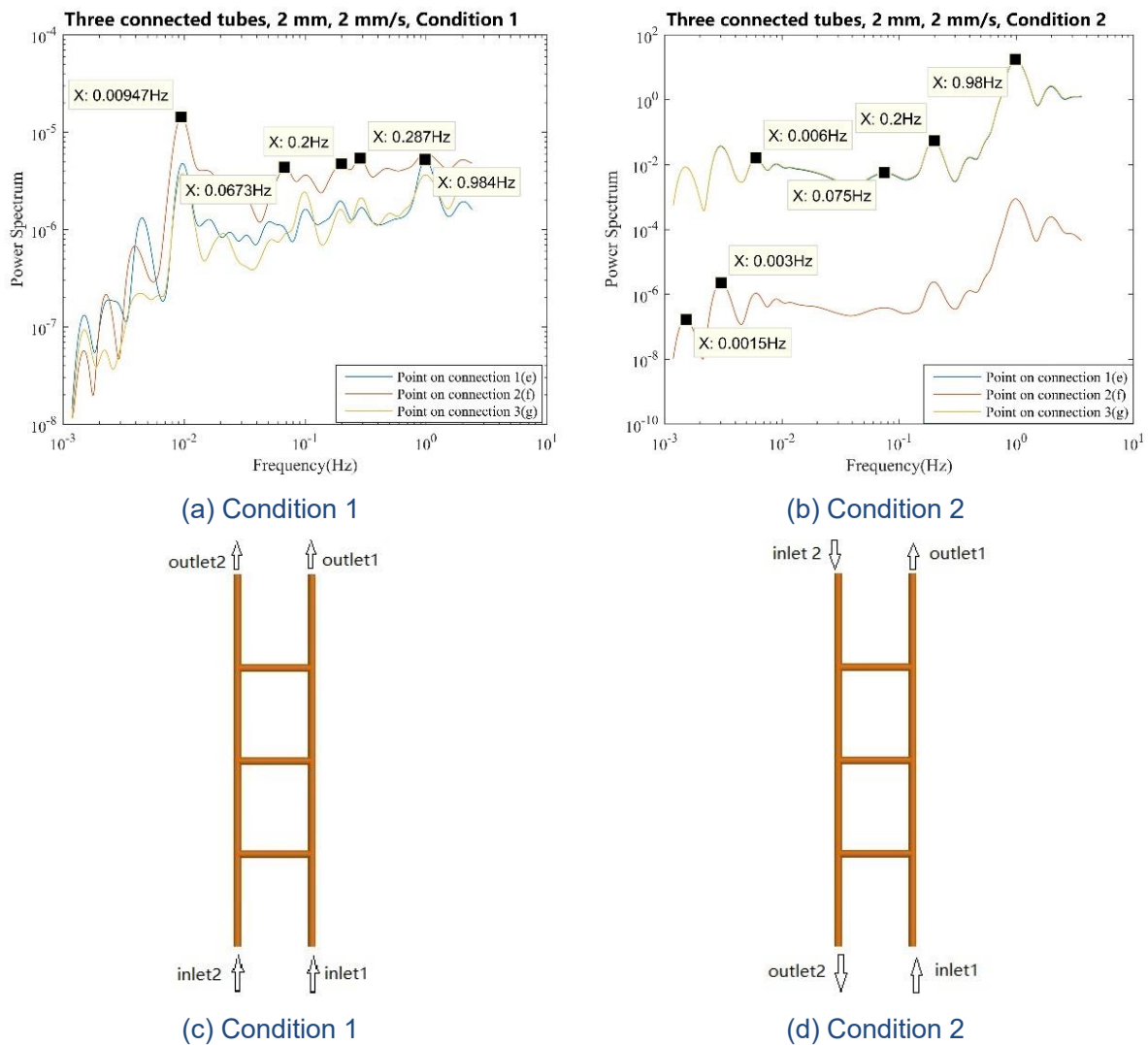


Figure 3-22 Three-connected-tubes model, different open-close states, 2 mm diameter, 2 mm/s maximum inlet velocity, 0.2 Hz input frequency, mean wavelet analysis

### 3.4.2 0.02459 Hz frequency input for different models

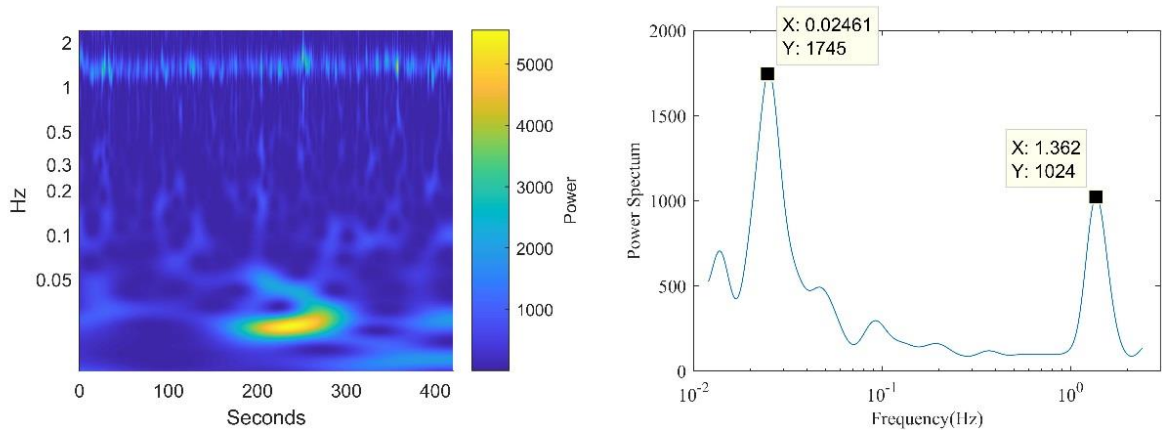


Figure 3-23 Measured data at the radial artery in the wrist, wavelet analysis and mean wavelet analysis

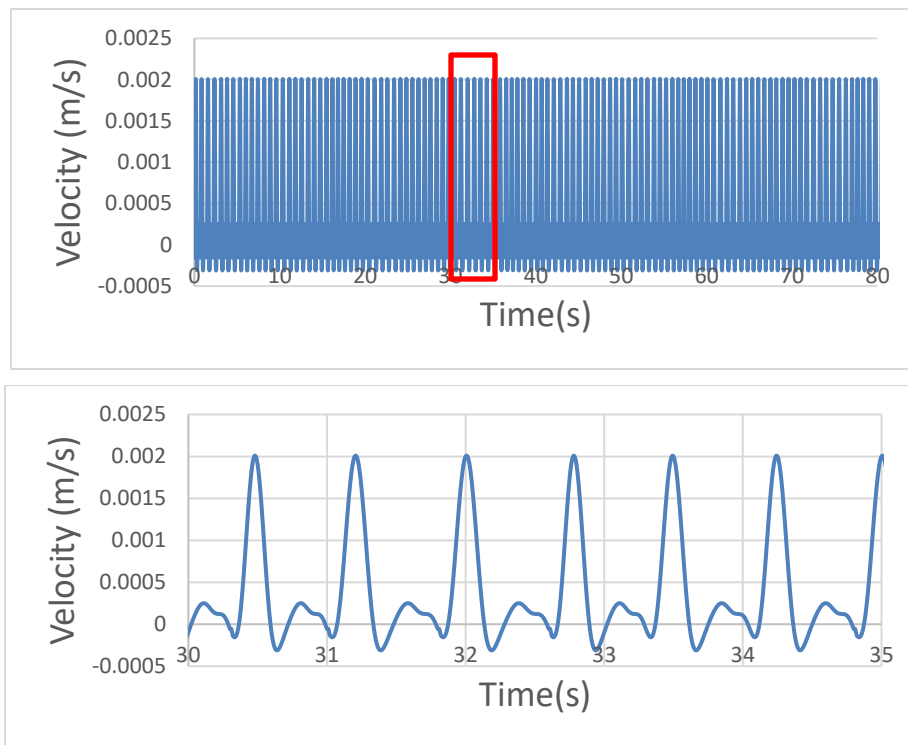


Figure 3-24 Velocity input of 40.5 s period

As shown in Figure 3-23, the measured average heart rate is 1.362 Hz, but it is difficult to determine how the heart period changes. However, we managed to figure an approximating method to build the numerical model of heart period variation. The mean wavelet analysis demonstrates that 0.02461 Hz has a higher PSD than that of heart rate (~1Hz), so from the measured heart period data, we truncate a segment that added up to

40.5 s (0.02459 Hz) to establish an input period for the numerical simulation. The constructed input period of 40.5 s consists of 55 sub-cycles, and the velocity profile is shown in Figure 3-24. The velocity profiles between 30 s and 35 s in the red box are magnified.

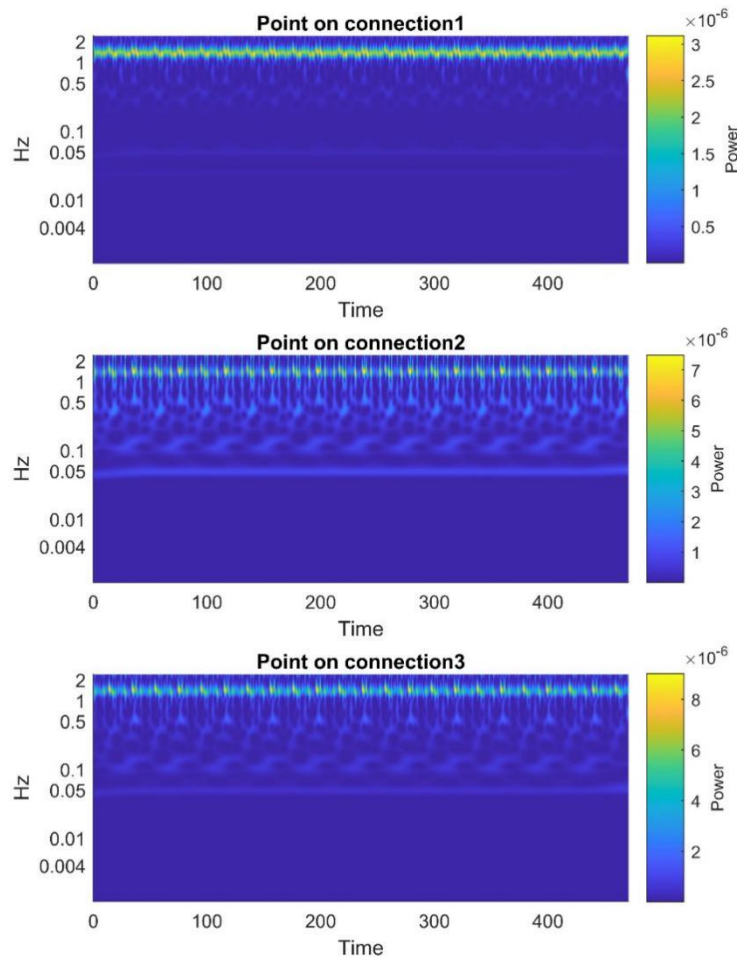


Figure 3-25 Three-connected-tubes model, points on three connections, 0.0245 Hz input frequency, wavelet analysis

In Figure 3-15 and Figure 3-26 where the input frequencies of the three-connected-tubes model are 0.2 Hz and 0.0245 Hz, respectively, the data on the points before and after the connection shows a similar pattern that ~1Hz frequency oscillation plays a dominant role and low-frequency components are not obvious. In the results at the points on the connections (shown in Figure 3-25), there is a broad frequency band from 0.2 Hz to 1 Hz which resembles the real blood flow oscillation shown in Figure 3-16, and a net shape

pattern is recognized. The shape of results at the points on connections 2 and 3 demonstrates a more complicated structure than that at the point on connection 1. Besides the net shape frequency band,  $\sim 0.1$  Hz is also captured at the three monitor points on connections.

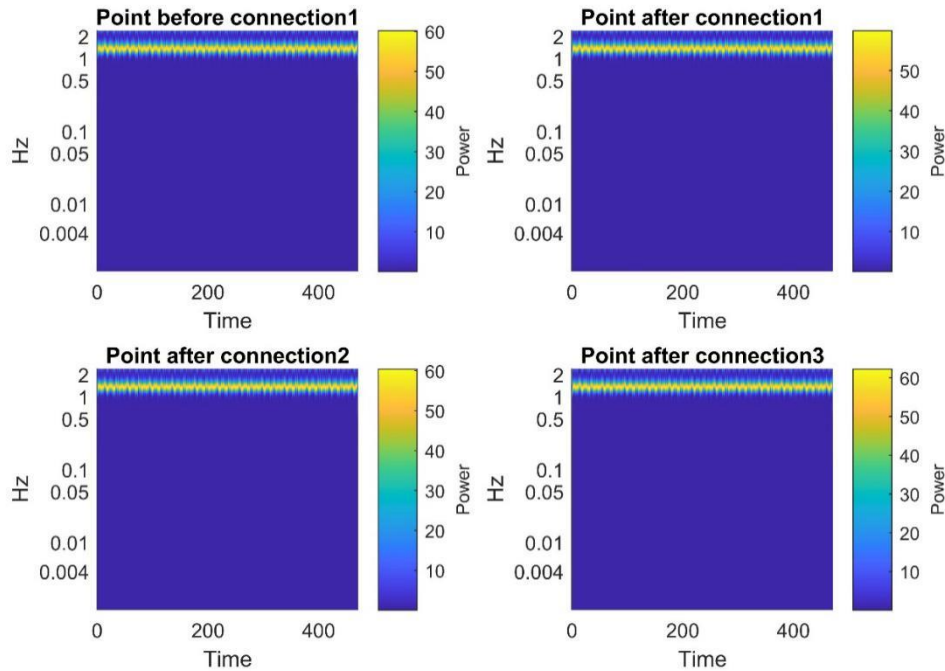


Figure 3-26 Three-connected-tubes model, point before and after three connections, 0.0245 Hz input frequency, wavelet analysis

Figure 3-27 demonstrates the mean wavelet analysis, and the results in the red box are magnified. The input frequency of 0.0245 Hz is observed in three monitors, while 0.0489 Hz, 0.0972 Hz, and 0.147 Hz could be the harmonic frequencies of 0.0245 Hz. Similar to the results of 0.2 Hz input frequency, the point on connection 2 has a higher power spectrum at 0.0489 Hz, 0.0972 Hz, and 0.147 Hz than that of the points on connection 1 and 3, which is also consistent with the two facts mentioned in Section 3.4.1.

I speculate that vasomotion-related frequencies ( $\sim 0.1$  Hz) are the harmonics of the input heart rate variation frequency, indicating the likely relationship between the low-frequency blood flow oscillations and the harmonics of the heart rate variation frequency.

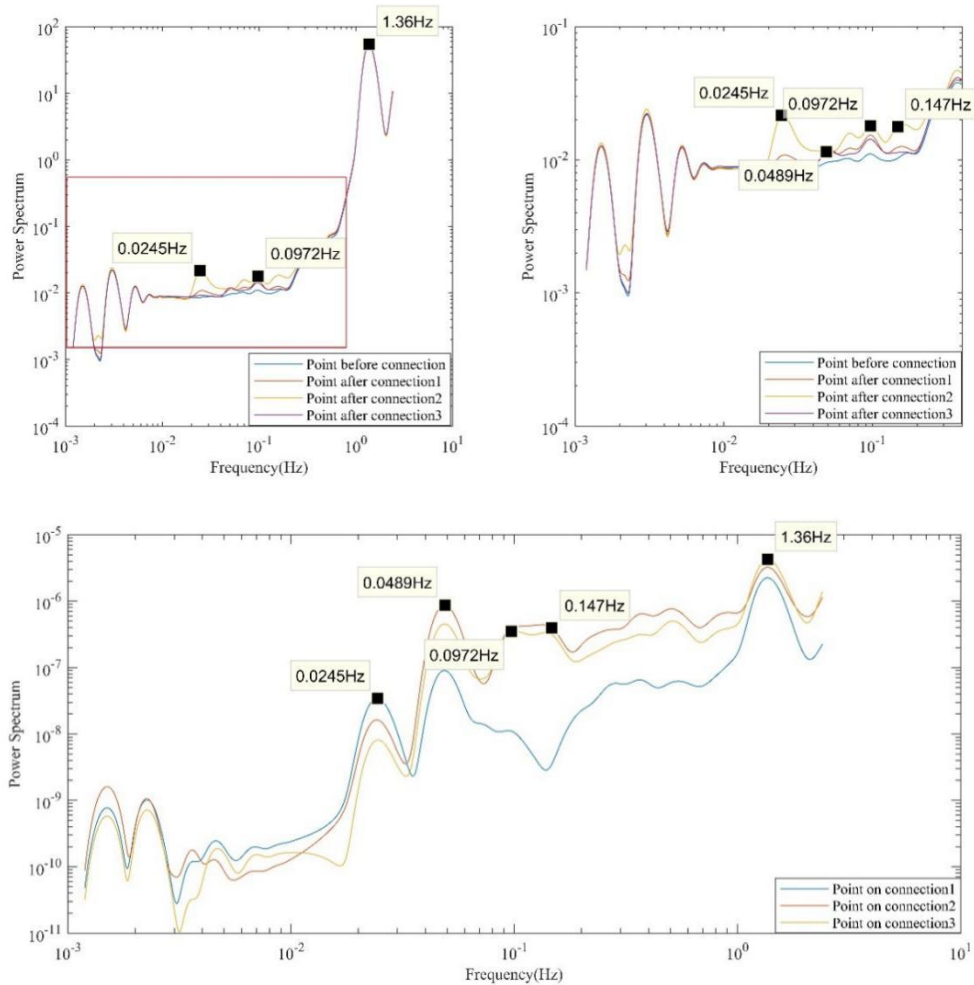


Figure 3-27 Three-connected-tubes model, 0.0245 Hz input frequency, mean wavelet analysis

### 3.5 Frequency of the system

Every vibration mode has its own characteristic frequency. The characteristic frequency of the arterial system depends on its geometry, mass density, and tethering<sup>176</sup>. For the vasculature model in Figure 3-1 (b), the root mean square (RMS) of oscillating pressure at different inlet frequencies is tabulated in Table 3-5. The RMS of oscillating pressure increases dramatically from 1 Hz to 1.87 Hz and then decreases gradually, indicating the frequency of the vasculature system is 1.87 Hz.

Using the same method, the natural frequencies of systems in Figure 3-1 (c) with different numbers of connected tubes are investigated. As shown in Figure 3-28, the frequency is

2.29 Hz for the single-connected tube system, 0.67 Hz for 16 connected tubes, and 0.37 Hz for 32 connected tubes, indicating that the frequency of the system decreases with the complexity of the microvasculature. Real human microvasculature is much more complicated than the vasculature in Figure 3-1 (c), and therefore we speculate that the frequency of the human microvasculature system is lower than 0.37 Hz. We wonder if the low-frequency vasomotion is due to the interaction between the cardiac rhythm and the frequency of the vasculature system.

Table 3-5 RMS of oscillating pressure for different frequencies

Frequency (Hz)	0.072	1	1.87	10	25	50
RMS(Pa)	0.0107	8.4077	68.0392	29.9428	10.1772	6.9592

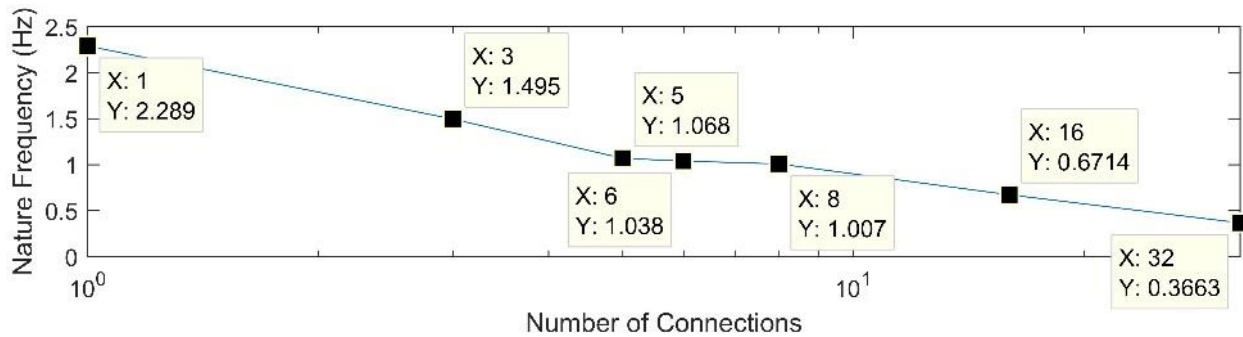


Figure 3-28 Frequencies of the connected-tubes model system

## Chapter 4 The origin of vasomotion

### 4.1 Experiment procedure

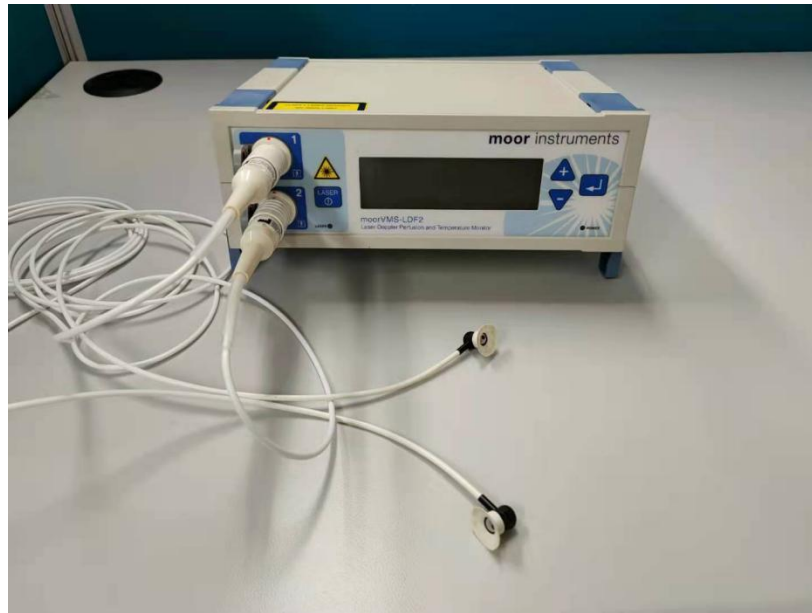


Figure 4-1 Laser Doppler flowmetry

We measured the oscillating radial artery blood flow at the wrist for four health subjects, two females and two males aged between 20 to 30 years. The baseline characteristics of the four subjects are presented in Table 4-1. They were asked to (i) avoid caffeine intake for two hours before the test; (ii) remain seated and still during the measurement; and (iii) avoid drugs for three days before the experiment.

Table 4-1 Anthropometric parameters for four subjects

	Gender	Hight (cm)	Weight (Kg)	Systolic Pressure(mmHg)	Diastolic Pressure(mmHg)	Pulse Rate (BPM)
Subject 1	Female	150	50	67	108	73
Subject 2	Female	164	52	70	116	87
Subject 3	Male	168	55	73	115	78
Subject 4	Male	178	85	79	125	76

During LDF measurement, two laser probes were connected to the Laser Doppler perfusion and the temperature monitor. Each probe contains one transmitting optical fiber and one receiving optical fiber. When attached to a specific skin location, probes will

receive the Doppler-shifted laser light reflecting the activities of red blood cells which are traveling through vessels. The detailed principle and application of LDF are introduced in section 1.1. The sampling frequency or the sampling rate is the number of samples obtained in one second. A 40 Hz sampling rate was used, meaning a 0.025 s time interval. The measurement time was 10 minutes.

The measured time series exhibited a periodical pattern so that the whole measurement time could be divided into beat-to-beat periods. Based on the heartbeat curve, we reconstructed two modified time series period by period, namely the average flux signal and the reconstructed signal. The average flux curve is generated by averaging all data points in each period. The reconstructed signal  $y(t)$  consists of sinusoidal curves and each sinusoidal curve is constructed by a sinusoidal function and a lift. The sinusoidal function's amplitude ( $A$ ) equals to half of the difference between maximum value ( $D_{max}$ ) and minimum value ( $D_{min}$ ) in each period. The lift is the average flux ( $F$ ) in each period. After the reconstruction of the average flux curve and the sinusoidal curve, the irregular fluctuation on the heartbeat curve is eliminated and its influence on low frequencies is minimized. Figure 4-2 indicates reconstructed time series and measured time series in three periods with the sequence axis as the x-axis.

$$y(t) = A\sin(2\pi*t/T) + F$$

$$F = \frac{\sum_{i=1}^n D_i}{n}$$

$$A = \frac{D_{max} - D_{min}}{2}$$

$n$  – Number of measured data in each period

$D_i$  – Measured data in each period

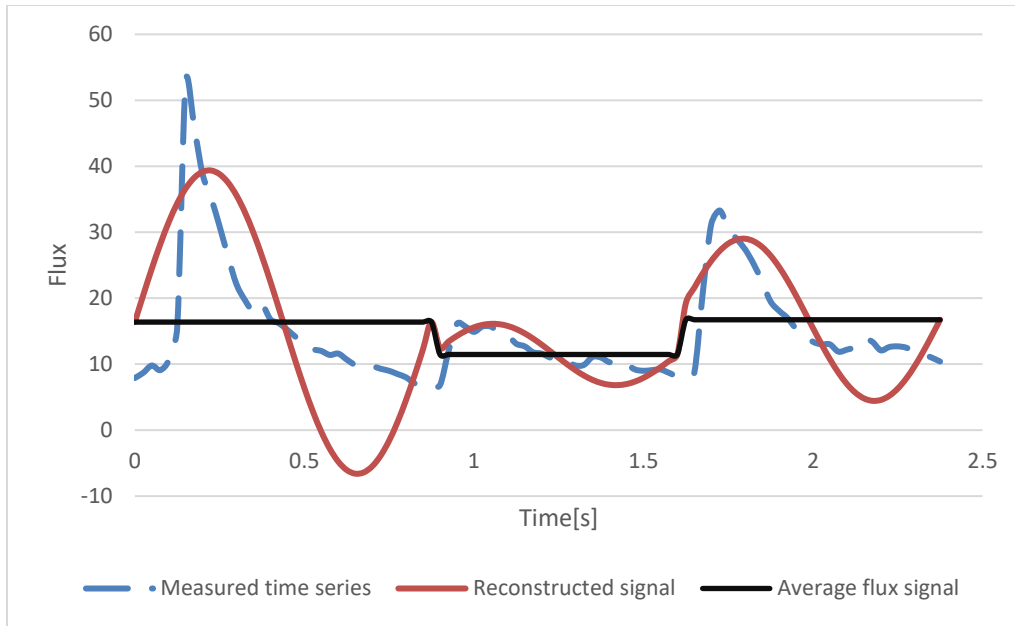
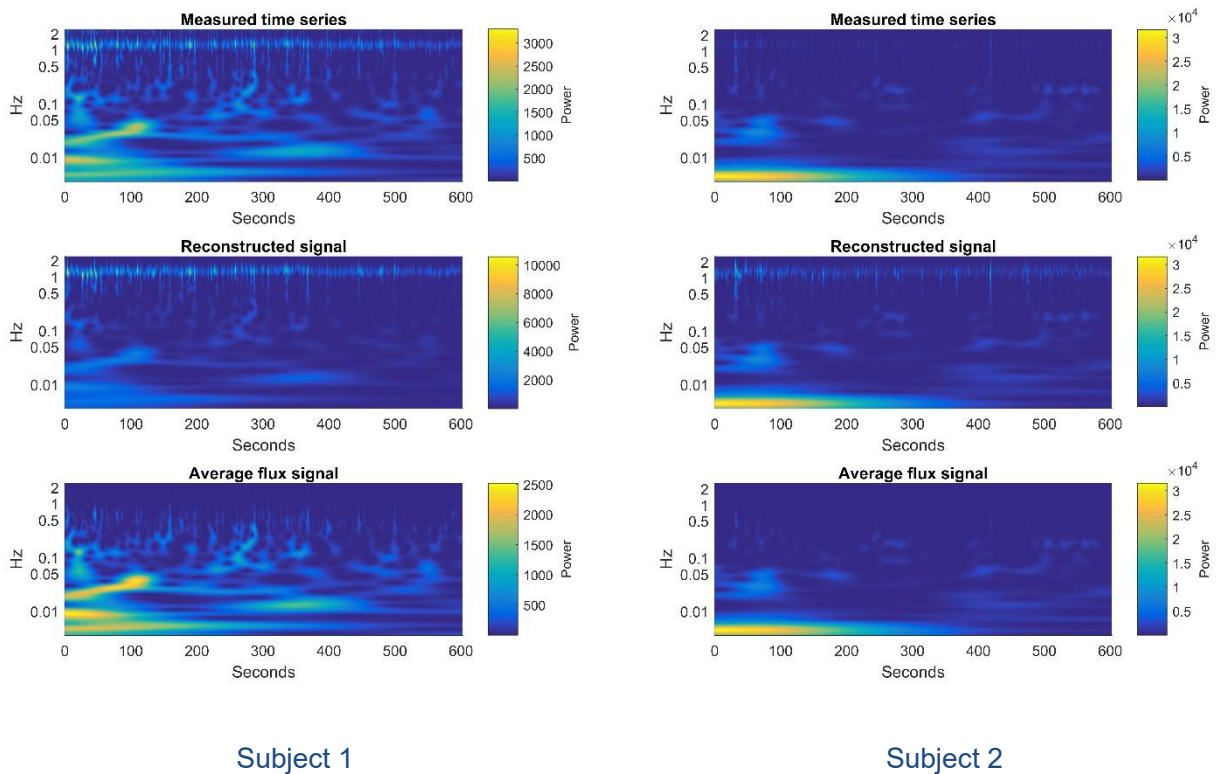


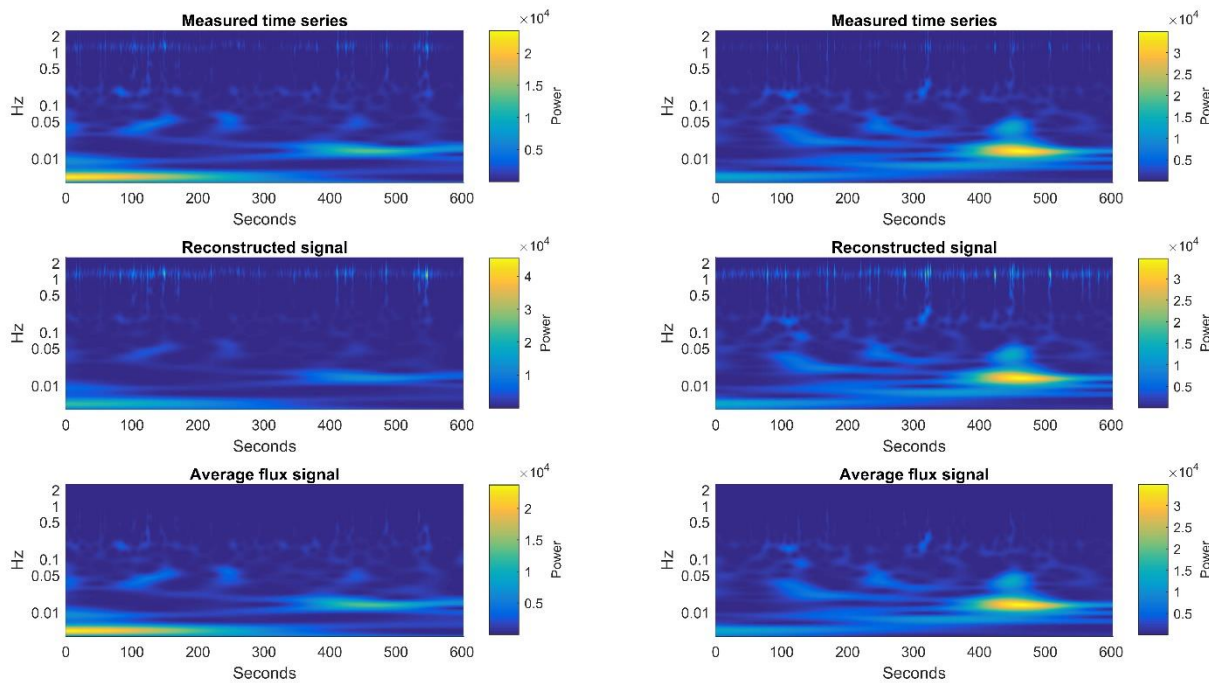
Figure 4-2 Reconstructed data and experimental data in three cycles

## 4.2 Experiment results



Subject 1

Subject 2



Subject 3

Subject 4

Figure 4-3 The wavelet analysis of the measured time series, the reconstructed signal, and the average flux signal

Figure 4-3 shows the wavelet analysis of the measured time series, reconstructed signal, and average flux signal. In general, the frequency distributions of these three cases are similar to each other. The lower frequencies band is almost the same. In the case of the average curve, the frequency is very weak at 1 Hz but quite strong at the lower frequency band. To show the comparison clearly, we took the mean value along the time span, as shown in Figure 4-4.

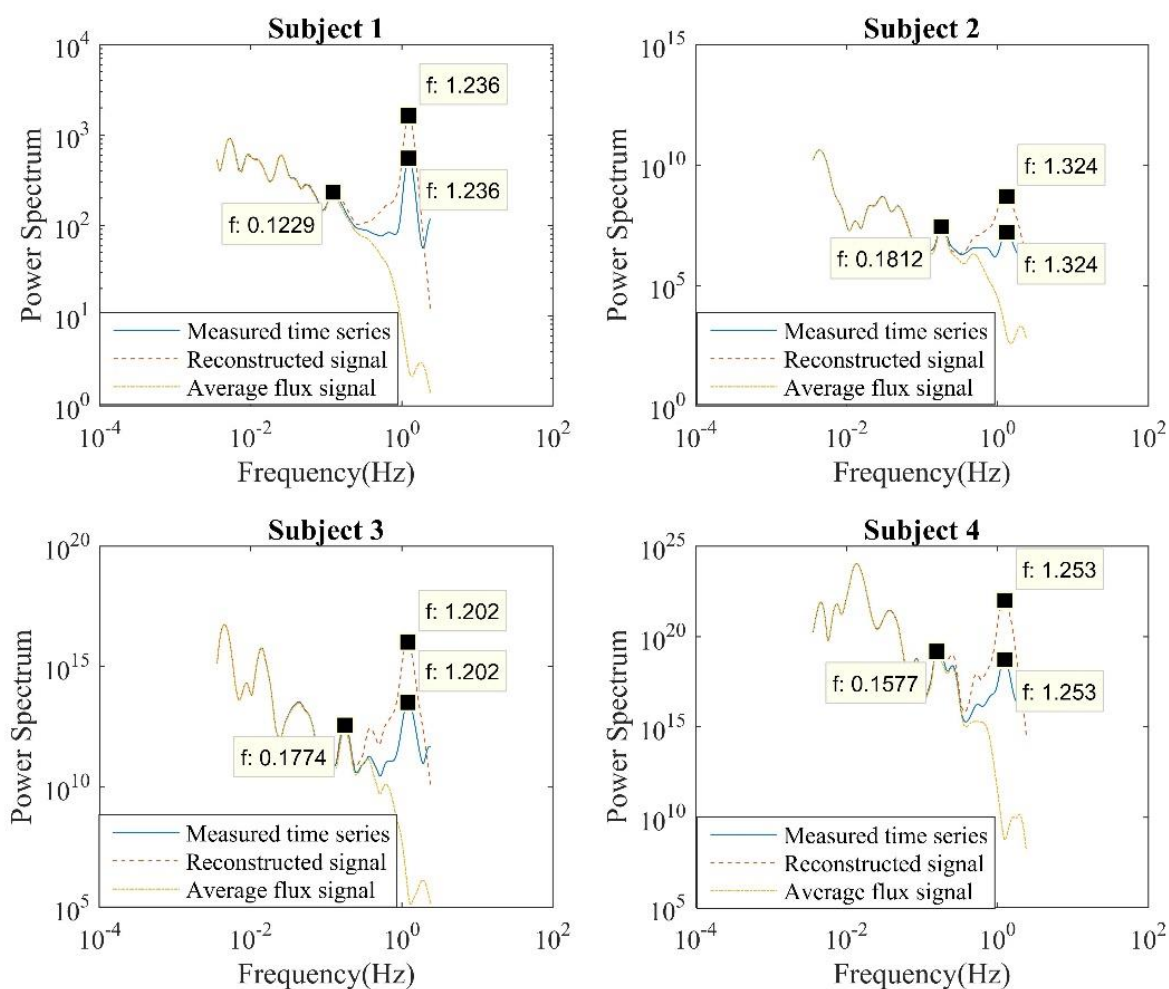


Figure 4-4 The mean wavelet analysis of the measured time series, the reconstructed signal, and the average flux signal

Figure 4-4 demonstrates the mean wavelet analysis of the measured time series, the reconstructed signal, and the average flux signal for the four study subjects. The measured and reconstructed sinusoid time series have the same heart rate peaks and an overlapped lower frequency band. The average flux signal can be extracted from the measured time series of the reconstructed signal. So, the measured time series and the reconstructed signal contain all the information of the averaged flux data and share some oscillation features as the average flux signal. It is obvious in Figure 4-4 that the frequencies below 0.2 Hz are almost identical in the mean wavelet curves of these three signals. The same component contained in these three signals is the average flux. Thus, the shared lower frequency band (0.01~0.2 Hz) in the mean wavelet analysis results of

the reconstructed signal and measured time series comes from the average flux. Because the average flux in each period represents the local average blood flux, it can be speculated that the lower frequency band (0.01~0.2 Hz) is induced by the averaged blood flux in each heart period.

Table 4-2 The coefficients of determination ( $R^2$ ) of mean wavelet analysis data between the reconstructed signal, the average flux signal, and the measured time series

(a) all mean wavelet analysis data

$R^2$	Subject1	Subject2	Subject3	Subject4
Reconstructed signal	0.990513	0.999836	0.967729	0.999832
Average flux signal	0.991526	0.999997	0.999914	0.999974

(b) mean wavelet analysis data of frequency below 0.25Hz

$R^2$	Subject1	Subject2	Subject3	Subject4
Reconstructed signal	0.997176	0.999991	0.999912	0.999917
Average flux signal	0.999524	0.999997	0.999994	0.999973

Linear regression analysis helps to find the relationship between the measured time series and the reconstructed signal with sinusoid curves, as well as the relationship between the measured time series and the average flux signals. The coefficients of determination ( $R^2$ ) interpret the ability of a model to predict or explain an outcome. In Table 4-2, the  $R^2$  of mean wavelet analysis data between reconstructed signals and measured time series, and the  $R^2$  between average flux signals and measured time series are close to one for the four subjects, which indicates that the mean wavelet analysis results of the reconstructed signal and the average flux signal are linear with respect to the measured time series. The average flux signals fit the measured time series better than reconstructed signals on account of larger  $R^2$ . Also, the intercepted mean wavelet analysis data of frequency below 0.25 Hz generates an even larger  $R^2$ . The lower frequency components of the average flux signal are the same as that of the measured time series.

# Chapter 5 Stochastic resonance

## 5.1 Pressure disturbance

### 5.1.1 Procedure



Figure 5-1 Pulse diagnosis and a sphygmomanometer cuff encircling the forearm

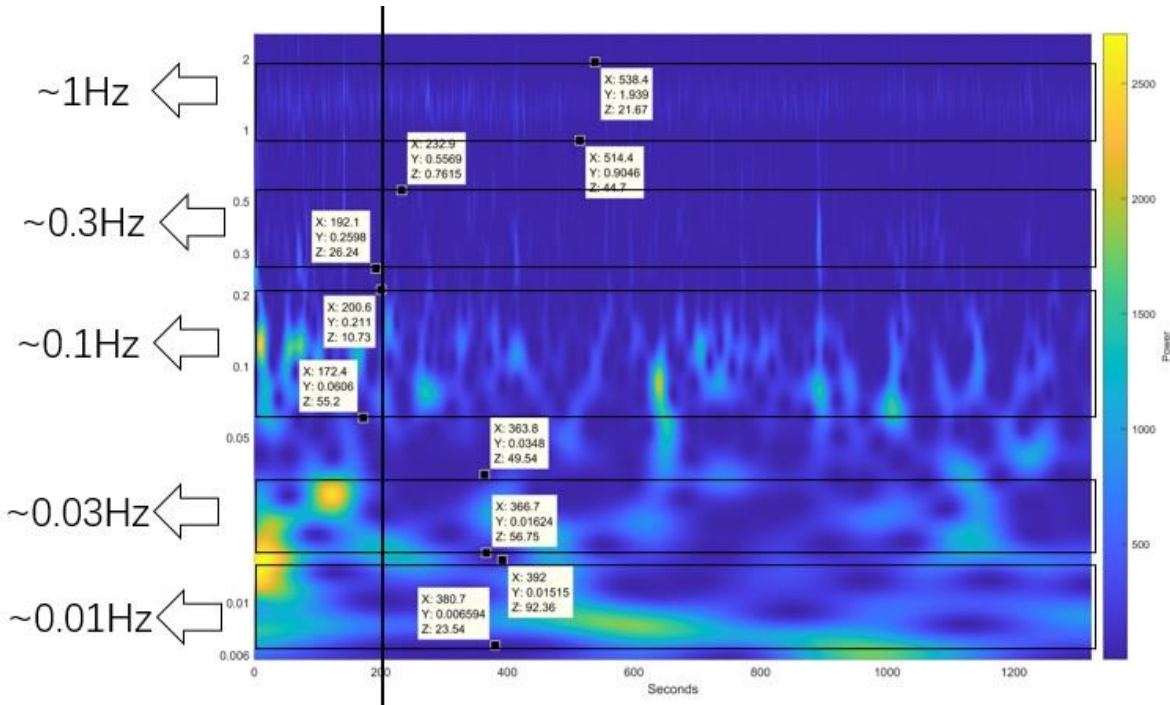


Figure 5-2 Five frequency bands in the wavelet analysis result

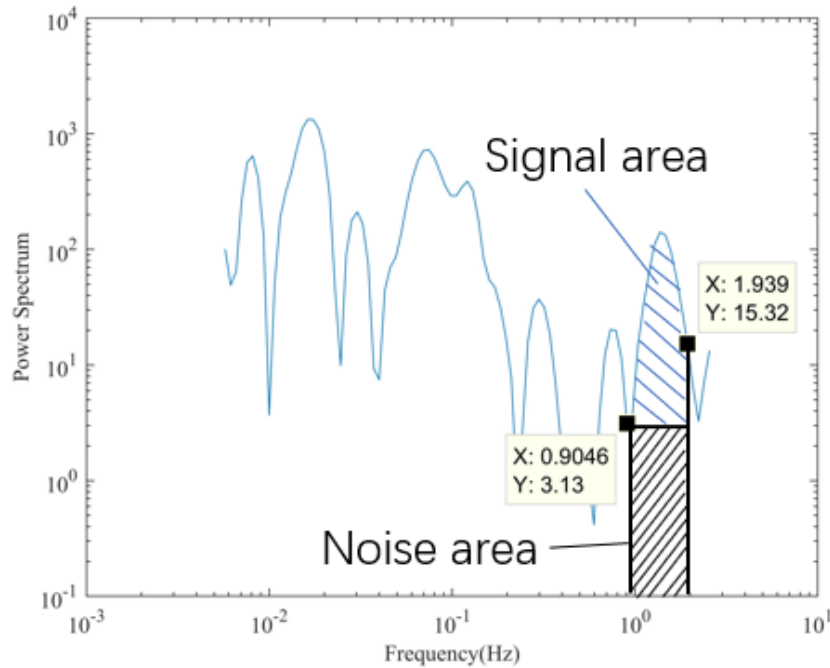


Figure 5-3 Instantaneous power spectrum in wavelet analysis

We measured the oscillating radial artery blood flow at the wrist for four health subjects, two females and two males aged from 20 to 30. The sampling rate is 20 Hz, which is equivalent to a 0.05s time interval. As shown in Figure 5-1, a sphygmomanometer cuff was placed on the forearm, and the cuff pressures were set to 0 mmHg, 5 mmHg, 10 mmHg, 15 mmHg, and 20 mmHg during different periods. The measurement time continued 50 minutes, consisting of five periods of 10 minutes each., And for each subject, there are four groups of experiments. After wavelet analysis of LDF signals was conducted, five frequency bands were observed, ~1 Hz, ~0.3 Hz, ~0.1 Hz, ~0.03 Hz, and ~0.01 Hz, which correspond to cardiac, respiratory, myogenic, neurogenic, and endothelial activities, respectively<sup>175</sup>. For each LDF signals' wavelet analysis results, we specified each frequency band with an upper-frequency limit and a lower-frequency limit which is shown in Figure 5-2. Through wavelet analysis, we can obtain the instantaneous power spectrum demonstrated in Figure 5-3. The instantaneous SNR can be calculated by the method stated in section 2.3. The total integrated signal power  $S_p$  is the signal area colored in blue shade and the total integrated noise power  $N_p$  is the noise area colored in black shade in Figure 5-3.

### 5.1.2 Results

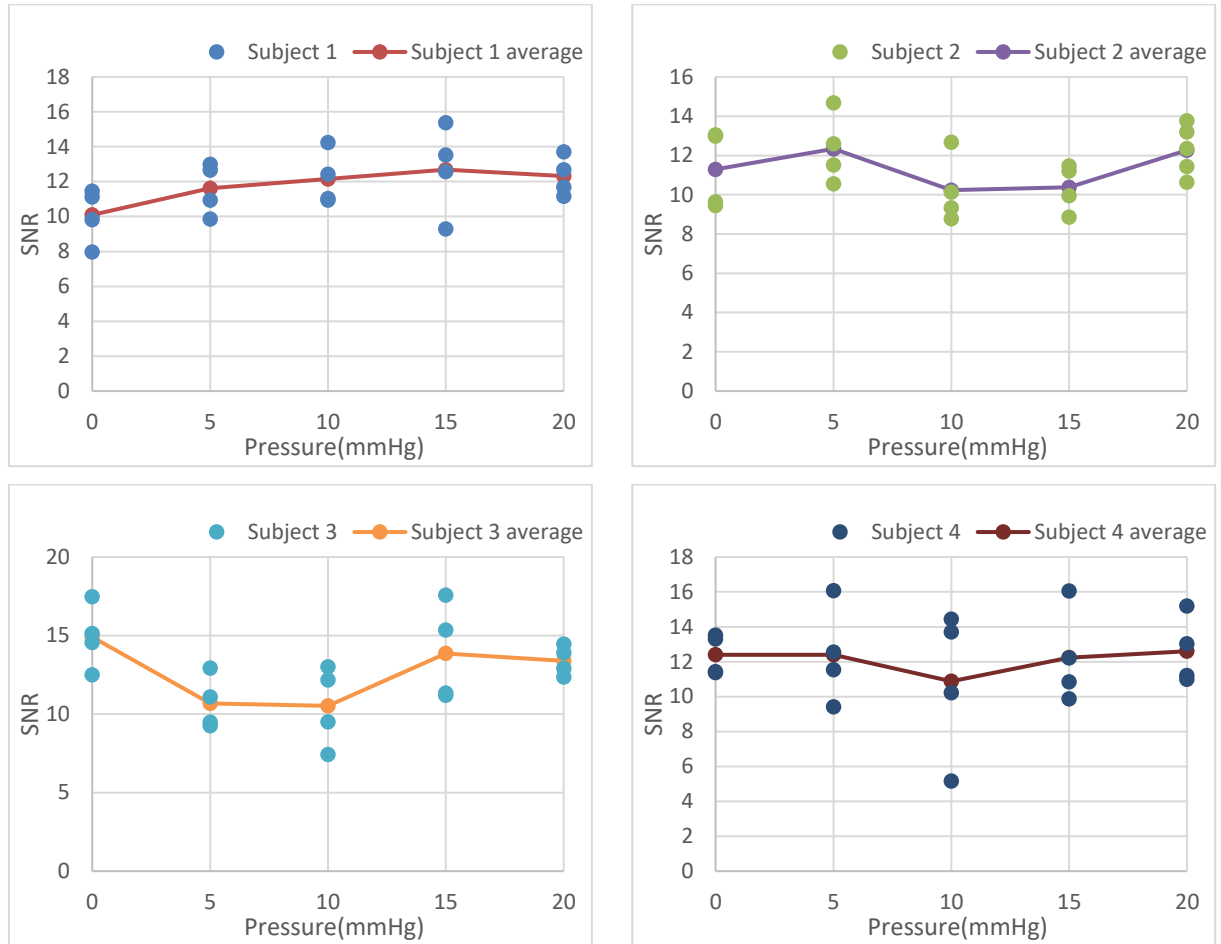


Figure 5-4 The SNR for frequency band around 1 Hz of four subjects with different pressures

We calculated the average SNR from the instantaneous SNR of five frequency bands. Figure 5-4 shows the average SNR for the frequency band around 1 Hz which includes four experiments data for each subject. For subject 1, the SNR increases with the cuff pressure and reaches the maximum at 15 mmHg, and then slightly decreases at 20 mmHg. For subject 2, the SNR increases at 5 mmHg, then decreases at 10 mmHg, and then continues to increase at 15 mmHg and 20 mmHg, with the maximum average SNR exhibited at 20 mmHg. The average SNR curve of subject 3 reveals a trend of gradually decreasing before 10 mmHg and fluctuating at 15 mmHg and 20 mmHg, however, the maximum average SNR is observed when no pressure is added. A concave shape is found in the average SNR curve of subject 4. The minimum average SNR shows up at 10 mmHg, and the average SNR at 20 mmHg is slightly larger compared to the other four

pressure conditions. Generally, the SNR of frequency band around 1 Hz related to the cardiac activity first reduces with the increase of pressure and then rises, reaching a maximum at 15 mmHg or 20 mmHg.

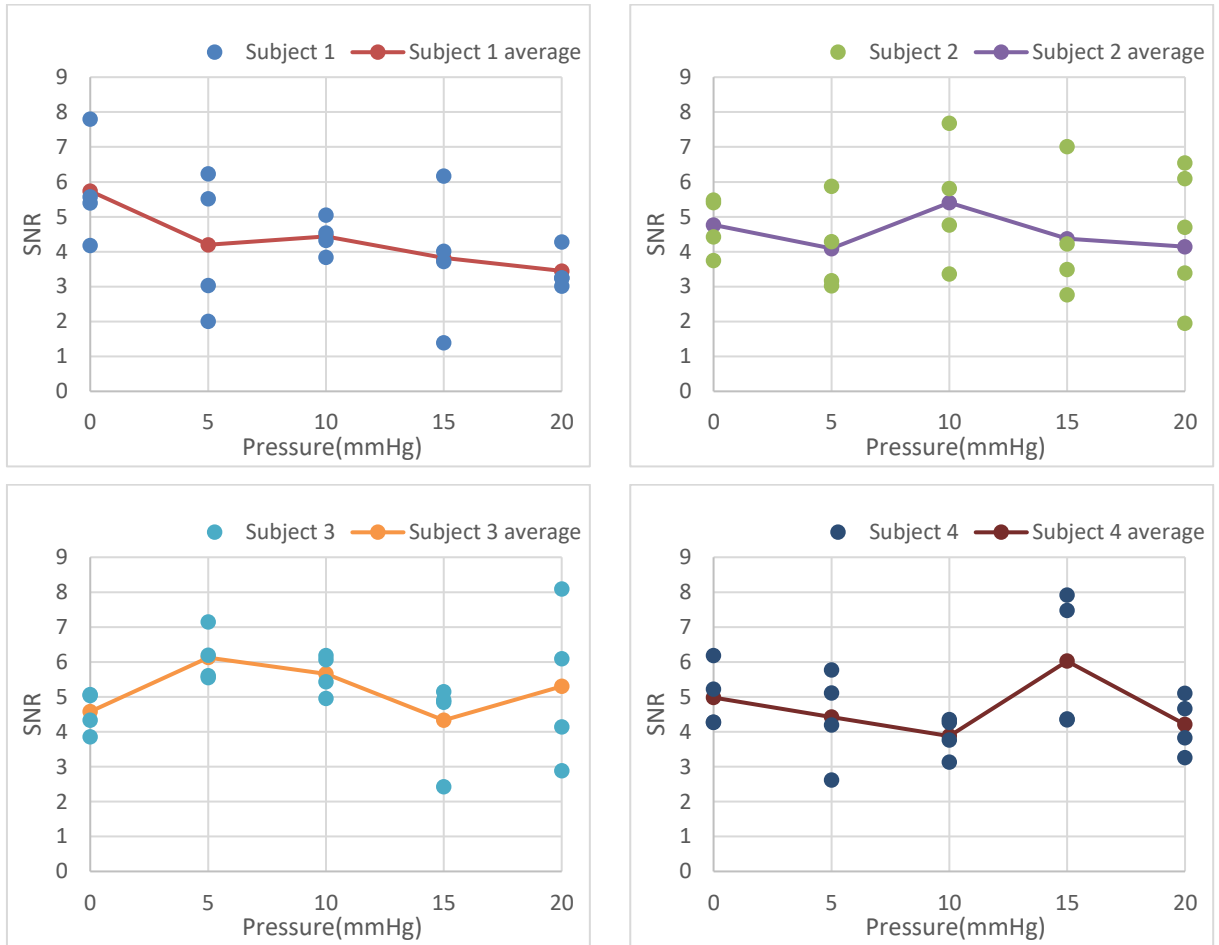


Figure 5-5 The SNR for frequency band around 0.3 Hz of four subjects with different pressures  
 Figure 5-5 shows the average SNR for the frequency band around 0.3 Hz associated with respiration activities, where subject 1, 2, and 4 shows a similar trend that the average SNR curve decreases first, and then oscillates as pressure increases. However, the maximum value of average SNR is achieved for subjects 1, 2, and 4 at the cuff pressure of 0 mmHg, 10 mmHg, and 15 mmHg, respectively. For subject 3, the average SNR first increases with increasing pressure and reaches its maximum at 5 mmHg, followed by a decrease until a pressure of 15 mmHg, and ended by an increase until 20 mmHg.

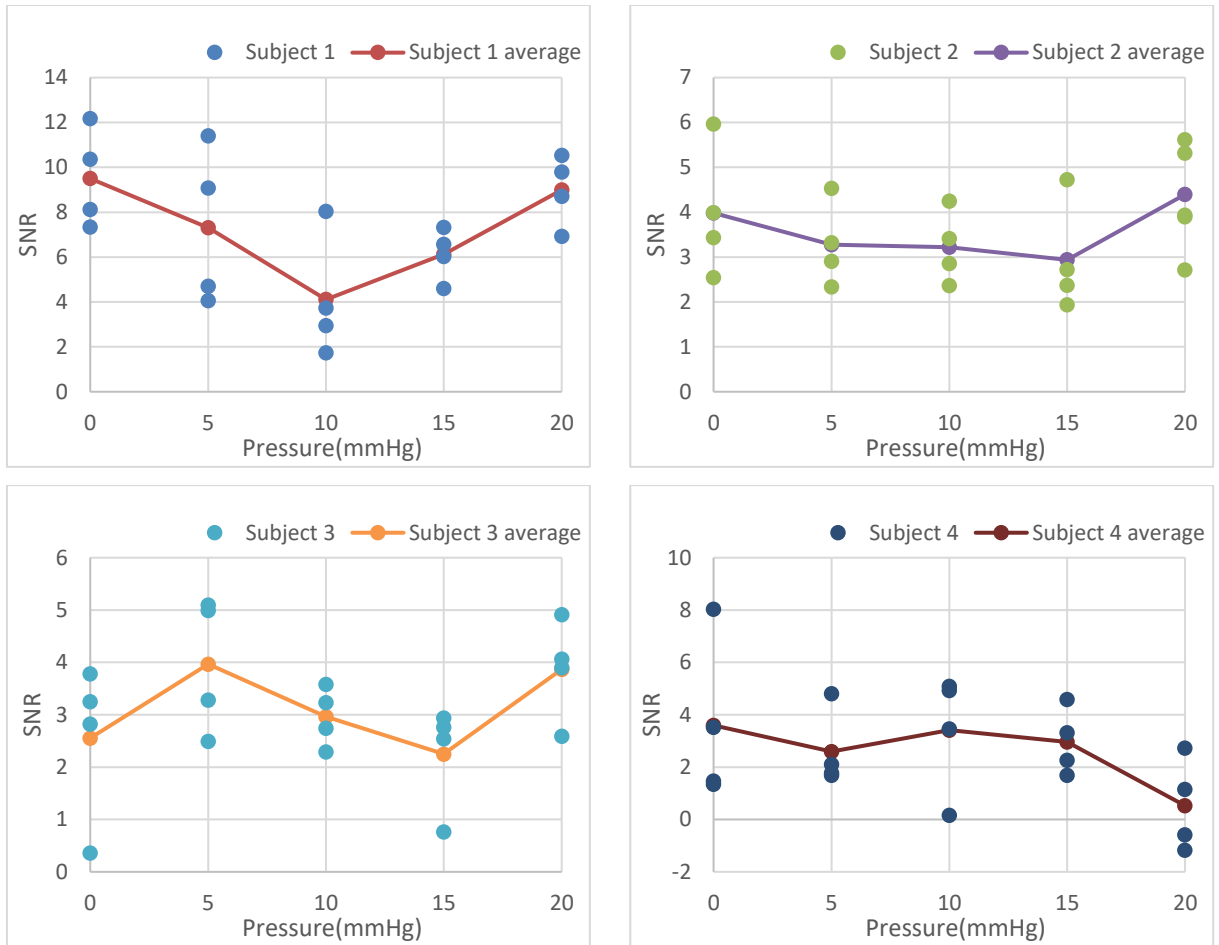


Figure 5-6 The SNR for frequency band around 0.1 Hz of four subjects with different pressures

As shown in Figure 5-6, the average SNR curves present a concave shape for both subjects 1 and 2 in the frequency band around 0.1 Hz, with the minimum average SNR at the cuff pressure of 10 mmHg and 15 mmHg. The average SNR curves of subjects 3 and 4 for frequency around 0.1 Hz show a similar trend to that for frequency around 0.3 Hz. The average SNRs of four subjects reach their maximum values at 0 mmHg, 20 mmHg, 5 mmHg, and 0 mmHg, respectively.

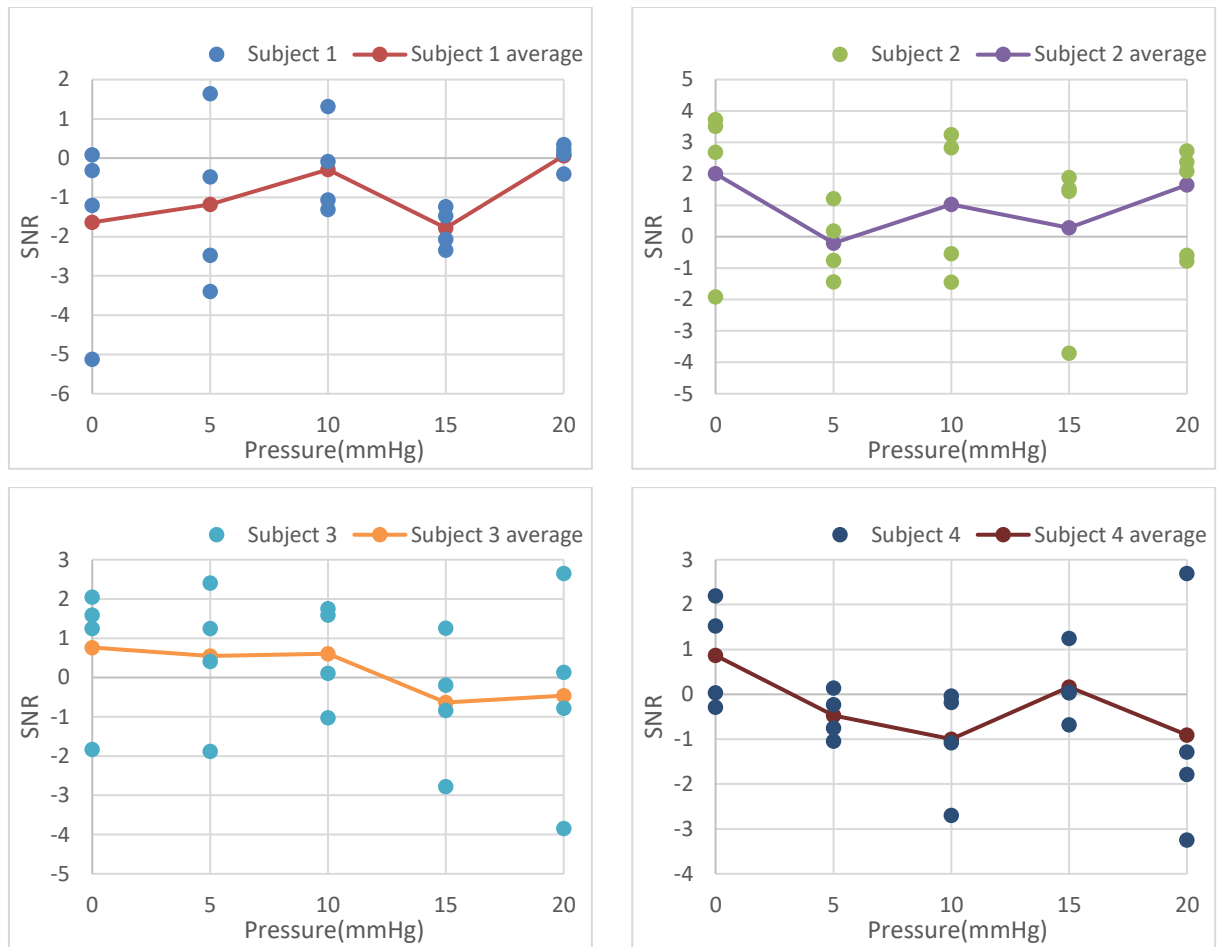


Figure 5-7 The SNR for frequency band around 0.03 Hz of four subjects with different pressures. From Figure 5-4 to Figure 5-8, the average SNRs for frequency bands around 0.03 Hz and 0.01 Hz are more dispersed than those for frequency bands around 1 Hz, 0.3 Hz, and 0.1 Hz. The average SNR curve cannot fully represent the trend of SNR results for the four subjects. However, Figure 5-7 and Figure 5-8 indicate that the SNR will change with the cuff pressure. According to a historical prospective study made by Bedford<sup>177</sup>, ancient Chinese physicians used their index fingers to apply light, moderate, and firm pressure to elicit the superficial and deep pulses. We can infer that the ancient Chinese physicians diagnosed by applying pressures to the wrist to sense the SNR changes in different frequency bands in the pulse signals related to cardiac, respiratory, myogenic, neurogenic, and endothelial activities.

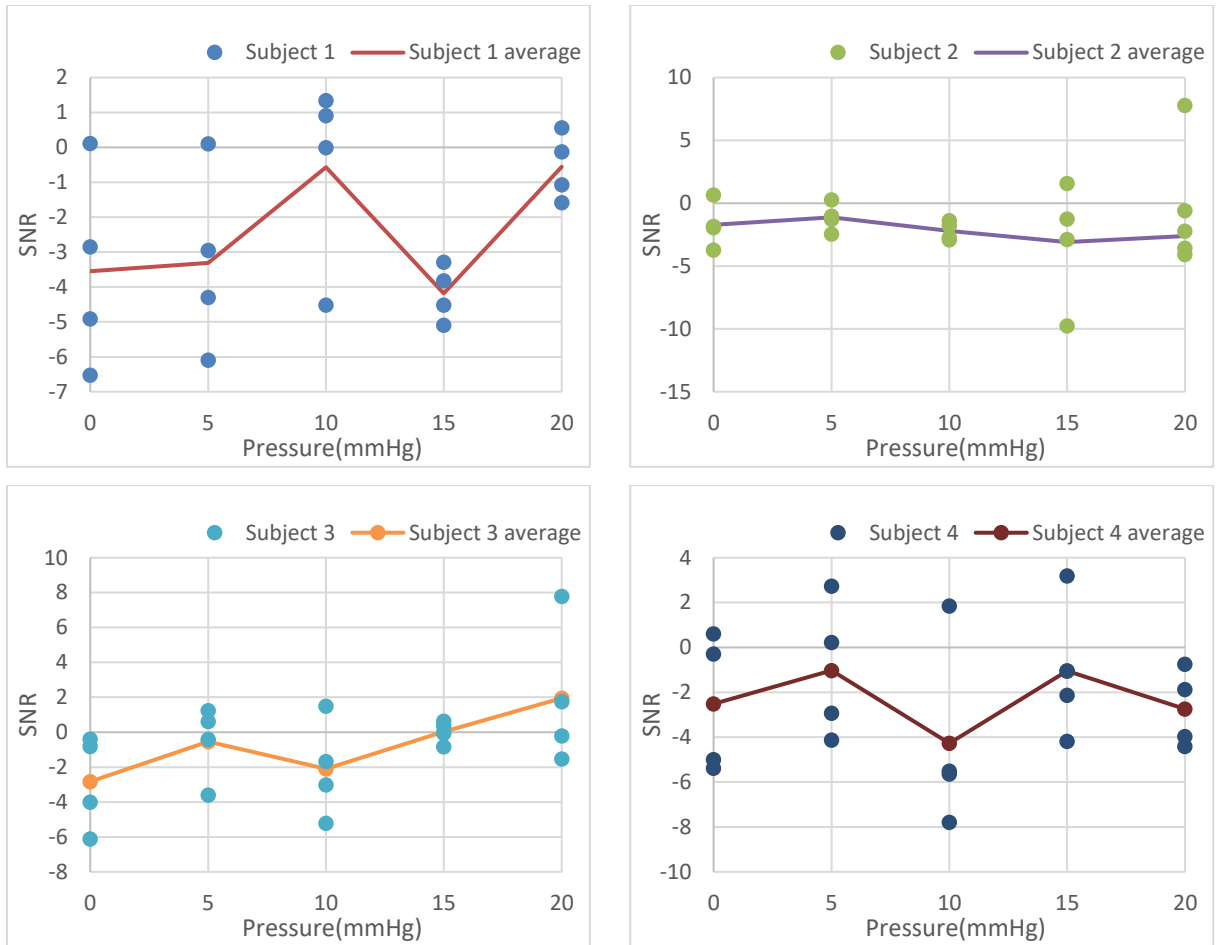


Figure 5-8 The SNR for frequency band around 0.01 Hz of four subjects with different pressures

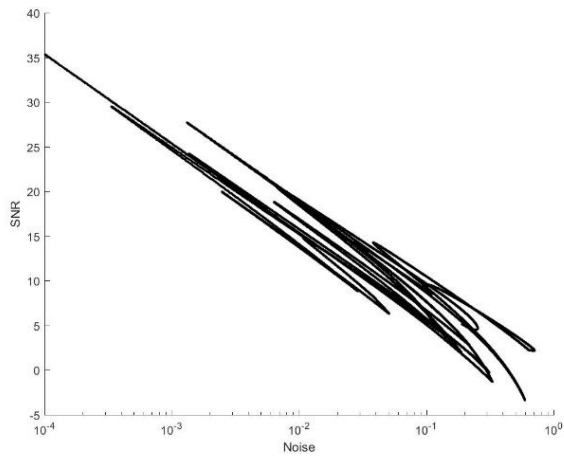
Table 5-1 demonstrates the deviation coefficients calculated with the standard deviation divided by the absolute mean value of each group. The average deviation coefficient of the frequency band around 1Hz is 0.145, which is the smallest among the five frequency bands, and the lower frequency band the larger the deviation coefficient.

Figure 5-9 shows the instantaneous SNR analysis results of one experimental data group for subject 1 including five frequency bands, with x-coordinate being the instantaneous noise and y-coordinate being the instantaneous SNR. The phenomenon of SR is not obvious in the five frequency bands due to the lack of points that have both low SNR and low noise intensity. This might be caused by the error from setting frequency bands manually and using the same frequency bands all the time. Even so, interesting phenomena are found. The points in the frequency band around 1 Hz are concentrated on certain paths, while the paths become scattered for the points in the frequency band around 0.3 Hz. The paths appear more scattered for the points in the frequency band

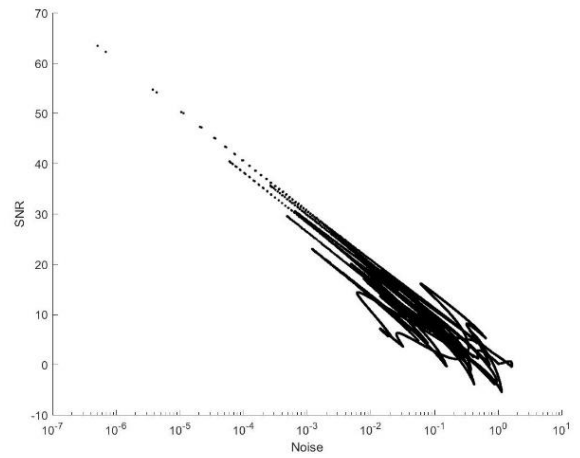
around 0.1 Hz and 0.3 Hz. The points in the frequency band around 0.01 Hz are dispersed and the paths are no longer evident.

Table 5-1 Absolute standard deviation coefficients of SNR

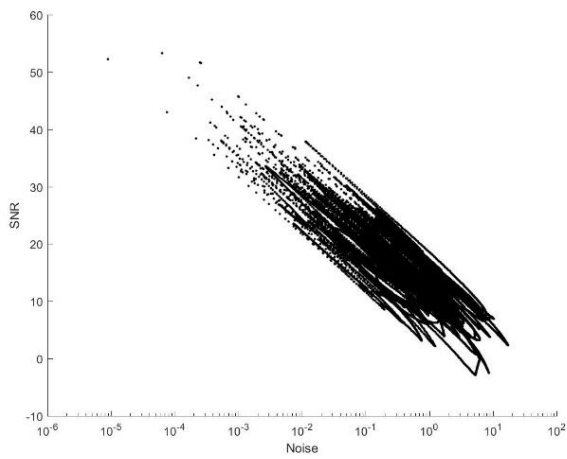
No.	Pressure	1Hz	0.3Hz	0.1Hz	0.03Hz	0.01Hz
<b>Subject 1</b>	20mmHg	0.079241	0.141675	0.15096	4.579919	1.493483
	15mmHg	0.173929	0.442566	0.163184	0.250906	0.163224
	10mmHg	0.109898	0.097929	0.577524	3.579548	4.079848
	5mmHg	0.110029	0.413008	0.418041	1.642994	0.683826
	0mmHg	0.136101	0.227681	0.199869	1.261409	0.699661
<b>Subject 2</b>	20mmHg	0.103657	0.408552	0.263354	0.797862	0.517111
	15mmHg	0.10032	0.36766	0.363064	8.222486	1.35193
	10mmHg	0.145332	0.290975	0.21673	2.003763	0.28659
	5mmHg	0.124128	0.27852	0.246491	4.87496	0.863482
	0mmHg	0.153695	0.150587	0.314946	1.145253	0.908209
<b>Subject 3</b>	20mmHg	0.061375	0.372958	0.214771	5.055524	1.830897
	15mmHg	0.195596	0.255545	0.386683	2.280351	21.30558
	10mmHg	0.210204	0.087709	0.164427	1.873052	1.157683
	5mmHg	0.137776	0.104867	0.28078	2.872052	3.466608
	0mmHg	0.118445	0.11093	0.513022	1.995944	0.833824
<b>Subject 4</b>	20mmHg	0.134165	0.169332	2.888569	2.431853	0.54505
	15mmHg	0.191567	0.278366	0.372262	4.219339	2.586067
	10mmHg	0.337039	0.125165	0.579882	1.062785	0.854282
	5mmHg	0.19387	0.267297	0.494407	0.973291	2.617802
	0mmHg	0.081221	0.158638	0.751562	1.18659	1.070869
<b>Average</b>		0.144879	0.237498	0.478026	2.615494	2.365801



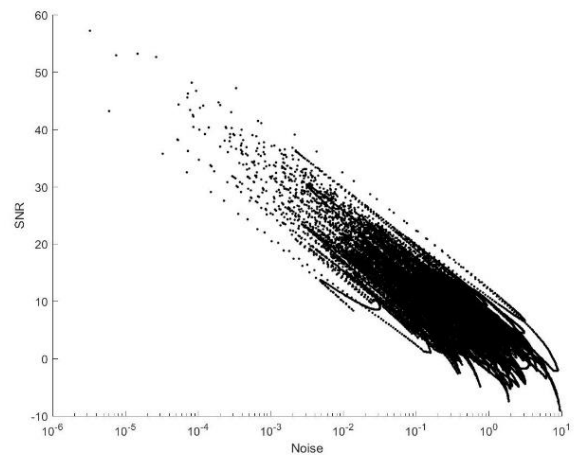
(a) 1 Hz



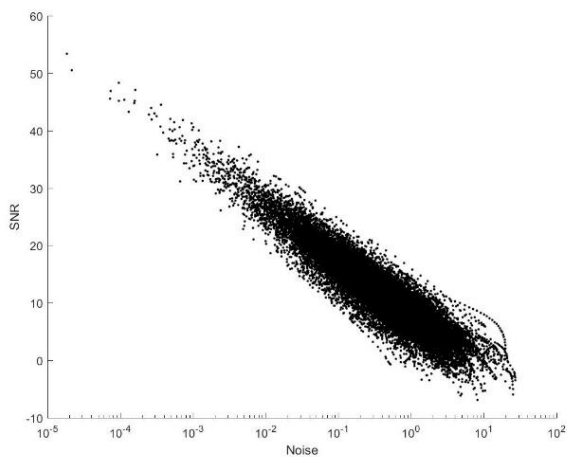
(b) 0.3 Hz



(c) 0.1 Hz



(d) 0.03 Hz



(e) 0.01 Hz

Figure 5-9 SNR vs Noise for five frequency bands of subject 1 without pressure

## 5.2 Noise disturbance

### 5.2.1 Procedure



Figure 5-10 A speaker placed on the forearm

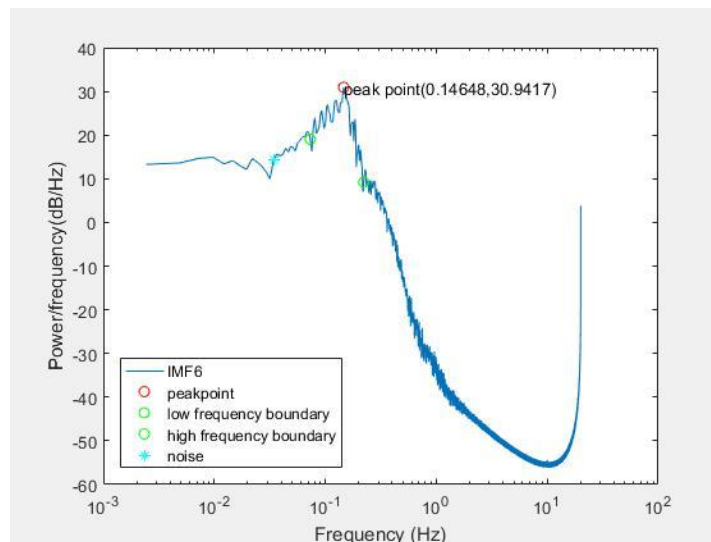


Figure 5-11 An IMF component after HHT

We measured the oscillating radial artery blood flow at the wrist for a 28-year-old health subject. The sampling rate was 20 Hz which indicates that the time interval was 0.05 s. As demonstrated in Figure 5-10, a speaker was placed on the forearm, and white noise and pink noise downloaded from YouTube were added to the pulse signal. All the subjects adopted a seated position during the measurement. The measurement time lasted 1 hour and 40 minutes, and there are five periods of 20 minutes each: without adding noise,

adding white noise, after adding white noise, adding pink noise, and after adding pink noise.

HHT analysis of LDF signals was conducted. The signals were decomposed into several IMFs, one of which is shown in Figure 5-11. Wavelet analysis was then applied to these IMFs, and a frequency band with an upper-frequency limit and a lower-frequency limit was set for each IMFs, which is indicated in Figure 5-12. According to section 5.1.1, through wavelet analysis, we could obtain the wavelet instantaneous power spectrum for IMFs after HHT. As shown in Figure 5-13, because the right half spectrum of IMFs might be a declining slope, it is difficult to determine the signal power and noise power of the spectrum in the right half. Therefore, the SNR was calculated by the left half of the spectrum curve. In the selected frequency band, all extrema were identified, and the maxima and the minima power point were found in these extrema. Figure 5-13 shows the integrated signal power  $S_p$  and the integrated noise power  $N_p$  in the enclosed area of the spectrum curve, under blues shades and black shades, respectively, both starting from the minima power point and ending at the maxima power point.

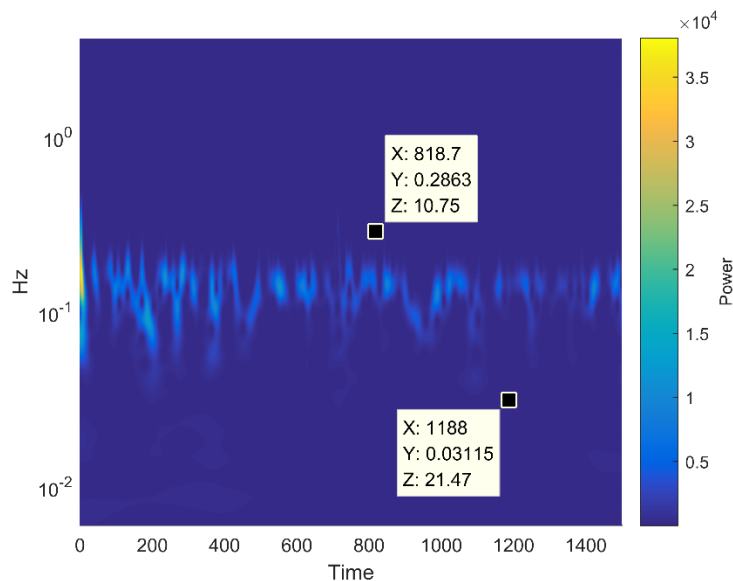


Figure 5-12 Wavelet analysis for an IMF

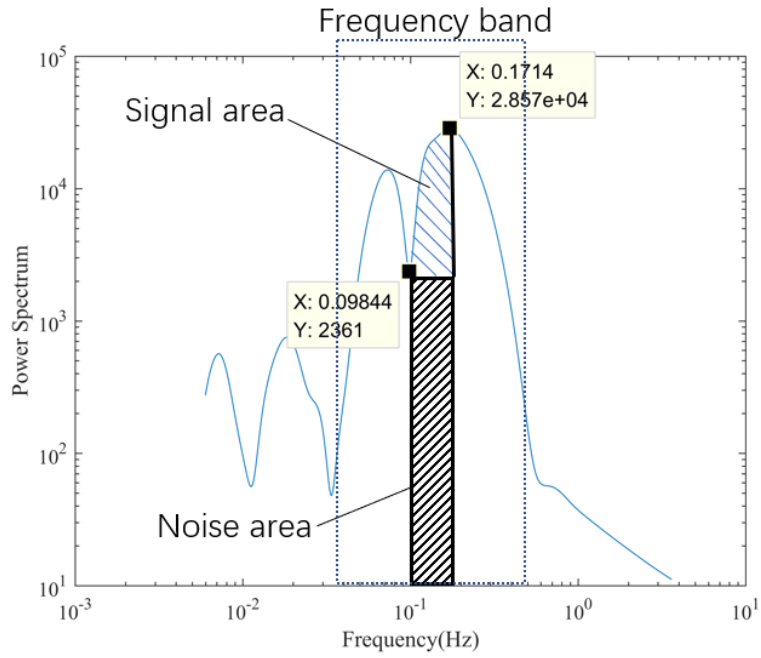
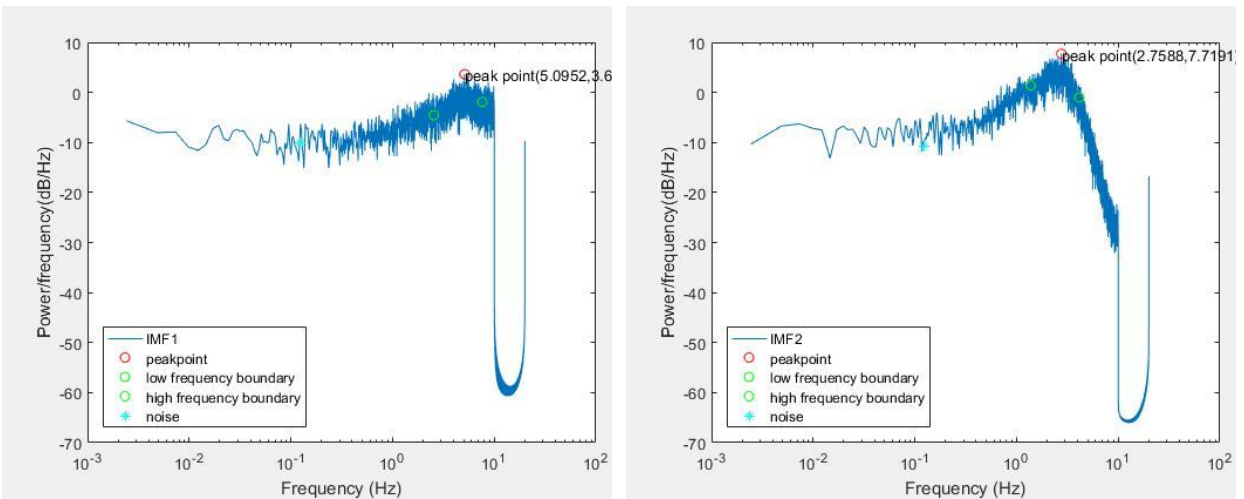
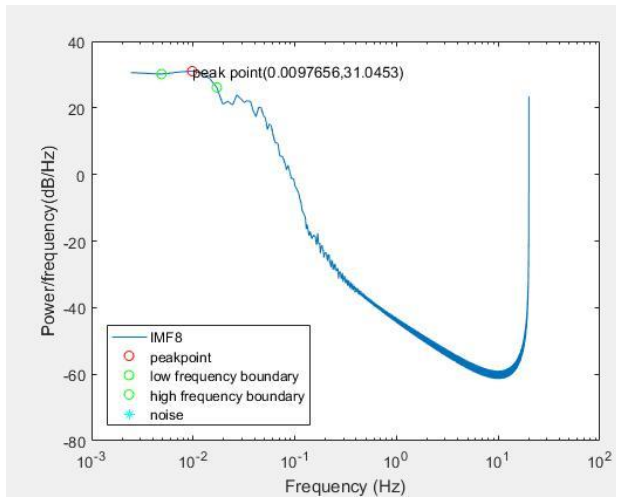
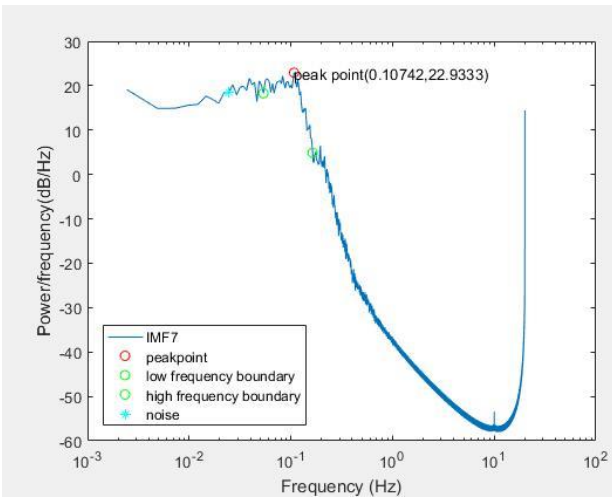
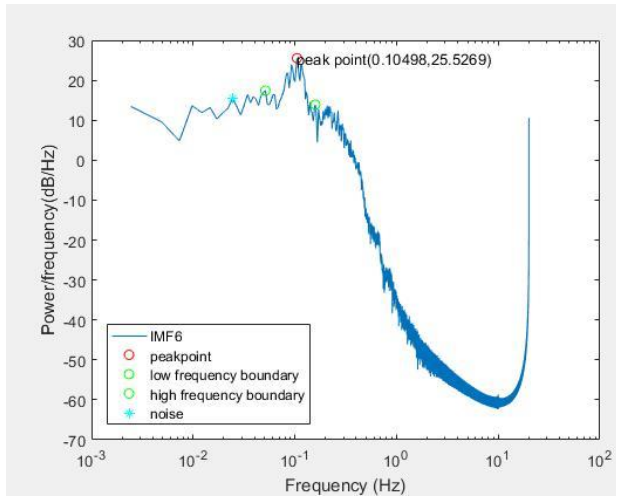
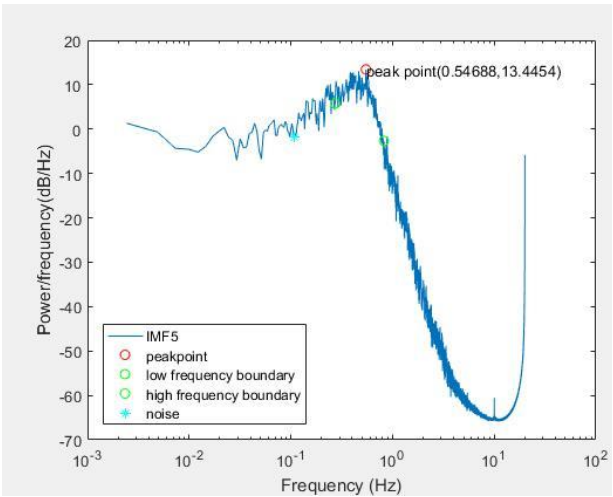
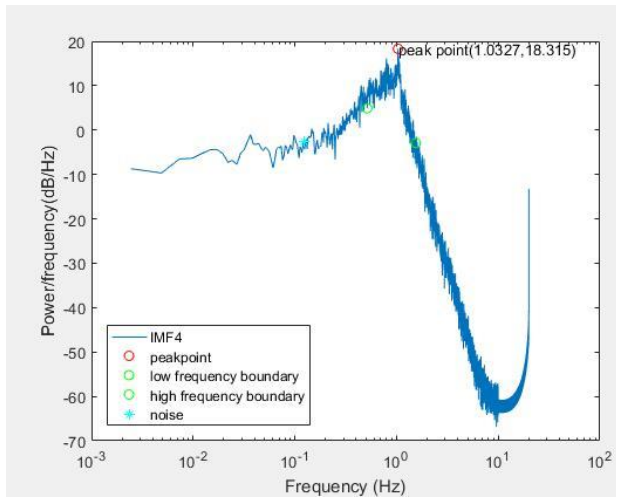
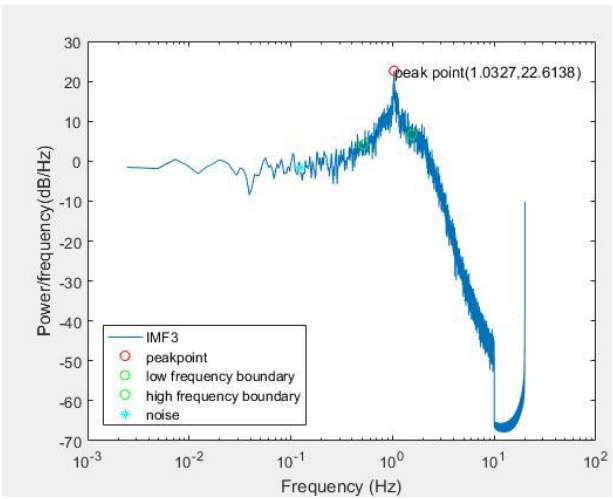


Figure 5-13 Instantaneous power spectrum in the wavelet analysis for an IMF after HHT

## 5.2.2 HHT results





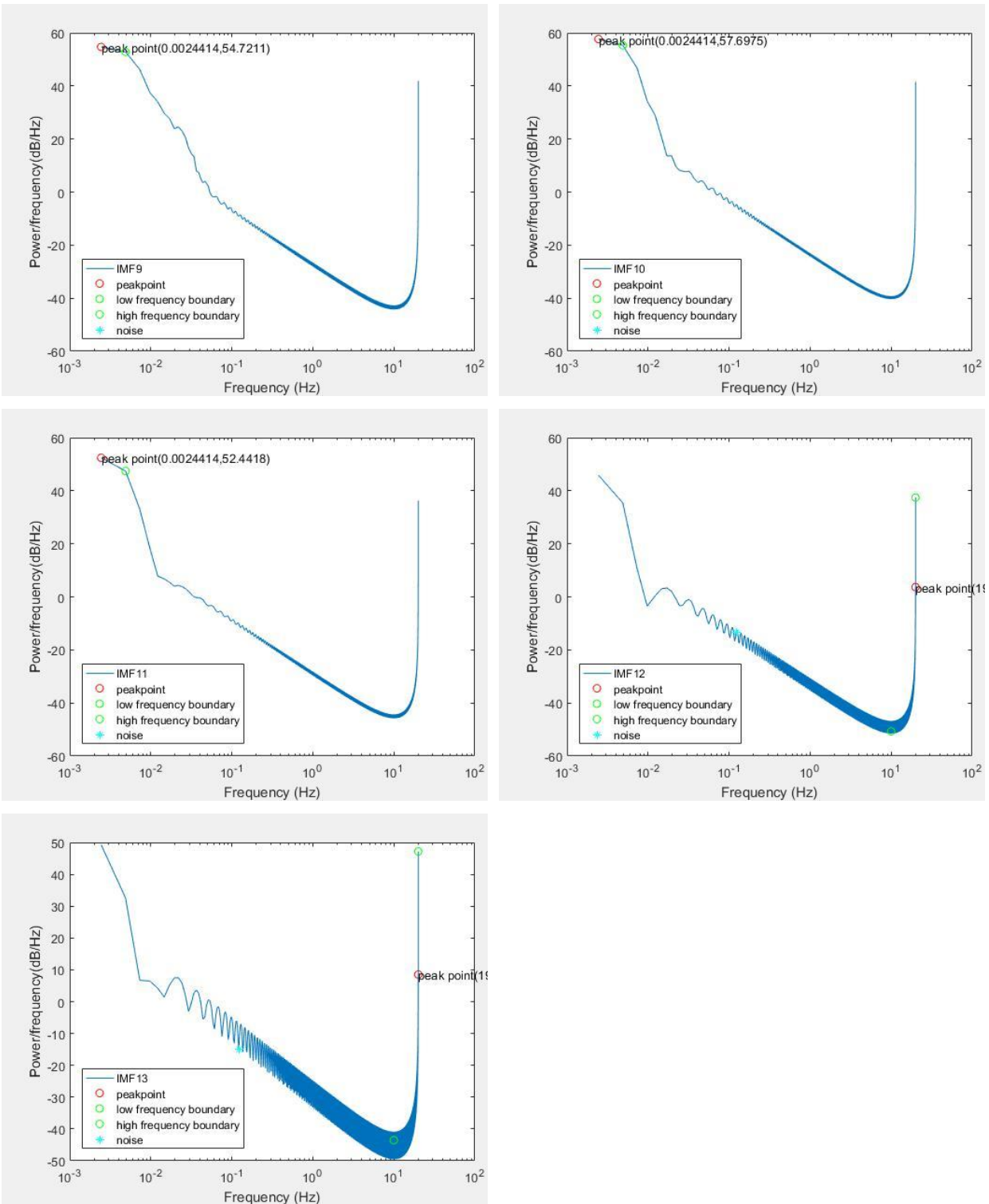
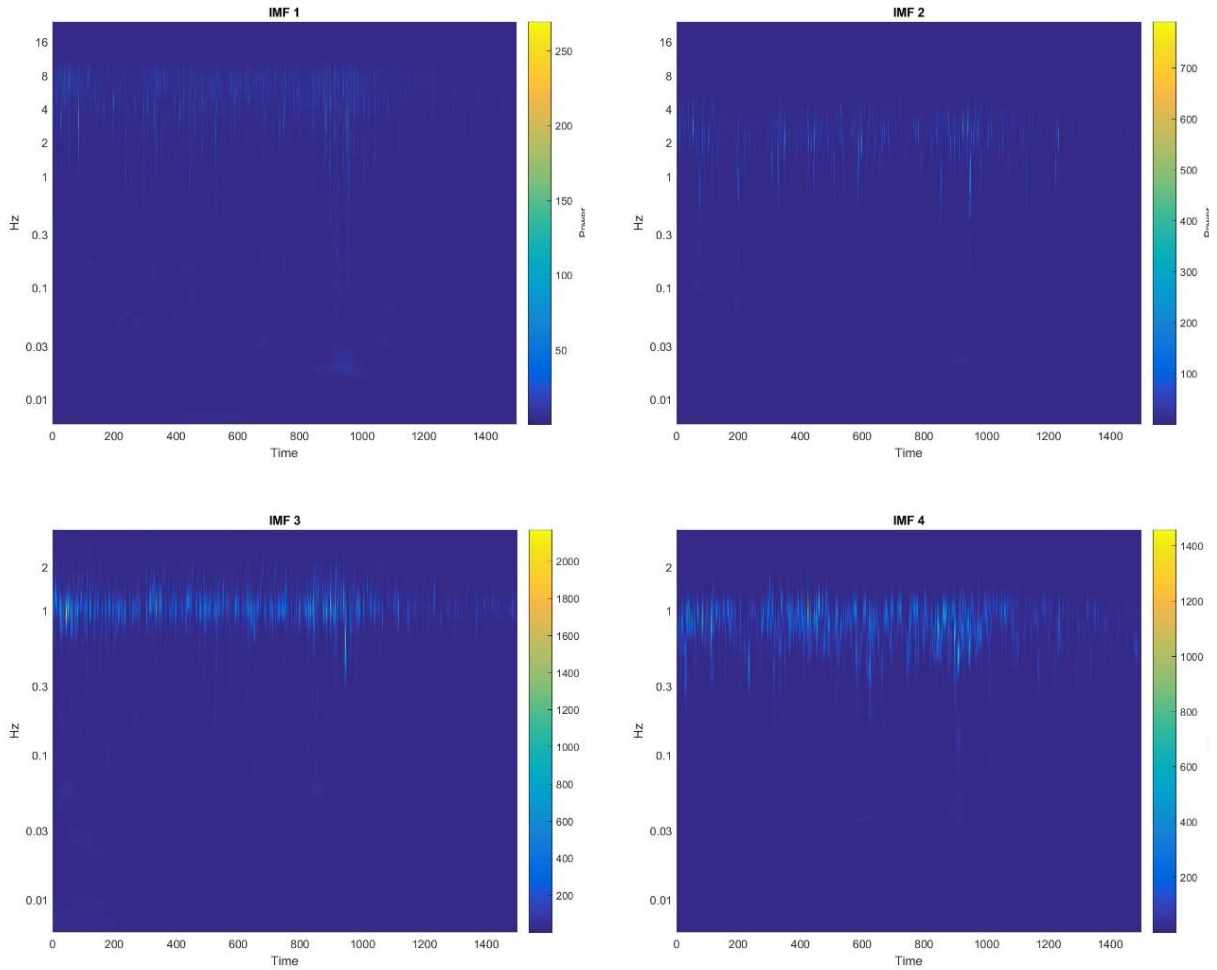
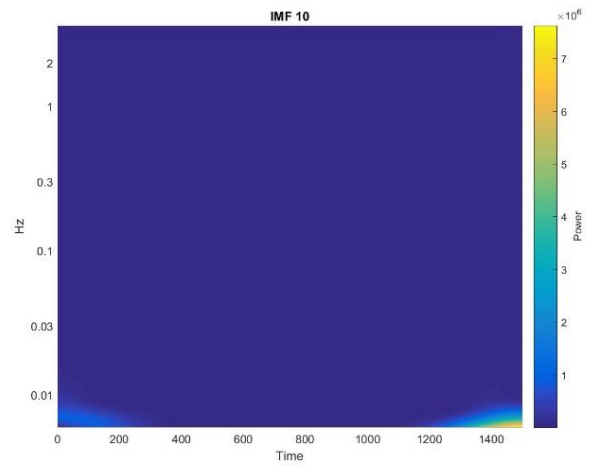
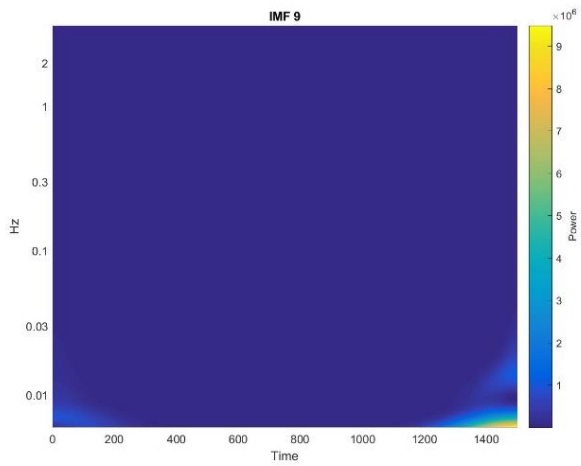
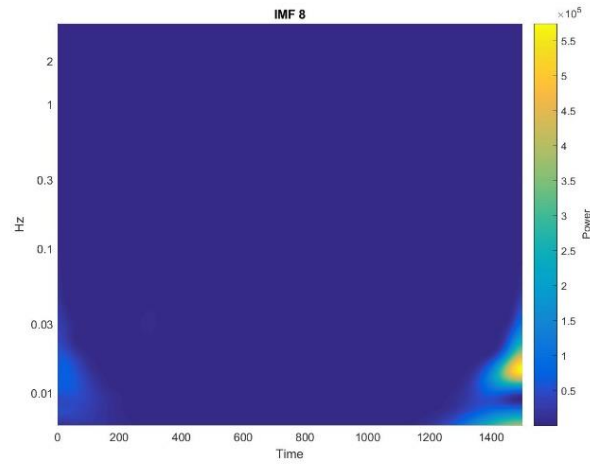
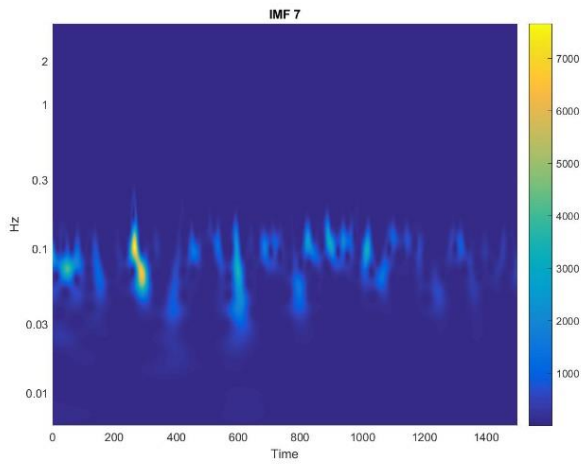
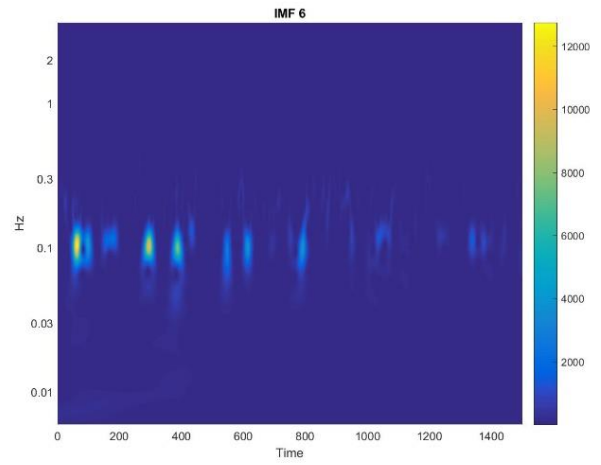
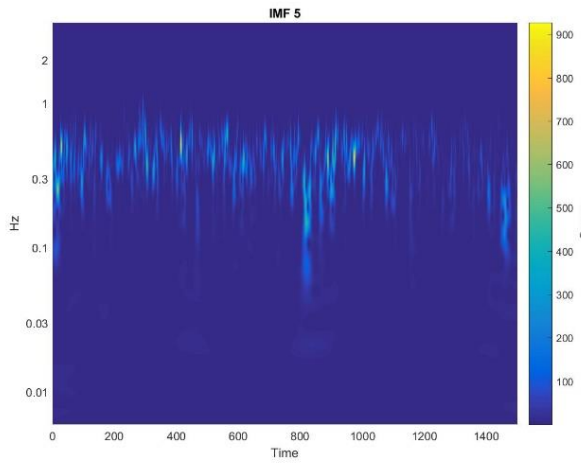


Figure 5-14 The HHT IMFs of measured data of radial artery at the wrist without adding noise

Figure 5-14 displays the 13 IMFs decomposed from a group of LDF signal data without adding noise. The first seven IMFs have distinct peak points, and the frequency of peak points decreases according to the separation sequence of each IMF. The subsequent

wavelet analysis for each IMF is shown in Figure 5-15. The frequency bands around 1 Hz, 0.3 Hz, and 0.1 Hz are apparent in IMF 3, 5, and 6, respectively. The other two frequency bands around 0.03 Hz and 0.01 Hz are indistinct in IMF 8 to 13. Therefore, the latter study is mainly focused on the frequency bands around 1 Hz, 0.3 Hz, and 0.1 Hz.





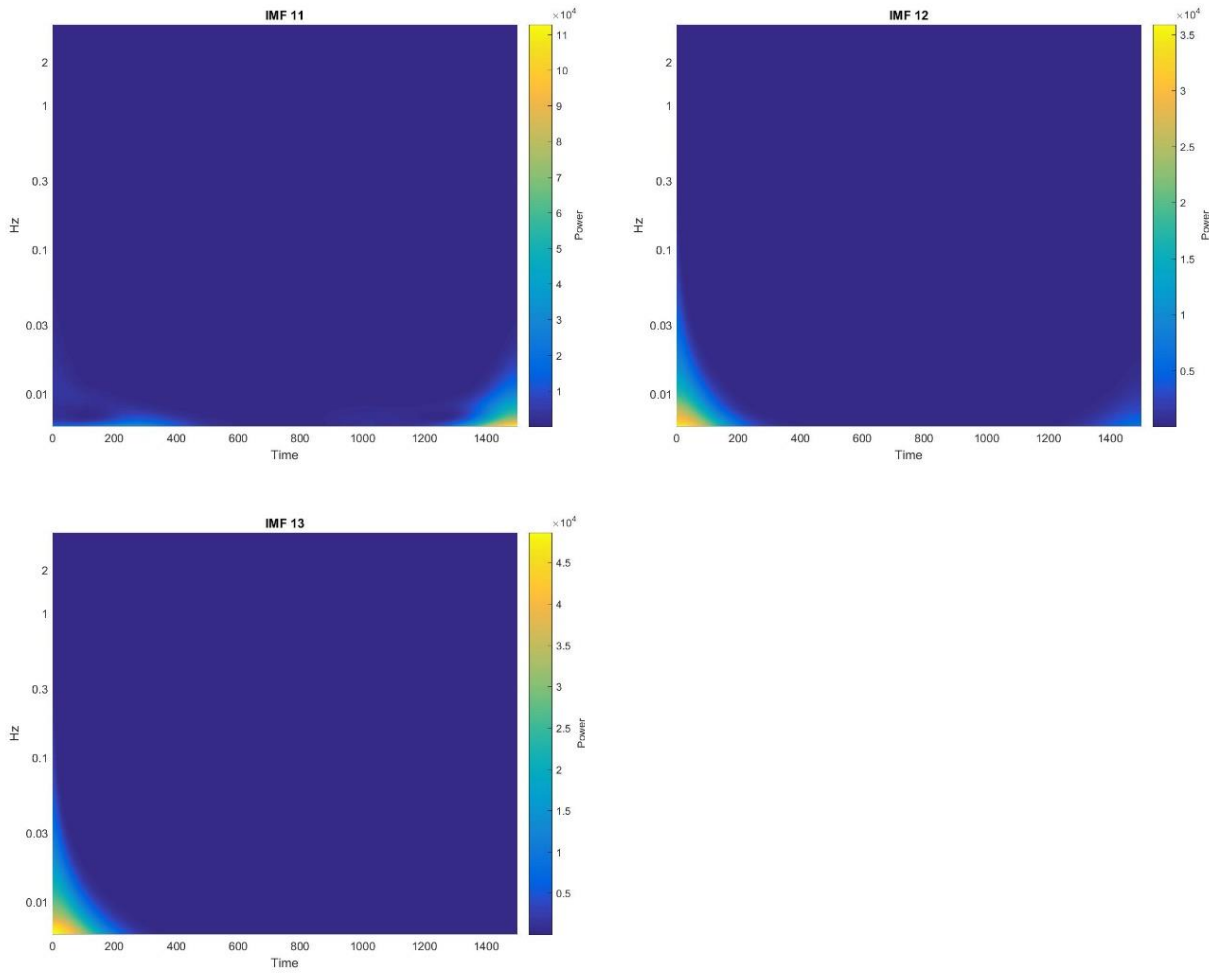
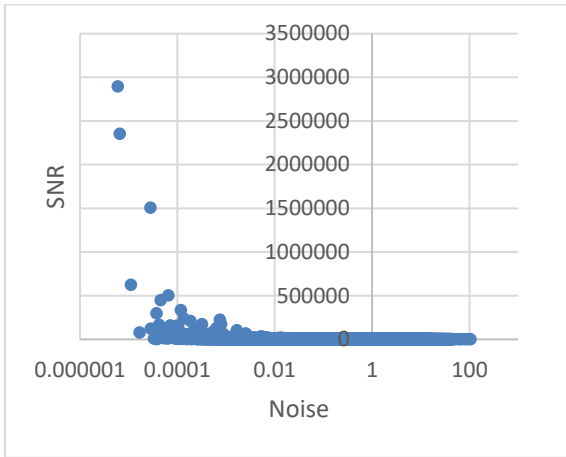
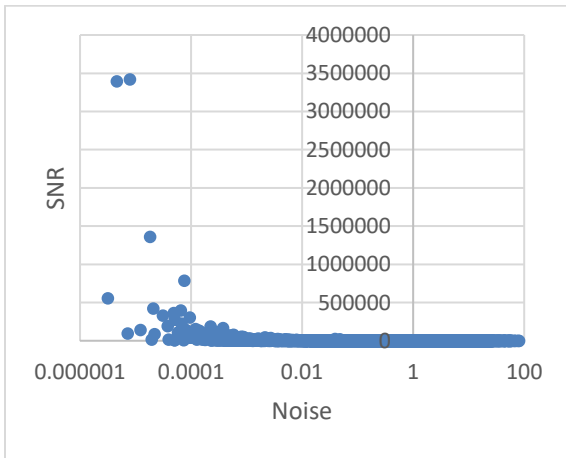


Figure 5-15 The wavelet analysis for IMFs of measured data of radial artery at the wrist without adding noise

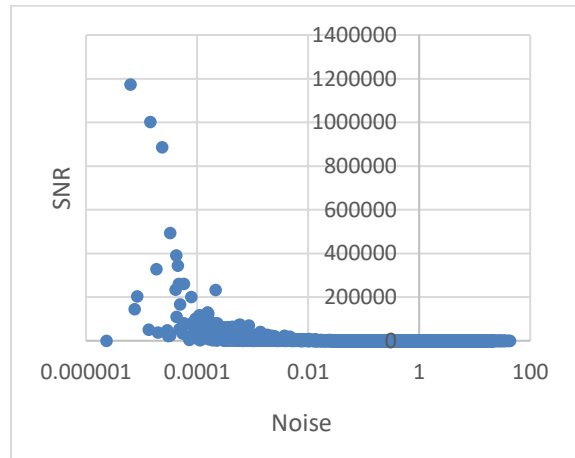
### 5.2.3 Stochastic resonance of different noise



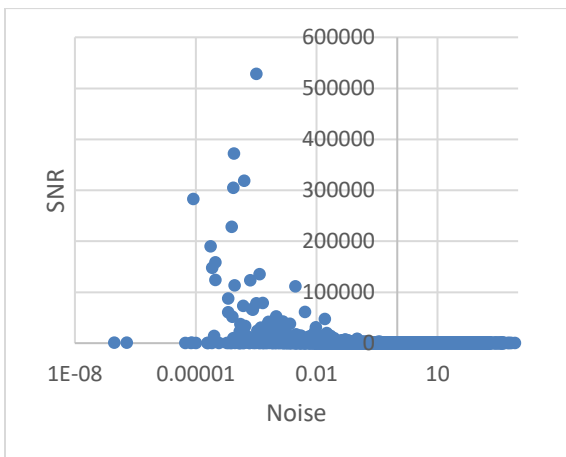
Without adding noise



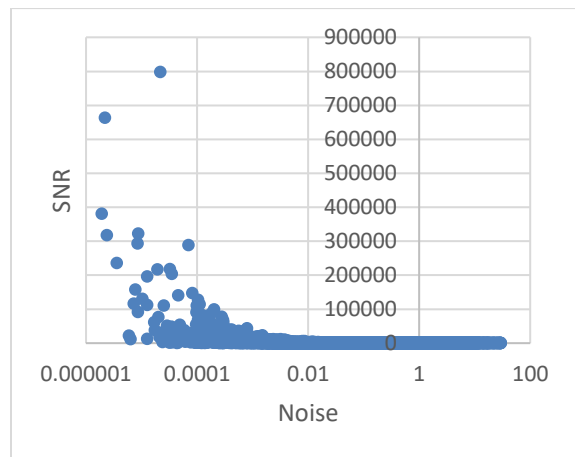
White noise



After adding white noise

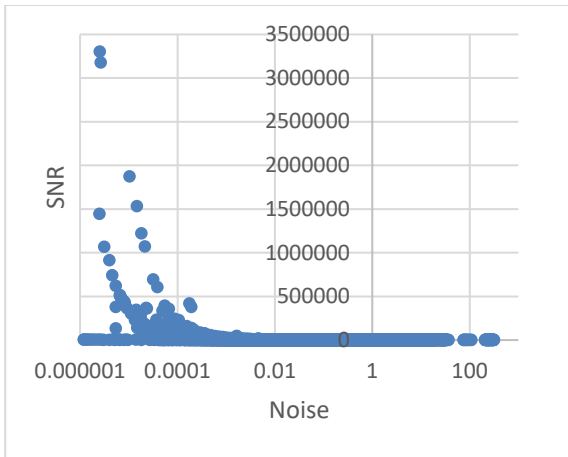


Pink noise

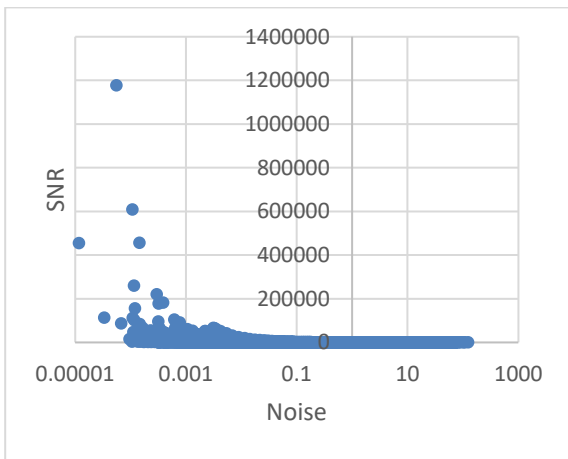


After adding pink noise

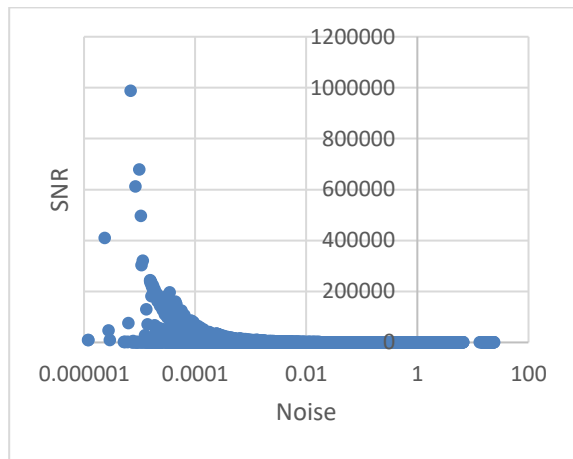
Figure 5-16 Stochastic resonance at 1 Hz



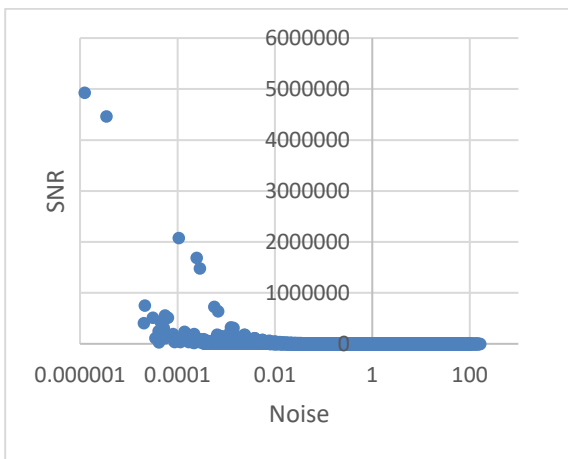
Without adding noise



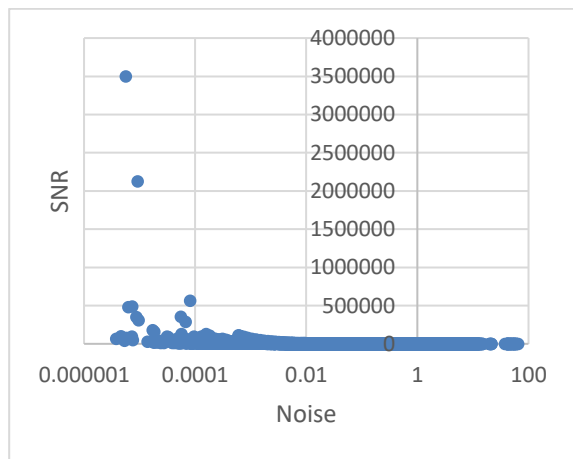
White noise



After adding white noise

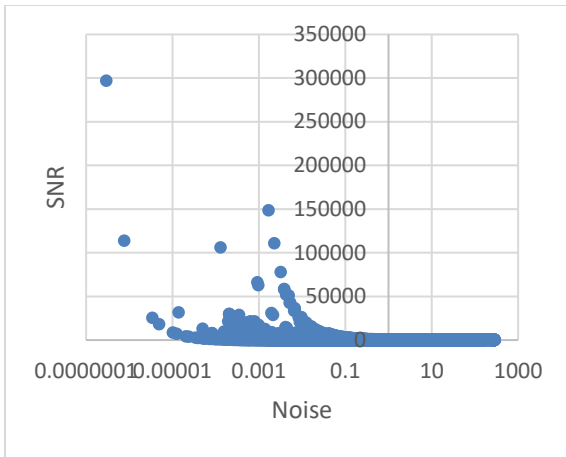


Pink noise

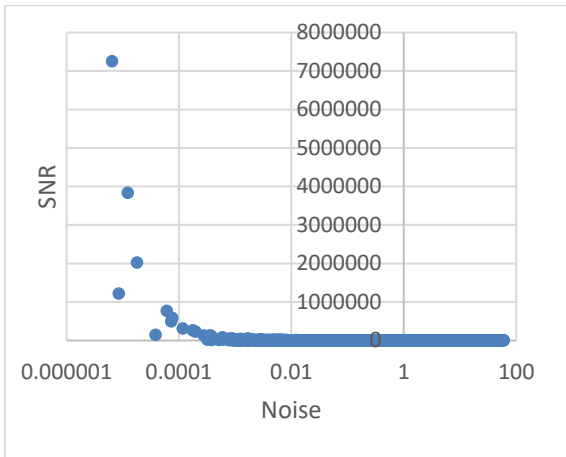


After adding pink noise

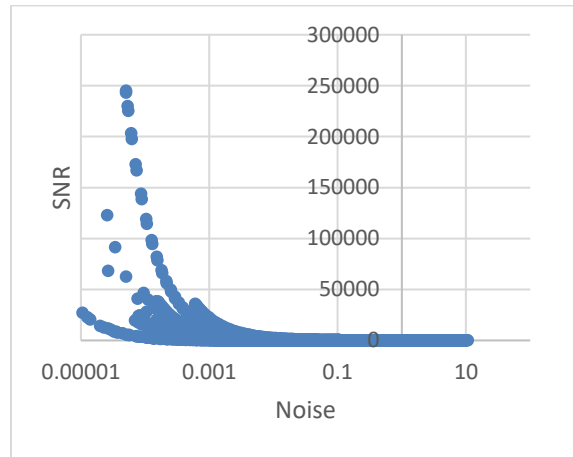
Figure 5-17 Stochastic resonance at 0.3 Hz



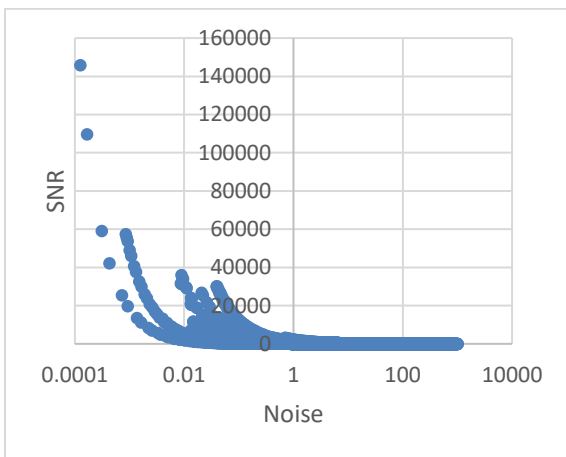
Without adding noise



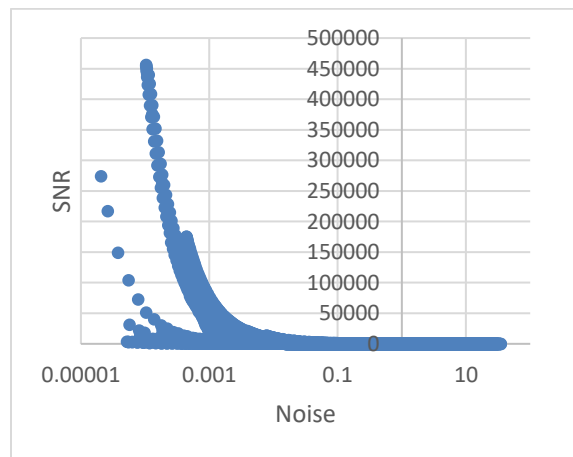
White noise



After adding white noise



Pink noise



After adding pink noise

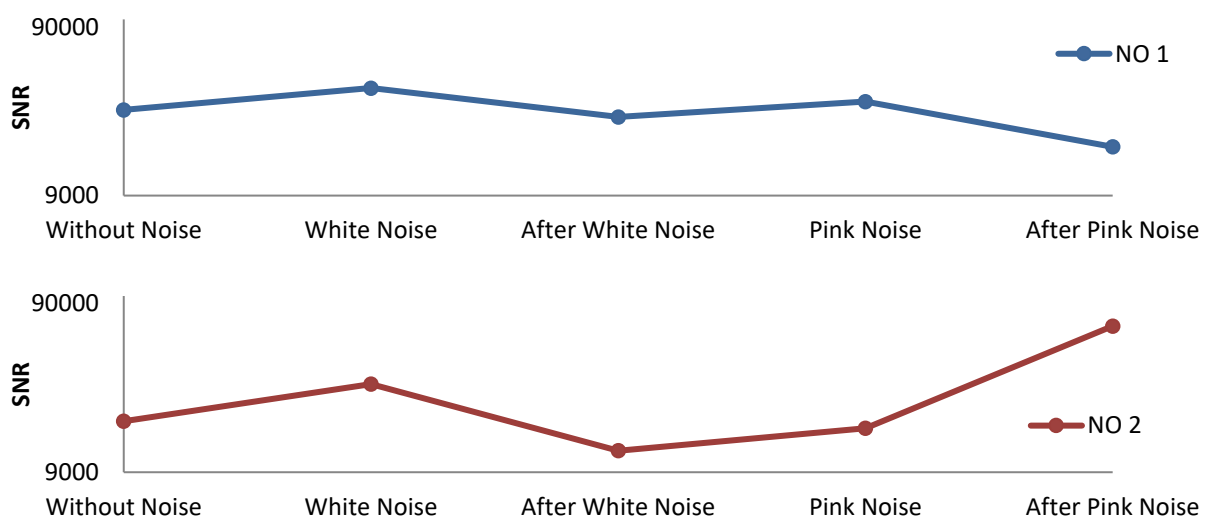
Figure 5-18 Stochastic resonance at 0.1 Hz

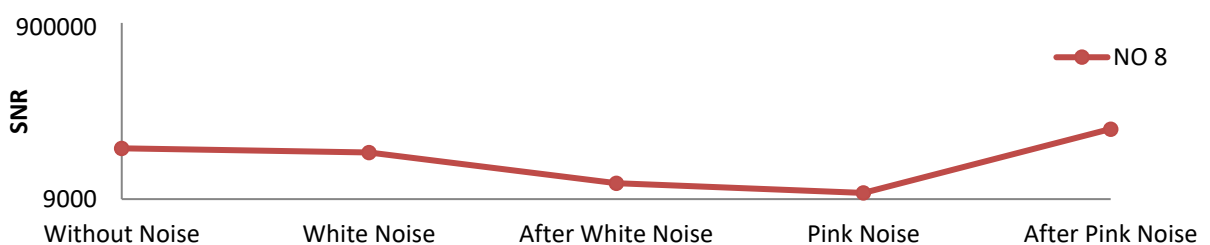
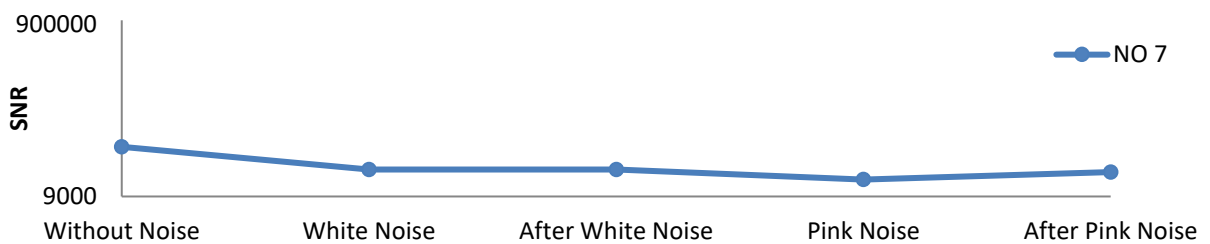
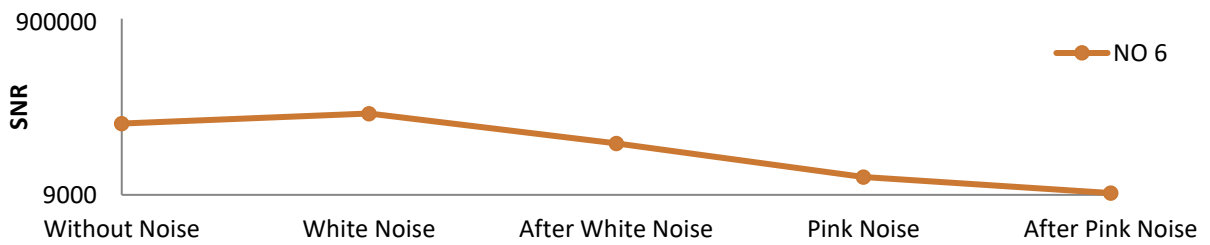
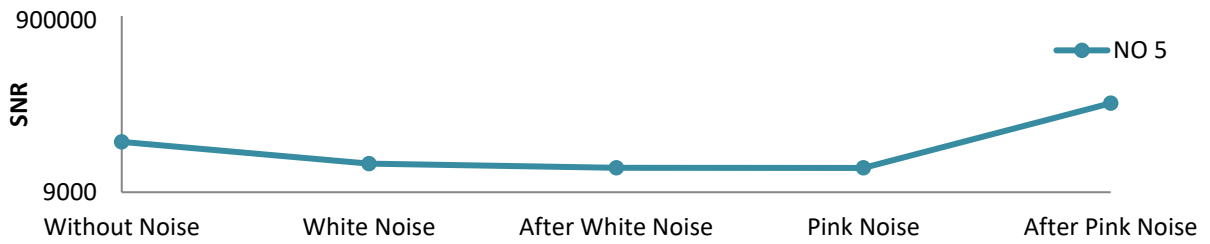
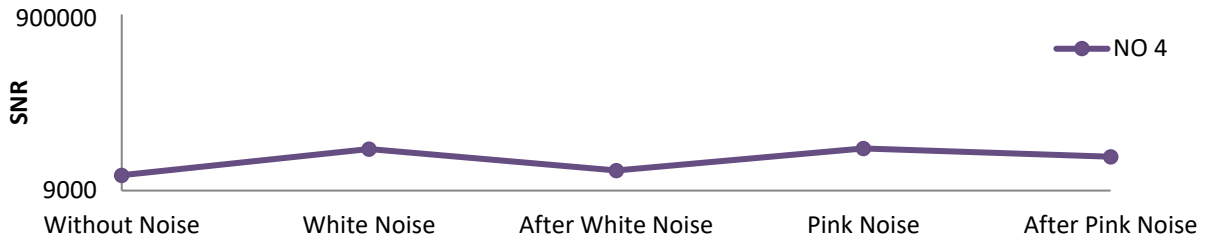
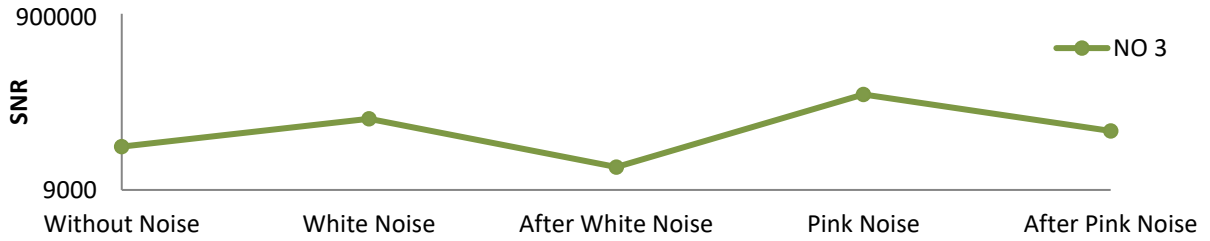
The instantaneous SNR versus instantaneous noise intensity for frequency bands 1 Hz, 0.3 Hz, and 0.1 Hz are illustrated in Figure 5-16, Figure 5-17, and Figure 5-18,

respectively. At a certain noise intensity, the SNR ascends sharply to a peak value then decreases moderately with the increase of noise intensity. There is inherent background noise changing with time in the human cardiovascular system<sup>128</sup>, regardless of whether noise is added. The phenomenon of SR is observed in all these three frequency bands, which means that the phenomenon of SR exists in the human cardiovascular system. From these figures, we cannot find the influence of adding the disturbance of noise to the pulse signal, so the average SNR is then analyzed.

#### 5.2.4 SNR for different disturbances of noise

From Figure 5-16 to Figure 5-18, the maximum SNR is about  $10^3$  to  $10^6$  multiples of the average SNR. Because higher instantaneous SNR contributes a major part, the entire SNR of a signal is represented by the average SNR of the top 1000 largest instantaneous SNR. Figure 5-19 illustrates the average SNR of the top 1000 largest instantaneous SNR of frequency band around 1 Hz. Six experiments represent similar responses to white noise, whose SNR raises after adding white noise and then falls. And there is no commonality in SNR changing pattern which might be induced by pink noise. Figure 5-20 indicates that there is little change in the value of the average SNR of the ten experiments under different noise conditions. The conclusion could be dropped that adding noise has little influence on the SNR of frequency around 1 Hz.





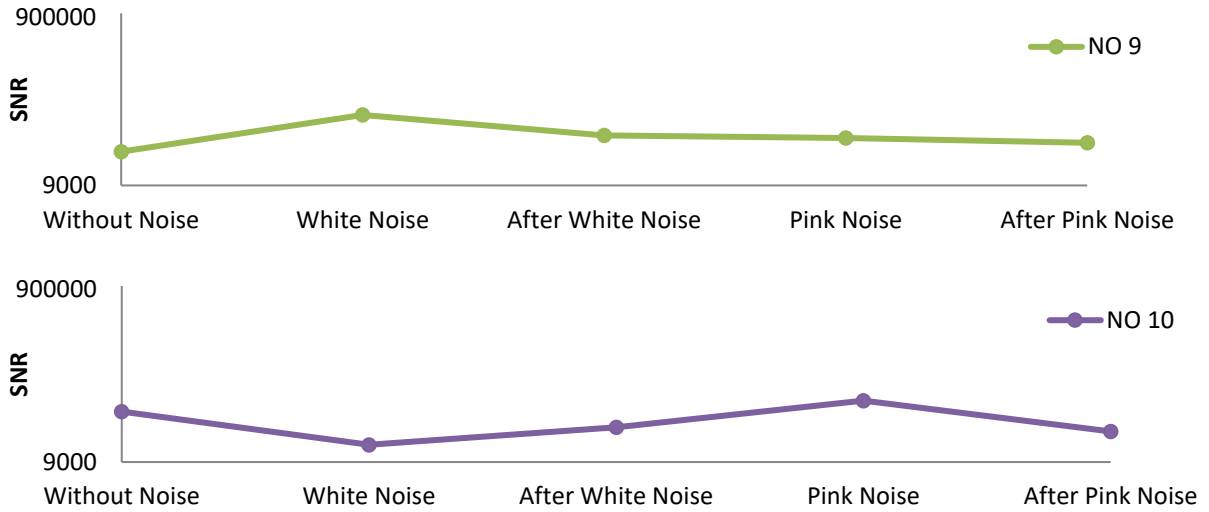


Figure 5-19 The average top 1000 SNR for frequency band around 1 Hz of ten experiments

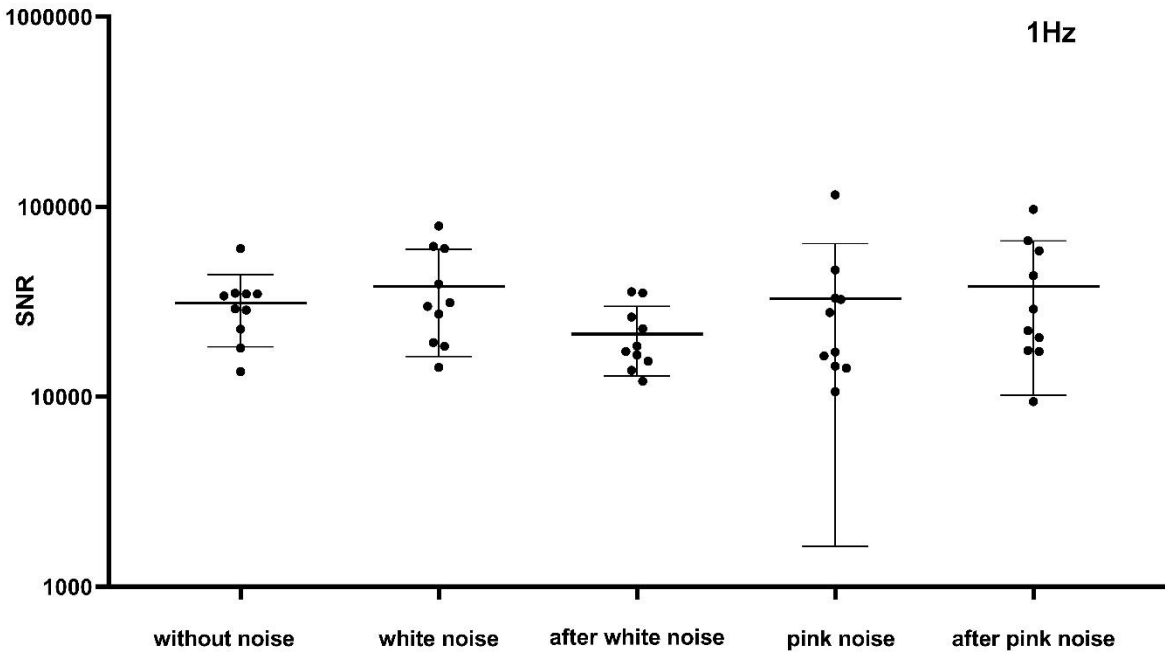
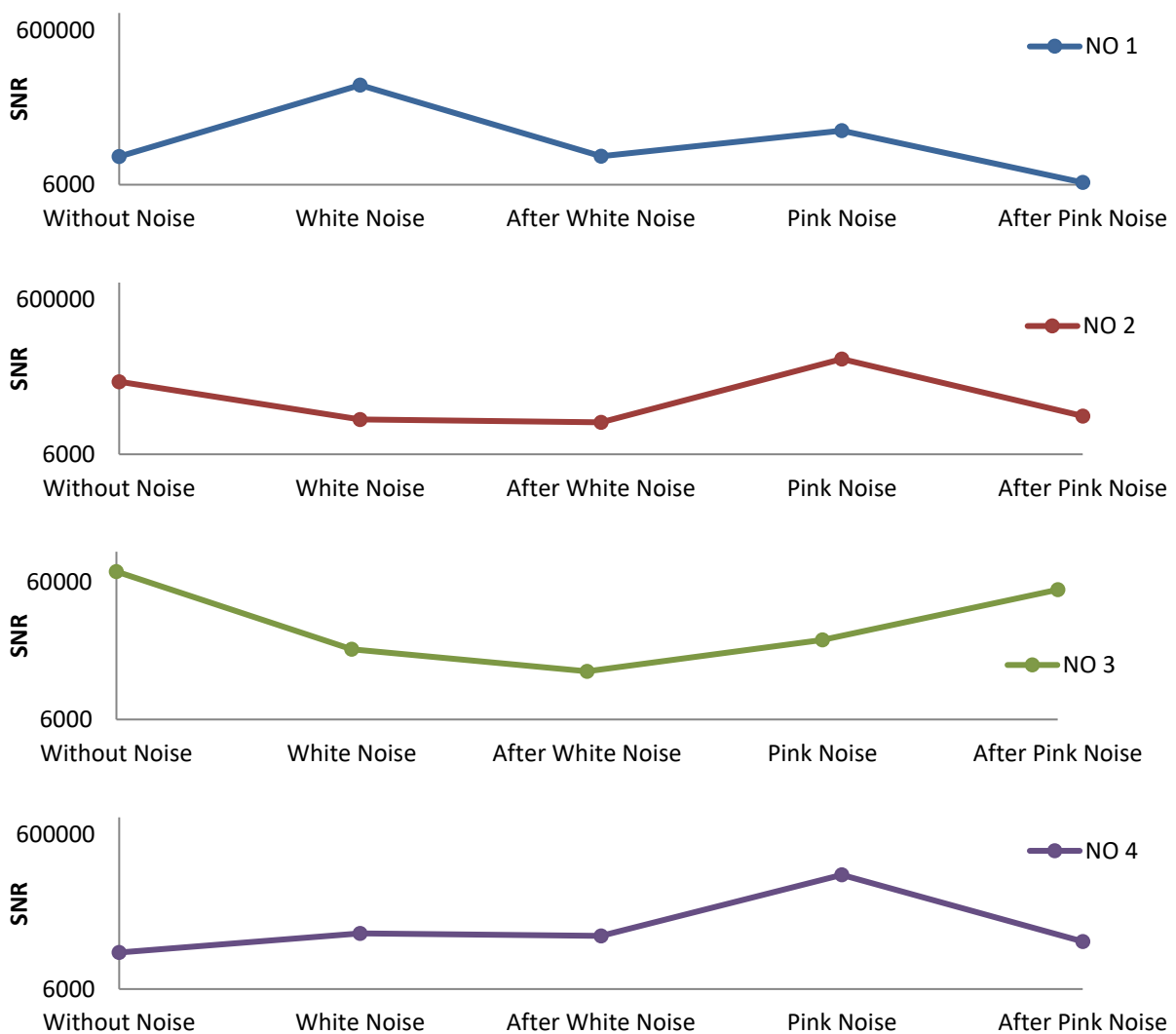


Figure 5-20 The total average top 1000 SNR of ten experiments and their mean  $\pm$  SD at different noise conditions for frequency band around 1 Hz

Figure 5-21 shows the average SNR for the top 1000 largest instantaneous SNR of frequency band around 0.3 Hz. Six experiments have the same trends of SNR that SNR heightens after adding white noise and reduces after stopping white noise. Eight experiments' SNRs strengthen after adding pink noise. Six of the eight experiments' SNRs reduce after stopping pink noise, and two of the eight experiments' SNR increase after withdrawing pink noise. Combined with Figure 5-22, both white and pink noise have

impacts on the pulse signal in the frequency band around 0.3 Hz, and it is evident that after adding white noise the SNR will increase. This frequency band around 0.3 Hz relates to respiration activities. This result is consistent with the baroreflex system mentioned in sections 1.5 and 1.7, where the baroreceptors detect the blood pressure ascent or descent in respiration activities<sup>100,101</sup> and induce a threshold-like behavior related to SR<sup>126,127</sup>. Furthermore, the white noise will significantly enhance the frequency signals around 0.3 Hz, and the pink noise will moderately enhance the frequency signals around 0.3 Hz.



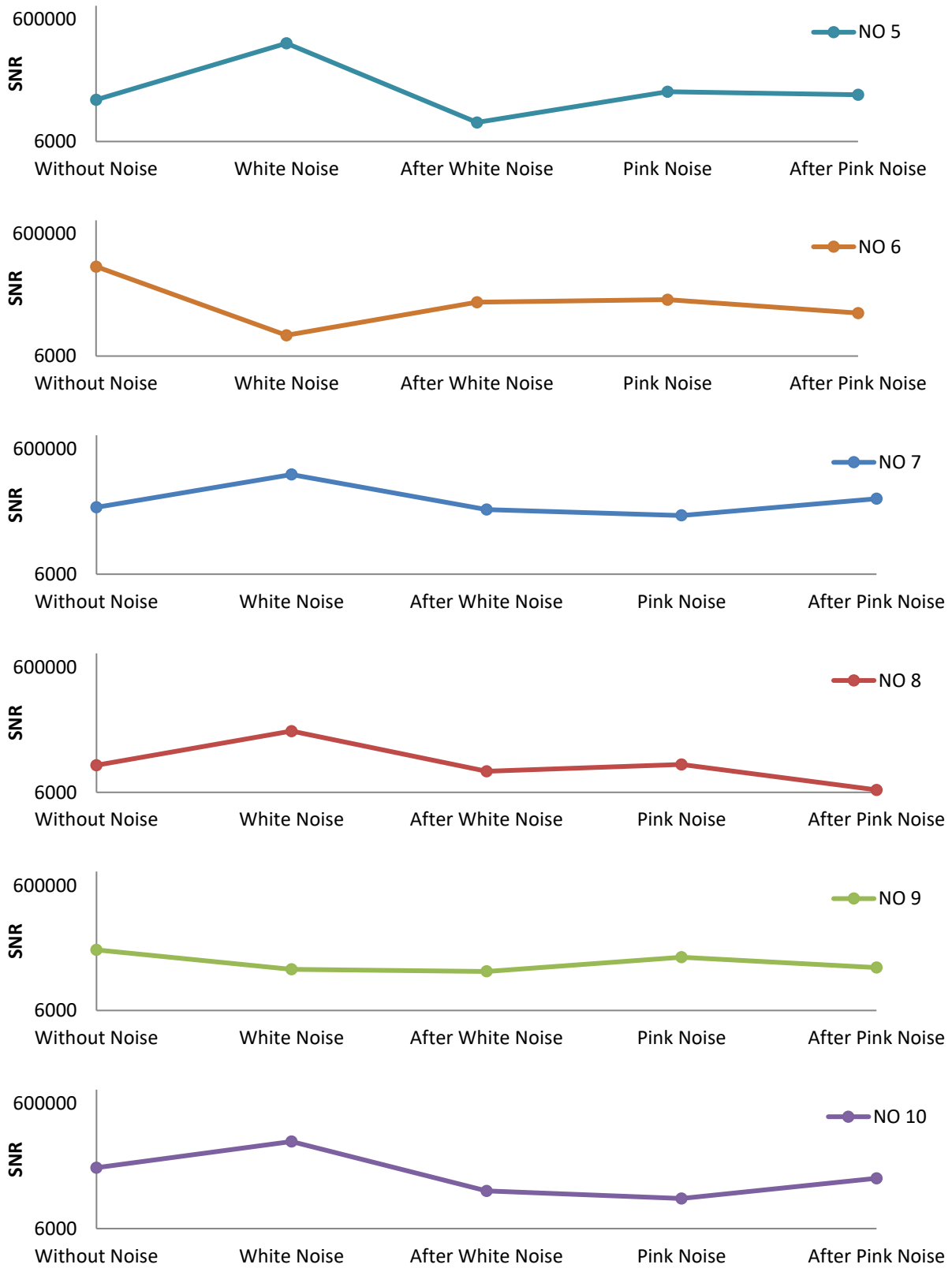


Figure 5-21 The average top 1000 SNR for frequency band around 0.3 Hz of ten experiments

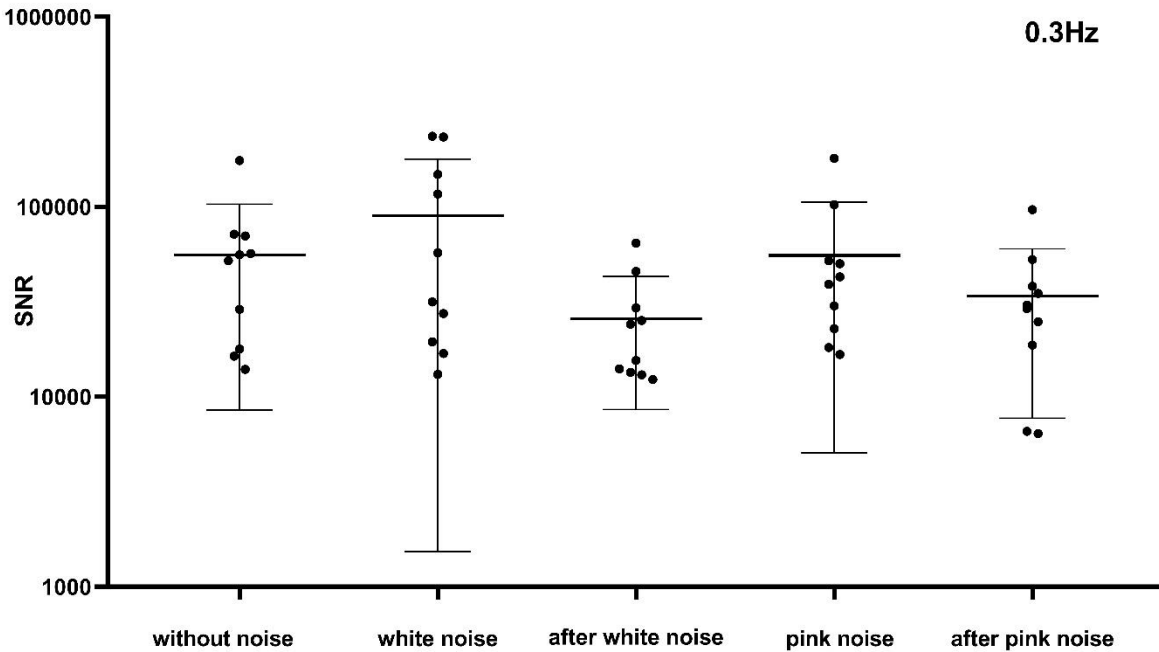
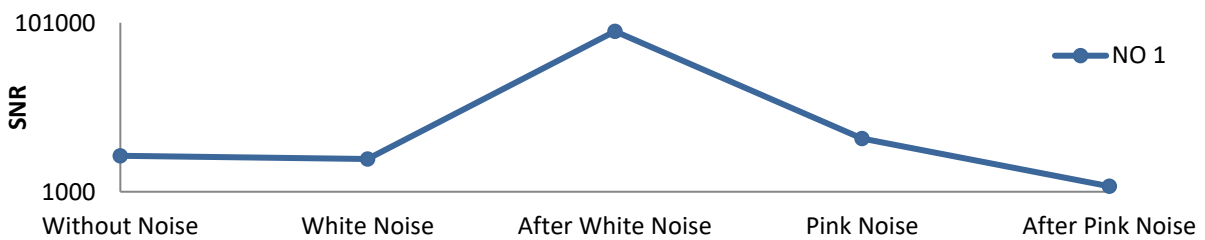
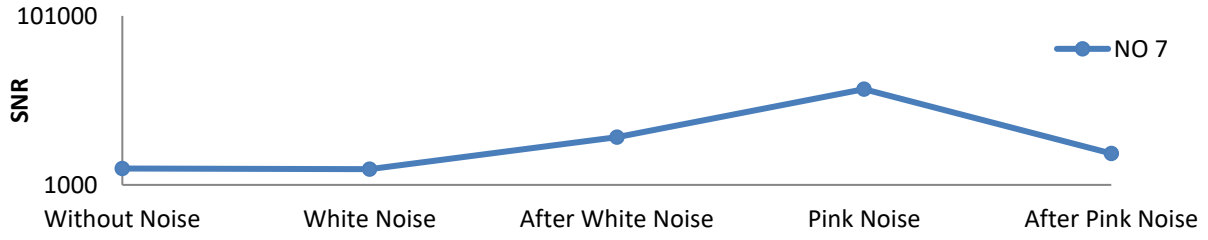
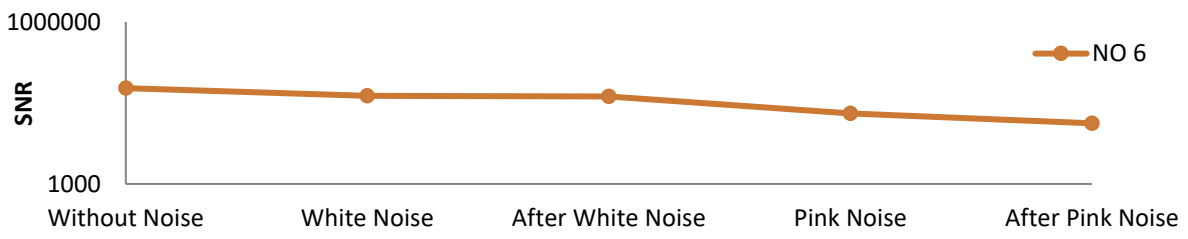
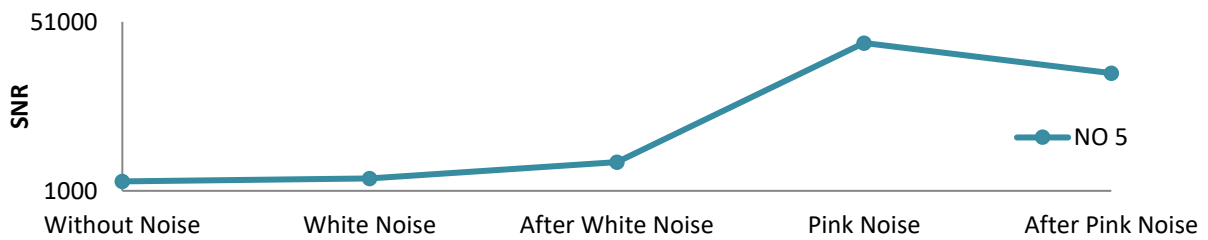
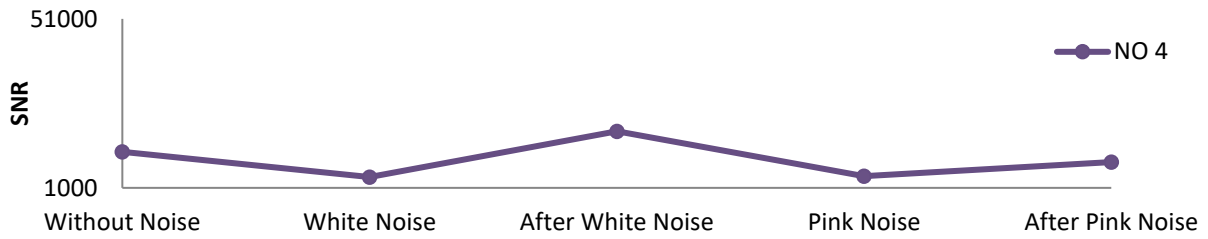
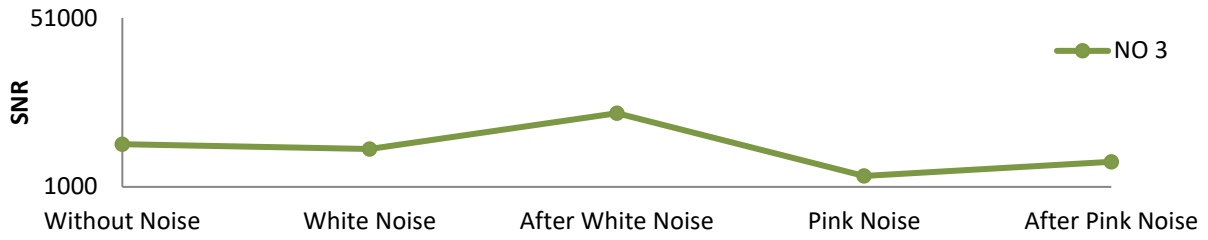
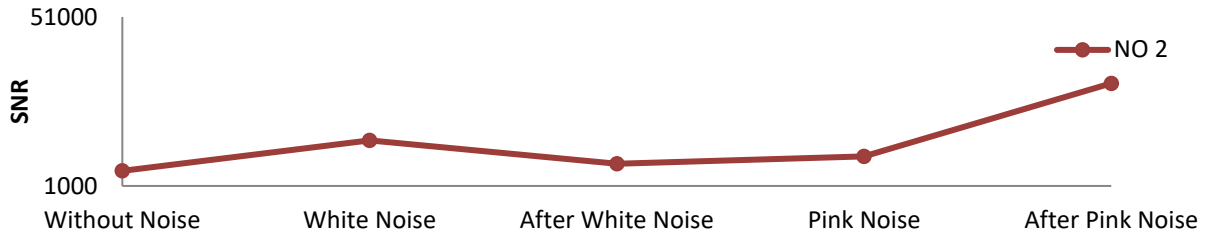


Figure 5-22 The total average top 1000 SNR of ten experiments and their mean  $\pm$  SD at different noise conditions for frequency band around 0.3 Hz

Figure 5-23 shows the average SNR for the top 1000 largest instantaneous SNR of frequency band around 0.1 Hz. In eight of the ten experiments, SNR will increase after withdrawing white noise. Same as the trend of the SNR change in the frequency band around 1 Hz, the SNR has no apparent change after adding pink noise. From Figure 5-24, the SNR of frequency band around 0.1 Hz in the experiment condition after stopping white noise shows a clear difference to that before adding white noise. Therefore, it is evident that adding white noise then stopping white noise would induce an increase in the SNR of the frequency band around 0.1 Hz.





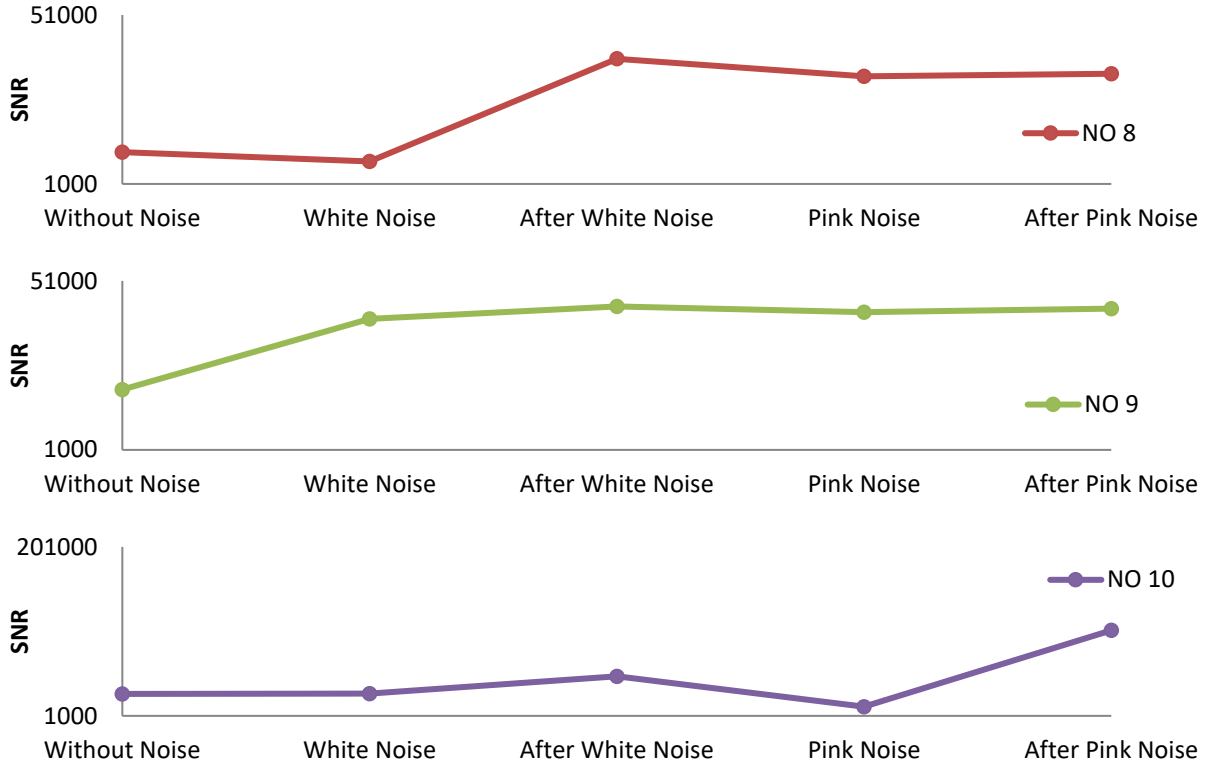


Figure 5-23 The average top 1000 SNR for frequency band around 0.1 Hz of ten experiments

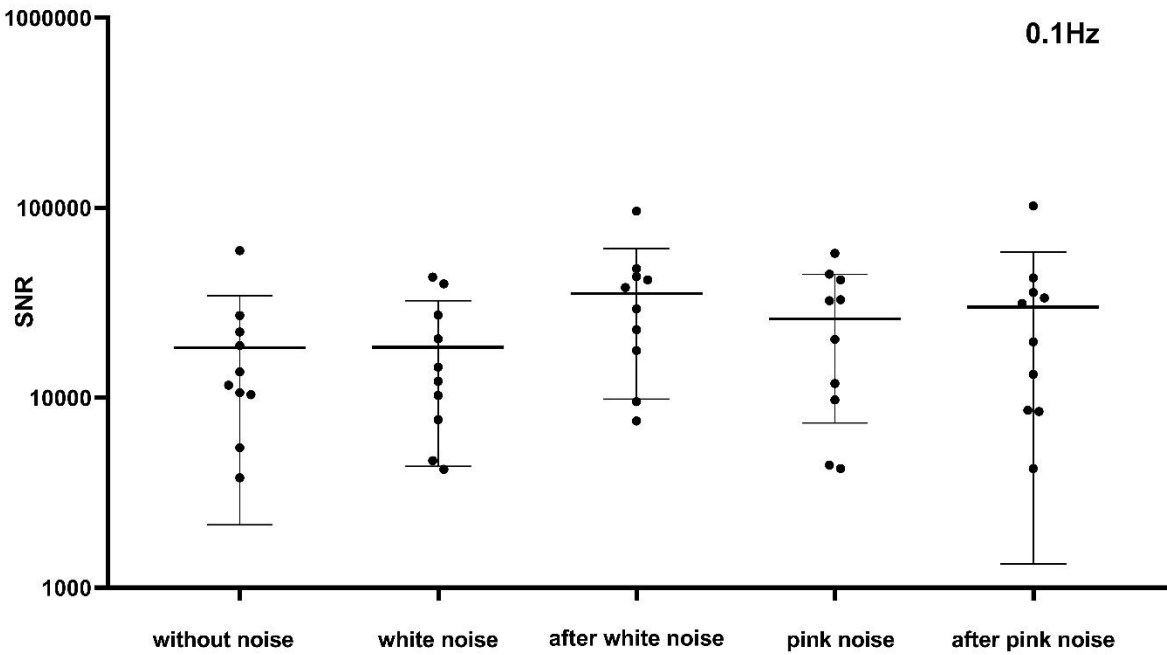


Figure 5-24 The average top 1000 SNR of ten experiments and their mean  $\pm$  SD at different noise conditions for frequency band around 0.1 Hz

## Chapter 6 Conclusions and future work

### 6.1 Conclusions

In this thesis, numerical simulations of blood flow in different models are carried out. Different geometries and different inlet frequencies based on measured heart period are studied for their influences on blood flow oscillations. The numerical results have been processed with wavelet analysis and mean wavelet analysis in order to acquire the blood flow oscillation frequencies. The analyzed results lead to the following conclusions: (1) interconnected vasculature induces nonlinear effect; (2) the power spectrum of low-frequency blood flow oscillations is more prominent at the connections distant from inlet and outlet than those at the connections close to inlet and outlet and those at main arteries; and (3) the low-frequency blood flow oscillations may be related to the harmonics or the subharmonics of the heart rate variation frequency. In summary, the low-frequency blood flow oscillations are induced by the variation of heart period and nonlinear vasculature. And the induced low-frequency blood flow oscillations stimulate the release of calcium flux which then stimulate the smooth muscles contraction and result in vasomotion.

Based on the LDF measured radial artery blood flow signals at the wrist, two groups of data, namely reconstructed and average data, were acquired by constructing a sinusoidal flow velocity model using important features from the experimental data. The reconstructed and the experimental data displayed remarkably similar features in their results of wavelet analysis and mean wavelet analysis. More importantly, in the mean wavelet analysis plots, the experimental data, the reconstructed data, and the average data shared an almost identical low-frequency band from 0.01 Hz to 0.2 Hz. The physical meaning of average data is the average blood flux in each heart period, so it can be speculated that the low-frequency band (0.01~0.2Hz) in the experimental data originates from the variation of the heartbeat period, or that the origin of vasomotion is from the heart beating period variation.

To investigate the effect of pressure on the blood flow oscillation, different cuff pressures were added to the radial arterial blood flow. The SNRs of different frequency bands (~1 Hz, ~0.3 Hz, ~0.1 Hz, 0.03 Hz, and 0.01 Hz) in the pulse signals changed with pressure.

We can infer that the ancient Chinese physicians diagnosed by applying pressures to the wrist to sense the SNR changes of different frequency bands in the pulse signals which relates to cardiac, respiratory, myogenic, neurogenic, and endothelial activities. To investigate the effect of noise on the stochastic resonance of blood flow oscillation, different noise disturbances were added and the measured signals were decomposed by HHT. By comparing the changes of SNRs for different frequency bands under different noise conditions, we could speculate that (1) the noise has little influence on the frequency band related to cardiac activities ( $\sim 1$  Hz); (2) both white noise and pink noise have impacts on the pulse signal in the frequency band related to respiratory activities ( $\sim 0.3$  Hz); and (3) adding white noise and then stopping white noise will induce a SNR increase in the frequency band related to vasomotion ( $\sim 0.1$  Hz).

## 6.2 Future work

In the numerical simulation part, subsequent research will focus on:

- (1) Further investigation into the relationship between blood flow oscillation and the vasculature, e.g., vessel diameter, length, and bifurcation.
- (2) The effect of more complicated vascular structure on low-frequency oscillations of blood flow.
- (3) Simulations are carried out on the realistic vasculature models, which can be obtained by 3D MRI scanning.
- (4) The influence of different quasi-period on blood flow oscillations.
- (5) Further investigation of the simulation model using the fluid-structure interaction method, and exploration of the relationship between blood flow oscillation and the young's modulus of the vessel wall and the relationship between blood flow oscillation and vessel wall oscillation.

The further experimental study will include:

- (1) Additional experiments on healthy subjects with different anthropometric parameters, e.g. age and weight.
- (2) More experiments on subjects with different diseases, e.g., hypertension, diabetes, and obesity.
- (3) More experiments for blood flow oscillations in arteries other than the radial artery to investigate whether SR phenomenon is involved in these arteries and the effect of different disturbances on SNRs of different frequency bands.

## Reference

1. Stergiopoulos N, Porret C-A, De Brouwer S, Meister J-J. Arterial vasomotion: effect of flow and evidence of nonlinear dynamics. *American Journal of Physiology-Heart and Circulatory Physiology*. 1998;274(6):H1858-H1864.
2. ROSS G, Stinson E, SCHROEDER Jt, Ginsburg R. Spontaneous phasic activity of isolated human coronary arteries. *Cardiovascular research*. 1980;14(10):613-618.
3. Aalkjaer C, Mulvany MJ. Structure and Function of the Microcirculation. In: *Microcirculation in Cardiovascular Diseases*. Springer; 2020:1-14.
4. Holowatz LA, Thompson-Torgerson CS, Kenney WL. The human cutaneous circulation as a model of generalized microvascular function. *J Appl Physiol* (1985). 2008;105(1):370-372.
5. Smith JF. *An investigation of the underlying mechanisms of arterial vasomotion*, University of Oxford; 2020.
6. Fonseca DA, Antunes PE, Antunes MJ, Cotrim MD. Vasomotion as an oscillatory sign of functional impairment in the human internal thoracic artery: A study based on risk factors and vessel reactivity. *Experimental physiology*. 2018;103(7):1030-1038.
7. Jones TW. X. Discovery that the veins of the bat's wing (which are furnished with valves) are endowed with rythmical contractility, and that the onward flow of blood is accelerated by each contraction. *Philosophical Transactions of the Royal Society of London*. 1852;142:131-136.
8. Rossi M, Carpi A, Di Maria C, Galetta F, Santoro G. Spectral analysis of laser Doppler skin blood flow oscillations in human essential arterial hypertension. *Microvascular research*. 2006;72(1-2):34-41.
9. Jones W. Discovery that the veins of the Bats' wing are enlowed with rhythmical contractility etc. *Philosophic. Trans*. 1852.
10. Gustafsson H, Mulvany M, Nilsson H. Rhythmic contractions of isolated small arteries from rat: influence of the endothelium. *Acta Physiologica*. 1993;148(2):153-163.
11. Fagrell B, Fronck A, Intaglietta M. A microscope-television system for studying flow velocity in human skin capillaries. *American Journal of Physiology-Heart and Circulatory Physiology*. 1977;233(2):H318-H321.
12. Mahler F, Muheim M, Intaglietta M, Bollinger A, Anliker M. Blood pressure fluctuations in human nailfold capillaries. *American Journal of Physiology-Heart and Circulatory Physiology*. 1979;236(6):H888-H893.
13. Braverman IM, Keh A, Goldminz D. Correlation of laser Doppler wave patterns with underlying microvascular anatomy. *Journal of Investigative Dermatology*. 1990;95(3):283-286.
14. Kastrup J, Bulow J, Lassen N. Vasomotion in human skin before and after local heating recorded with laser Doppler flowmetry. A method for induction of vasomotion. *Int J Microcirc Clin Exp*. 1989;8(2):205-215.
15. Bertuglia S, Colantuoni A, Arnold M, Witte H. Dynamic coherence analysis of vasomotion and flow motion in skeletal muscle microcirculation. *Microvascular Research*. 1996;52(3):235-244.
16. Müick-Weymann M, Albrecht H-P, Hager D, Hiller D, Hornstein O, Bauer R. Respiratory-dependent laser–Doppler flux motion in different skin areas and its meaning

- to autonomic nervous control of the vessels of the skin. *Microvascular research*. 1996;52(1):69-78.
17. Bračić M, Stefanovska A. Wavelet-based analysis of human blood-flow dynamics. *Bulletin of mathematical biology*. 1998;60(5):919-935.
  18. Stefanovska A, Bracic M, Kvernmo HD. Wavelet analysis of oscillations in the peripheral blood circulation measured by laser Doppler technique. *IEEE Transactions on Biomedical Engineering*. 1999;46(10):1230-1239.
  19. Söderström T, Stefanovska A, Veber M, Svensson H. Involvement of sympathetic nerve activity in skin blood flow oscillations in humans. *American Journal of Physiology-Heart and Circulatory Physiology*. 2003;284(5):H1638-H1646.
  20. Cracowski JL, Minson CT, Salvat-Melis M, Halliwill JR. Methodological issues in the assessment of skin microvascular endothelial function in humans. *Trends Pharmacol Sci*. 2006;27(9):503-508.
  21. Stefanovska A. Coupled oscillators: complex but not complicated cardiovascular and brain interactions. *IEEE Engineering in medicine and biology magazine*. 2007;26(6).
  22. Nilsson H, Aalkjaer C. Vasomotion: mechanisms and physiological importance. *Molecular Interventions*. 2003;3(2):79.
  23. Aalkjaer C, Boedtkjer D, Matchkov V. Vasomotion - what is currently thought? *Acta Physiologica*. 2011;202(3):253-269.
  24. Kvandal P, Landsverk SA, Bernjak A, Stefanovska A, Kvernmo HD, Kirkebøen KA. Low-frequency oscillations of the laser Doppler perfusion signal in human skin. *Microvascular Research*. 2006;72(3):120-127.
  25. Bouskela E, Grampp W. Spontaneous vasomotion in hamster cheek pouch arterioles in varying experimental conditions. *American Journal of Physiology*. 1992;262(2):478-485.
  26. Kaufman AG, Intaglietta M. Automated diameter measurement of vasomotion by cross-correlation. *International Journal of Microcirculation Clinical & Experimental*. 1985;4(1):45-53.
  27. Hu S, Maslov K, Wang LV. Noninvasive label-free imaging of microhemodynamics by optical-resolution photoacoustic microscopy. *Optics Express*. 2009;17(9):7688.
  28. Colantuoni A, Bertuglia S, Intaglietta M. Quantitation of rhythmic diameter changes in arterial microcirculation. *American Journal of Physiology-Heart and Circulatory Physiology*. 1984;246(4):H508-H517.
  29. Wiederhielm CA, Weston BV. Microvascular, lymphatic, and tissue pressures in the unanesthetized mammal. *American Journal of Physiology-Legacy Content*. 1973;225(4):992-996.
  30. Hsiu H, Hu H-F, Tsai H-C. Differences in laser-Doppler indices between skin-surface measurement sites in subjects with diabetes. *Microvascular research*. 2018;115:1-7.
  31. Schmidt JA, Borgström P, Firestone GP, von Wichert P, Intaglietta M, Fronck A. Periodic hemodynamics (flow motion) in peripheral arterial occlusive disease. *Journal of vascular surgery*. 1993;18(2):207-215.
  32. Mizeva I, Zharkikh E, Dremin V, et al. Spectral analysis of the blood flow in the foot microvascular bed during thermal testing in patients with diabetes mellitus. *Microvascular research*. 2018;120:13-20.
  33. Nilsson GE, Tenland T, Oberg PA. A new instrument for continuous measurement of tissue blood flow by light beating spectroscopy. *IEEE Transactions on Biomedical Engineering*. 1980(1):12-19.

34. Bollinger A, Hoffmann U, Franzeck U. Evaluation of flux motion in man by the laser Doppler technique. *Journal of Vascular Research*. 1991;28(Suppl. 1):21-26.
35. Rajan V, Varghese B, van Leeuwen TG, Steenbergen W. Review of methodological developments in laser Doppler flowmetry. *Lasers in medical science*. 2009;24(2):269-283.
36. SCHABAUER AM, ROOKE TW. Cutaneous laser Doppler flowmetry: applications and findings. Paper presented at: Mayo Clinic Proceedings 1994.
37. Haddock R, Hirst G, Hill C. Voltage independence of vasomotion in isolated irideal arterioles of the rat. *The Journal of physiology*. 2002;540(1):219-229.
38. Oishi H, Schuster A, Lambole M, Stergiopoulos N, Meister J-J, Bény J-L. Role of membrane potential in vasomotion of isolated pressurized rat arteries. *Life sciences*. 2002;71(19):2239-2248.
39. Doyle MP, Duling BR. Conducted vasomotion in isolated arterioles: evidence for multiple cellular mechanisms. In: *The Resistance Arteries*. Springer; 1994:171-182.
40. Nilsson H, Aalkjær C. Vasomotion: mechanisms and physiological importance. *Molecular interventions*. 2003;3(2):79.
41. Cole WC, Gordon GR, Braun AP. Cellular and ionic mechanisms of arterial vasomotion. *Smooth Muscle Spontaneous Activity*. 2019:297-312.
42. Berridge M, Rapp PE. A comparative survey of the function, mechanism and control of cellular oscillators. *Journal of Experimental Biology*. 1979;81(1):217-279.
43. Aalkjaer C, Nilsson H. Vasomotion: cellular background for the oscillator and for the synchronization of smooth muscle cells. *British journal of pharmacology*. 2005;144(5):605-616.
44. Haddock RE, Hill CE. Rhythmicity in arterial smooth muscle. *The Journal of physiology*. 2005;566(3):645-656.
45. Peng H, Matchkov V, Ivarsen A, Aalkjær C, Nilsson H. Hypothesis for the initiation of vasomotion. *Circulation research*. 2001;88(8):810-815.
46. Jacobsen JCB, Aalkjaer C, Matchkov VV, Nilsson H, Freiberg JJ, Holstein-Rathlou N-H. Heterogeneity and weak coupling may explain the synchronization characteristics of cells in the arterial wall. *Philosophical Transactions of the Royal Society A: Mathematical, Physical and Engineering Sciences*. 2008;366(1880):3483-3502.
47. Ruehlmann DO, Lee C-H, Poburko D, van Breemen C. Asynchronous Ca<sup>2+</sup> waves in intact venous smooth muscle. *Circulation research*. 2000;86(4):e72-e79.
48. Iino M, Kasai H, Yamazawa T. Visualization of neural control of intracellular Ca<sup>2+</sup> concentration in single vascular smooth muscle cells in situ. *The EMBO Journal*. 1994;13(21):5026-5031.
49. Zang W-J, Balke C, Wier W. Graded  $\alpha$ -adrenoceptor activation of arteries involves recruitment of smooth muscle cells to produce 'all or none' Ca<sup>2+</sup> signals. *Cell Calcium*. 2001;29(5):327-334.
50. Jaggar JH, Nelson MT. Differential regulation of Ca<sup>2+</sup> sparks and Ca<sup>2+</sup> waves by UTP in rat cerebral artery smooth muscle cells. *American Journal of Physiology-Cell Physiology*. 2000;279(5):C1528-C1539.
51. Lee CH, Poburko D, Sahota P, Sandhu J, Ruehlmann DO, van Breemen C. The mechanism of phenylephrine - mediated [Ca<sup>2+</sup>] oscillations underlying tonic contraction in the rabbit inferior vena cava. *The Journal of physiology*. 2001;534(3):641-650.

52. Rahman A, Matchkov V, Nilsson H, Aalkjær C. Effects of cGMP on coordination of vascular smooth muscle cells of rat mesenteric small arteries. *Journal of vascular research*. 2005;42(4):301-311.
53. Gao Y. *Biology of vascular smooth muscle: vasoconstriction and dilatation*. Vol 8: Springer; 2017.
54. Owens GK. Regulation of differentiation of vascular smooth muscle cells. *Physiological reviews*. 1995;75(3):487-517.
55. Fedorovich AA. Functional State of the Microvascular Bed of the Skin in Essential Arterial Hypertension Assessed by Laser Doppler Flowmetry with Amplitude-Frequency Wavelet Analysis of Blood Flow Oscillations. In: *Basic and Clinical Understanding of Microcirculation*. IntechOpen; 2019.
56. Segal SS, Duling BR. Conduction of vasomotor responses in arterioles: a role for cell-to-cell coupling? *American Journal of Physiology-Heart and Circulatory Physiology*. 1989;256(3):H838-H845.
57. Segal SS, Duling BR. Flow control among microvessels coordinated by intercellular conduction. *Science*. 1986;234(4778):868-870.
58. Song H, Tynl K. Evidence for sensing and integration of biological signals by the capillary network. *American Journal of Physiology-Heart and Circulatory Physiology*. 1993;265(4):H1235-H1242.
59. Miriel VA, Mauban JR, Blaustein MP, Gil Wier W. Local and cellular Ca<sup>2+</sup> transients in smooth muscle of pressurized rat resistance arteries during myogenic and agonist stimulation. *The Journal of physiology*. 1999;518(3):815-824.
60. Segal SS, Duling BR. Communication between feed arteries and microvessels in hamster striated muscle: segmental vascular responses are functionally coordinated. *Circulation research*. 1986;59(3):283-290.
61. Welsh DG, Jackson WF, Segal SS. Oxygen induces electromechanical coupling in arteriolar smooth muscle cells: a role for L-type Ca<sup>2+</sup> channels. *American Journal of Physiology-Heart and Circulatory Physiology*. 1998.
62. Wölfle SE, Schmidt VJ, Hoyer J, Köhler R, de Wit C. Prominent role of KCa<sub>3.1</sub> in endothelium-derived hyperpolarizing factor-type dilations and conducted responses in the microcirculation in vivo. *Cardiovascular research*. 2009;82(3):476-483.
63. Welsh DG, Segal SS. Role of EDHF in conduction of vasodilation along hamster cheek pouch arterioles in vivo. *American Journal of Physiology-Heart and Circulatory Physiology*. 2000;278(6):H1832-H1839.
64. Boedtkjer DB, Matchkov V, Boedtkjer E, Nilsson H, Aalkjaer C. Vasomotion has chloride-dependency in rat mesenteric small arteries. *Pflügers Archiv-European Journal of Physiology*. 2008;457(2):389-404.
65. Greenwood IA, Leblanc N. Overlapping pharmacology of Ca<sup>2+</sup>-activated Cl<sup>-</sup> and K<sup>+</sup> channels. *Trends in pharmacological sciences*. 2007;28(1):1-5.
66. VanBavel E, Wesselman JP, Spaan JA. Myogenic activation and calcium sensitivity of cannulated rat mesenteric small arteries. *Circulation research*. 1998;82(2):210-220.
67. Lambole M, Schuster A, Bény J-L, Meister J-J. Recruitment of smooth muscle cells and arterial vasomotion. *American Journal of Physiology-Heart and Circulatory Physiology*. 2003;285(2):H562-H569.

68. Haddock R, Hill C. Differential activation of ion channels by inositol 1, 4, 5 - trisphosphate (IP<sub>3</sub>) - and ryanodine - sensitive calcium stores in rat basilar artery vasomotion. *The Journal of physiology*. 2002;545(2):615-627.
69. Rivers RJ. Remote effects of pressure changes in arterioles. *American Journal of Physiology-Heart and Circulatory Physiology*. 1995;268(3):H1379-H1382.
70. Sheppard LW, Vuksanović V, McClintock P, Stefanovska A. Oscillatory dynamics of vasoconstriction and vasodilation identified by time-localized phase coherence. *Physics in Medicine & Biology*. 2011;56(12):3583.
71. Koenigsberger M, Sauser R, Bény J-L, Meister J-J. Effects of arterial wall stress on vasomotion. *Biophysical journal*. 2006;91(5):1663-1674.
72. Berg BR, Cohen KD, Sarelius IH. Direct coupling between blood flow and metabolism at the capillary level in striated muscle. *American Journal of Physiology-Heart and Circulatory Physiology*. 1997;272(6):H2693-H2700.
73. Davis M, Meininger G, Zawieja D. Stretch-induced increases in intracellular calcium of isolated vascular smooth muscle cells. *American Journal of Physiology-Heart and Circulatory Physiology*. 1992;263(4):H1292-H1299.
74. Demer L, Wortham C, Dirksen E, Sanderson M. Mechanical stimulation induces intercellular calcium signaling in bovine aortic endothelial cells. *American Journal of Physiology-Heart and Circulatory Physiology*. 1993;264(6):H2094-H2102.
75. Li G, Liang J-M, Li P-W, et al. Physiology and cell biology of acupuncture observed in calcium signaling activated by acoustic shear wave. *Pflügers Archiv-European Journal of Physiology*. 2011;462(4):587.
76. Bayliss W. On the local reaction of the arterial wall to changes of internal pressure. *Journal of Physiology, London*. 1974;28:260-276.
77. Davis MJ, Hill MA. Signaling mechanisms underlying the vascular myogenic response. *Physiological reviews*. 1999;79(2):387-423.
78. Fredriksson I, Larsson M, Strömberg T, Iredahl F. Vasomotion analysis of speed resolved perfusion, oxygen saturation, red blood cell tissue fraction, and vessel diameter: Novel microvascular perspectives. *Skin Research and Technology*. 2021.
79. Shimokawa H. *Coronary vasomotion abnormalities*. Springer; 2021.
80. Ghali MG, Styler MJ. Etiologies, cerebral vasomotion, and endothelial dysfunction in the pathophysiology of posterior reversible encephalopathy syndrome in pediatric patients. *Journal of Pediatric Neurology*. 2020;18(02):055-078.
81. Rossi M, Carpi A, Di Maria C, Franzoni F, Galetta F, Santoro G. Skin blood flow motion and microvascular reactivity investigation in hypercholesterolemic patients without clinically manifest arterial diseases. *Physiological research*. 2009;58(1).
82. Ramadan R, Sheps D, Esteves F, et al. Myocardial ischemia during mental stress: role of coronary artery disease burden and vasomotion. *Journal of the American Heart Association*. 2013;2(5):e000321.
83. Schlez A, Kittel M, Braun S, Häfner H-M, Jünger M. Endothelium-dependent regulation of cutaneous microcirculation in patients with systemic scleroderma. *Journal of investigative dermatology*. 2003;120(2):332-334.
84. Schmiedel O, Schroeter ML, Harvey JN. Microalbuminuria in Type 2 diabetes indicates impaired microvascular vasomotion and perfusion. *American Journal of Physiology-Heart and Circulatory Physiology*. 2007;293(6):H3424-H3431.

85. De Ciuceis C. *Microvascular Alterations in Diabetes: Focus on Small Resistance Arteries*. In: *Microcirculation in Cardiovascular Diseases*. Springer; 2020:149-164.
86. Stansberry KB, Shapiro SA, Hill MA, McNitt PM, Meyer MD, Vinik AI. *Impaired peripheral vasomotion in diabetes*. *Diabetes care*. 1996;19(7):715-721.
87. Benbow S, Pryce D, Noblett K, MacFarlane I, Friedmann P, Williams G. *Flow motion in peripheral diabetic neuropathy*. *Clinical Science*. 1995;88(2):191-196.
88. Bouskela E, Cyrino FZ, Wiernsperger N, Bouskela E. *Effects of insulin and the combination of insulin plus metformin (glucophage) on microvascular reactivity in control and diabetic hamsters*. *Angiology*. 1997;48(6):503-514.
89. Renaudin C, Michoud E, Lagarde M, Wiernsperger N. *Impaired microvascular responses to acute hyperglycemia in type I diabetic rats*. *Journal of Diabetes and its Complications*. 1999;13(1):39-44.
90. de Jongh RT, Serné EH, IJzerman RG, Jørstad HT, Stehouwer CD. *Impaired local microvascular vasodilatory effects of insulin and reduced skin microvascular vasomotion in obese women*. *Microvascular research*. 2008;75(2):256-262.
91. Jacobsen JCB, Aalkjær C. *Mechanism and Consequence of Vasomotion*. In: *Physics of Biological Oscillators*. Springer; 2021:261-272.
92. Rucker M, Strobel O, Vollmar B, Roesken F, Menger M. *Vasomotion in critically perfused muscle protects adjacent tissues from capillary perfusion failure*. *American Journal of Physiology-Heart and Circulatory Physiology*. 2000;279(2):H550-H558.
93. Bertuglia S, Colantuoni A, Coppini G, Intaglietta M. *Hypoxia-or hyperoxia-induced changes in arteriolar vasomotion in skeletal muscle microcirculation*. *American Journal of Physiology-Heart and Circulatory Physiology*. 1991;260(2):H362-H372.
94. Anderson GK, Rosenberg AJ, Barnes HJ, et al. *Peaks and valleys: oscillatory cerebral blood flow at high altitude protects cerebral tissue oxygenation*. *Physiological measurement*. 2021;42(6):064005.
95. Shaffer F, McCraty R, Zerr CL. *A healthy heart is not a metronome: an integrative review of the heart's anatomy and heart rate variability*. *Frontiers in psychology*. 2014;5:1040.
96. Kim H-G, Cheon E-J, Bai D-S, Lee YH, Koo B-H. *Stress and heart rate variability: a meta-analysis and review of the literature*. *Psychiatry investigation*. 2018;15(3):235.
97. Shaffer F, Ginsberg J. *An overview of heart rate variability metrics and norms*. *Frontiers in public health*. 2017;5:258.
98. Forte G, Favieri F, Casagrande M. *Heart rate variability and cognitive function: a systematic review*. *Frontiers in neuroscience*. 2019;13:710.
99. Vaillancourt DE, Newell KM. *Changing complexity in human behavior and physiology through aging and disease*. *Neurobiology of aging*. 2002;23(1):1-11.
100. Lehrer P, Vaschillo E. *The Future of Heart Rate Variability Biofeedback*. *Biofeedback*. 2008;36(1).
101. Karemaker JM. *Counterpoint: respiratory sinus arrhythmia is due to the baroreflex mechanism*. *Journal of applied physiology*. 2009;106(5):1742-1743.
102. Man T, Riese H, Jaju D, et al. *Heritability and genetic and environmental correlations of heart rate variability and baroreceptor reflex sensitivity with ambulatory and beat-to-beat blood pressure*. *Scientific reports*. 2019;9(1):1-8.
103. Acharya UR, Joseph KP, Kannathal N, Lim CM, Suri JS. *Heart rate variability: a review*. *Medical and biological engineering and computing*. 2006;44(12):1031-1051.

104. *Goldberger AL. Is the normal heartbeat chaotic or homeostatic? Physiology. 1991;6(2):87-91.*
105. *Beckers F, Verheyden B, Aubert AE. Aging and nonlinear heart rate control in a healthy population. American Journal of Physiology-Heart and Circulatory Physiology. 2006;290(6):H2560-H2570.*
106. *Goldbeter A. Biochemical oscillations and cellular rhythms: the molecular bases of periodic and chaotic behaviour. Cambridge university press; 1997.*
107. *Meyer T, Stryer L. Molecular model for receptor-stimulated calcium spiking. Proceedings of the National Academy of Sciences. 1988;85(14):5051-5055.*
108. *Schuster S, Marhl M, Höfer T. Modelling of simple and complex calcium oscillations. The FEBS Journal. 2002;269(5):1333-1355.*
109. *Parthimos D, Edwards DH, Griffith T. Minimal model of arterial chaos generated by coupled intracellular and membrane Ca<sup>2+</sup> oscillators. American Journal of Physiology-Heart and Circulatory Physiology. 1999;277(3):H1119-H1144.*
110. *Griffith T, Edwards D. Fractal analysis of role of smooth muscle Ca<sup>2+</sup> fluxes in genesis of chaotic arterial pressure oscillations. American Journal of Physiology-Heart and Circulatory Physiology. 1994.*
111. *Parthimos D, Haddock R, Hill C, Griffith TM. Dynamics of a three-variable nonlinear model of vasomotion: comparison of theory and experiment. Biophysical journal. 2007;93(5):1534-1556.*
112. *Ursino M, Colantuoni A, Bertuglia S. Vasomotion and blood flow regulation in hamster skeletal muscle microcirculation: a theoretical and experimental study. Microvascular research. 1998;56(3):233-252.*
113. *Arciero J, Secomb T. Spontaneous oscillations in a model for active control of microvessel diameters. Mathematical medicine and biology: a journal of the IMA. 2010;29(2):163-180.*
114. *Wellens T, Shatokhin V, Buchleitner A. Stochastic resonance. Reports on progress in physics. 2003;67(1):45.*
115. *Harmer GP, Davis BR, Abbott D. A review of stochastic resonance: Circuits and measurement. IEEE Transactions on Instrumentation and Measurement. 2002;51(2):299-309.*
116. *Gammaitoni L, Hänggi P, Jung P, Marchesoni F. Stochastic resonance. Reviews of modern physics. 1998;70(1):223.*
117. *Hänggi P. Stochastic resonance in biology how noise can enhance detection of weak signals and help improve biological information processing. ChemPhysChem. 2002;3(3):285-290.*
118. *Longtin A, Bulsara A, Moss F. Time-interval sequences in bistable systems and the noise-induced transmission of information by sensory neurons. Physical review letters. 1991;67(5):656.*
119. *Bulsara A, Jacobs E, Zhou T, Moss F, Kiss L. Stochastic resonance in a single neuron model: Theory and analog simulation. Journal of Theoretical Biology. 1991;152(4):531-555.*
120. *Bulsara A, Moss F. Single neuron dynamics: Noise-enhanced signal processing. Paper presented at: [Proceedings] 1991 IEEE International Joint Conference on Neural Networks 1991.*

121. Douglass JK, Wilkens L, Pantazelou E, Moss F. Noise enhancement of information transfer in crayfish mechanoreceptors by stochastic resonance. *Nature*. 1993;365(6444):337-340.
122. Collins JJ, Imhoff TT, Grigg P. Noise-enhanced information transmission in rat SAI cutaneous mechanoreceptors via aperiodic stochastic resonance. *Journal of Neurophysiology*. 1996;76(1):642-645.
123. Gluckman BJ, Netoff TI, Neel EJ, Ditto WL, Spano ML, Schiff SJ. Stochastic resonance in a neuronal network from mammalian brain. *Physical Review Letters*. 1996;77(19):4098.
124. Di Rienzo M, Parati G, Radaelli A, Castiglioni P. Baroreflex contribution to blood pressure and heart rate oscillations: time scales, time-variant characteristics and nonlinearities. *Philosophical Transactions of the Royal Society A: Mathematical, Physical and Engineering Sciences*. 2009;367(1892):1301-1318.
125. Mandell AJ, Selz KA. Brain stem neuronal noise and neocortical "resonance". *Journal of Statistical Physics*. 1993;70(1):355-373.
126. Hidaka I, Nozaki D, Yamamoto Y. Functional stochastic resonance in the human brain: noise induced sensitization of baroreflex system. *Physical review letters*. 2000;85(17):3740.
127. Yamamoto Y, Soma R, Kitajo K, et al. Functional Roles of Noise and Fluctuations in the Human Brain. Paper presented at: AIP Conference Proceedings 2005.
128. Yamamoto Y, Hughson RL. On the fractal nature of heart rate variability in humans: effects of data length and beta-adrenergic blockade. *American Journal of Physiology-Regulatory, Integrative and Comparative Physiology*. 1994;266(1):R40-R49.
129. Kubota T, Chishaki H, Yoshida T, Sunagawa K, Takeshita A, Nose Y. How to encode arterial pressure into carotid sinus nerve to invoke natural baroreflex. *American Journal of Physiology-Heart and Circulatory Physiology*. 1992;263(1):H307-H313.
130. Triedman JK, Saul JP. Blood pressure modulation by central venous pressure and respiration. Buffering effects of the heart rate reflexes. *Circulation*. 1994;89(1):169-179.
131. Suki B, Alencar A, Sujeer M, et al. Life-support system benefits from noise. *Nature*. 1998;393(6681):127-128.
132. Camalet S, Duke T, Jülicher F, Prost J. Auditory sensitivity provided by self-tuned critical oscillations of hair cells. *Proceedings of the National Academy of Sciences*. 2000;97(7):3183-3188.
133. Adair RK, Astumian RD, Weaver JC. Detection of weak electric fields by sharks, rays, and skates. *Chaos: An Interdisciplinary Journal of Nonlinear Science*. 1998;8(3):576-587.
134. Harry JD, Niemi JB, Priplata AA, Collins J. Balancing act [noise based sensory enhancement technology]. *IEEE Spectrum*. 2005;42(4):36-41.
135. Hijmans JM, Geertzen JH, Schokker B, Postema K. Development of vibrating insoles. *International Journal of Rehabilitation Research*. 2007;30(4):343-345.
136. Morse RP, Evans EF. Enhancement of vowel coding for cochlear implants by addition of noise. *Nature medicine*. 1996;2(8):928-932.
137. Morse RP, Morse PF, Nunn TB, Archer KA, Boyle P. The effect of Gaussian noise on the threshold, dynamic range, and loudness of analogue cochlear implant stimuli. *Journal of the Association for Research in Otolaryngology*. 2007;8(1):42-53.
138. Stocks N, Allingham D, Morse R. The application of suprathreshold stochastic resonance to cochlear implant coding. *Fluctuation and noise letters*. 2002;2(03):L169-L181.

139. Lefevre GR, Kowalski SE, Girling L, Thiessen DB, Mutch W. Improved arterial oxygenation after oleic acid lung injury in the pig using a computer-controlled mechanical ventilator. *American journal of respiratory and critical care medicine*. 1996;154(5):1567-1572.
140. Li C, Chang Q, Zhang J, Chai W. Effects of slow breathing rate on heart rate variability and arterial baroreflex sensitivity in essential hypertension. *Medicine*. 2018;97(18).
141. McDonnell MD, Abbott D. What is stochastic resonance? Definitions, misconceptions, debates, and its relevance to biology. *PLoS Comput Biol*. 2009;5(5):e1000348.
142. Ziegler MG. Heart Rate Variability. *Psychosomatic medicine*. 2021;83(7):813-814.
143. Hauton D, Ray CJ. Caffeine, gravity, and baroreceptor function: the integration of diet and cardiovascular control. *Advances in Physiology Education*. 2018;42(3):454-461.
144. Lai Y-H, Yuan Y, Liang Y-X, Yu J-H. Comparison of aging effect between cardiac complexity and baroreceptor sensitivity. Paper presented at: 2021 International Conference on Information Technology and Biomedical Engineering (ICITBE)2021.
145. Torrence C, Compo GP. A Practical Guide to Wavelet Analysis. *Bulletin of the American Meteorological Society*. 1998;79(1):61-78.
146. Huang NE, Long SR, Shen Z. The mechanism for frequency downshift in nonlinear wave evolution. *Advances in applied mechanics*. 1996;32:59-117C.
147. Huang NE, Shen Z, Long SR, et al. The empirical mode decomposition and the Hilbert spectrum for nonlinear and non-stationary time series analysis. *Proceedings of the Royal Society of London Series A: mathematical, physical and engineering sciences*. 1998;454(1971):903-995.
148. Huang NE, Shen Z, Long SR. A new view of nonlinear water waves: the Hilbert spectrum. *Annual review of fluid mechanics*. 1999;31(1):417-457.
149. Huang NE. Introduction to the Hilbert–Huang transform and its related mathematical problems. In: *Hilbert–Huang transform and its applications*. World Scientific; 2014:1-26.
150. Huang NE, Wu Z. A review on Hilbert - Huang transform: Method and its applications to geophysical studies. *Reviews of geophysics*. 2008;46(2).
151. Huang NE, Attoh-Okine NO. *The Hilbert-Huang transform in engineering*. CRC Press; 2005.
152. Huang NE. *Hilbert-Huang transform and its applications*. Vol 16: World Scientific; 2014.
153. Huang Y, Erdogmus D, Hild K, Pavel M, Mathan S. Mixed effects models for single-trial ERP detection in noninvasive brain computer interface design. *Recent Advances in Biomedical Signal Processing*. 2009:171-180.
154. Huang Y, Erdogmus D, Pavel M, Mathan S. Mixed effects models for EEG evoked response detection. Paper presented at: 2008 IEEE Workshop on Machine Learning for Signal Processing2008.
155. Lin C-F, Zhu J-D. Hilbert–Huang transformation-based time-frequency analysis methods in biomedical signal applications. *Proceedings of the Institution of Mechanical Engineers, Part H: Journal of Engineering in Medicine*. 2012;226(3):208-216.
156. Fu K, Qu J, Chai Y, Dong Y. Classification of seizure based on the time-frequency image of EEG signals using HHT and SVM. *Biomedical Signal Processing and Control*. 2014;13:15-22.

157. Stork M, Mayer D, Hrusak J. High resolution analog-digital converter and digital polynomial filter applications. *WSEAS Transactions on signal processing*. 2006(3):351-356.
158. Stork M, Trefny Z. New seismocardiographic measuring system with separate QRS detection. *Latest Trends on Systems*. 2010;1:176-180.
159. Das A, Stocks N, Nikitin A, Hines E. Quantifying stochastic resonance in a single threshold detector for random aperiodic signals. *Fluctuation and Noise Letters*. 2004;4(02):L247-L265.
160. Mills C, Gabe I, Gault J, et al. Pressure-flow relationships and vascular impedance in man. *Cardiovascular Research*. 1970;4(4):405-405.
161. Truskey GA, Yuan F, Katz DF. *Transport phenomena in biological systems*. 2004.
162. Kanaris A, Anastasiou A, Paras S. Modeling the effect of blood viscosity on hemodynamic factors in a small bifurcated artery. *Chemical Engineering Science*. 2012;71:202-211.
163. Blair GS. An equation for the flow of blood, plasma and serum through glass capillaries. *Nature*. 1959;183(4661):613-614.
164. Copley AL, Stainsby G. *Flow properties of blood and other biological systems*. Flow properties of blood and other biological systems. 1960.
165. Merrill E, Benis A, Gilliland E, Sherwood T, Salzman E. Pressure-flow relations of human blood in hollow fibers at low flow rates. *Journal of Applied Physiology*. 1965;20(5):954-967.
166. Pries AR, Secomb T, Gaehtgens P, Gross J. Blood flow in microvascular networks. Experiments and simulation. *Circulation research*. 1990;67(4):826-834.
167. Xu D, Warnecke S, Song B, Ma X, Hof B. Transition to turbulence in pulsating pipe flow. *Journal of Fluid Mechanics*. 2017;831.
168. Avila K, Moxey D, Lozar AD, Avila M, Barkley D, Hof B. The Onset of Turbulence in Pipe Flow. *Science*. 2011;333(6039):192-196.
169. Avila M, Willis AP, Hof BR. On the transient nature of localized pipe flow turbulence. *Journal of Fluid Mechanics*. 2010;646:127.
170. Hof B, Mukund V, Lemoult G, Avila M, Song B, Barkley D. The rise of fully turbulent flow. *Nature*. 2015;526(7574):550-553.
171. Eckhardt B, Schneider TM, Hof B, Westerweel J. Turbulence Transition in Pipe Flow. *Annual Review of Fluid Mechanics*. 2007;39(1):447-468.
172. de Boer MP, Wijnstok NJ, Serné EH, et al. Body mass index is related to microvascular vasomotion, this is partly explained by adiponectin. *European journal of clinical investigation*. 2014;44(7):660-667.
173. Porret C, Stergiopoulos N, Hayoz D, Brunner H, Meister J. Simultaneous ipsilateral and contralateral measurements of vasomotion in conduit arteries of human upper limbs. *American Journal of Physiology-Heart and Circulatory Physiology*. 1995;269(6):H1852-H1858.
174. Mayhew JE, Askew S, Zheng Y, et al. Cerebral vasomotion: a 0.1-Hz oscillation in reflected light imaging of neural activity. *Neuroimage*. 1996;4(3):183-193.
175. Newman JM, Dwyer RM, St - Pierre P, Richards SM, Clark MG, Rattigan S. Decreased microvascular vasomotion and myogenic response in rat skeletal muscle in association with acute insulin resistance. *The Journal of physiology*. 2009;587(11):2579-2588.

176. Wang Y-YL, Jan M-Y, Shyu C-S, Chiang C-A, Wang W-K. *The natural frequencies of the arterial system and their relation to the heart rate. IEEE Transactions on Biomedical Engineering.* 2004;51(1):193-195.
177. Bedford DE. *The ancient art of feeling the pulse. British heart journal.* 1951;13(4):423.